Originally published as:

RESEARCH ARTICLE

Key Points:
- [10]Be-derived erosion rates from the Himalaya and Eastern Tibet indicate regional differences in erosional efficiency
- Monsoonal discharge variability can be parameterized by a weighted sum of two inverse gamma distributions
- Stochastic-threshold stream power model helps reconcile observed scatter in erosion rate data

Supporting Information:
- Supporting Information S1
- Table S1
- Table S2
- Table S3
- Table S4

Correspondence to:
D. Scherler,
scherler@gfz-potsdam.de

Testing monsoonal controls on bedrock river incision in the Himalaya and Eastern Tibet with a stochastic-threshold stream power model

Dirk Scherler[1,2] (iD), Roman A. DiBiase[3] (iD), G. Burch Fisher[4], and Jean-Philippe Avouac[5] (iD)

[1]German Research Centre for Geosciences GFZ, Potsdam, Germany, [2]Institute for Geological Sciences, Freie Universität Berlin, Berlin, Germany, [3]Department of Geosciences, Pennsylvania State University, University Park, Pennsylvania, USA, [4]Jackson School of Geosciences, University of Texas at Austin, Austin, Texas, USA, [5]Division of Geological and Planetary Sciences, California Institute of Technology, Pasadena, California, USA

Abstract [10]Be-derived catchment average erosion rates from the Himalaya and Eastern Tibet show different relationships with normalized channel steepness index (k_{sn}), suggesting differences in erosional efficiency of bedrock river incision. We used a threshold stream power model (SPM) combined with a stochastic distribution of discharges to explore the extent to which this observation can be explained by differences in the mean and variability of discharge between the two regions. Based on the analysis of 199 daily discharge records (record lengths 3–45 years; average 18.5 years), we parameterized monsoonal discharge with a weighted sum of two inverse gamma distributions. During both high- and low-flow conditions, annual and interannual discharge variabilities are similarly low in each region. Channel widths for 36 rivers indicate, on average, 25% wider streams in Eastern Tibet than in the Himalaya. Because most catchments with [10]Be data are not gauged, we constrained mean annual discharge in these catchments using gridded precipitation data sets that we calibrated to the available discharge records. Comparing [10]Be-derived with modeled erosion rates, the stochastic-threshold SPM explains regional differences better than a simple SPM based on drainage area or mean annual runoff. Systematic differences at small k_{sn} values can be reconciled with k_{sn}-dependent erosion thresholds, whereas substantial scatter for high k_{sn} values persists, likely due to methodological limitations. Sensitivity analysis of the stochastic-threshold SPM calibrated to the Himalaya indicates that changes in the duration or strength of summer monsoon precipitation have the largest effect on erosional efficiency, while changes in monsoonal discharge variability have almost no effect. The modeling approach presented in this study can in principle be used to assess the impact of precipitation changes on erosion.

Plain Language Summary River incision is the main process that erodes mountain belts such as the Himalaya or Tibet. Existing models of river incision emphasize the role of water discharge and river slopes. More recent research, however, emphasizes the role of discharge variability, i.e., how variable the streamflow of an individual river is over time. Theoretically, it is possible that rivers with less but more variable discharge are more erosive than rivers with more but less variable discharge. Despite growing understanding of the mechanics of river incision it has been difficult to test existing models of river incision with field data. In our study, we combine a state-of-the-art model of river incision with a wealth of empirical data from the Himalaya and Eastern Tibet to test the importance of discharge variability and to assess whether observed differences in centennial to millennial erosion rates can be reconciled with our current understanding of the climatic and topographic controls on river incision. Results show that the importance of discharge variability in the Himalaya is much smaller than expected and plays a role only in gently-sloping rivers. While observations can be reconciled with our model to some degree, remaining discrepancies highlight shortcomings of the model as well as the data used to constrain the model.

1. Introduction

River incision into bedrock is in most mountains on Earth the main process controlling landscape-scale erosion, because rivers set the base level for adjacent hill slopes and communicate changes in climate and tectonics through the landscape. Understanding the mechanisms of bedrock river incision is thus critical for landscape evolution models that can be used to assess how landscapes adjust to changing tectonic and climatic forcing. Additionally, models of bedrock river incision are important for assessing the spatial variation

of erosion rates in a landscape and for inferring spatiotemporal patterns of rock uplift rate [e.g., *Hurtrez et al.*, 1999; *Lavé and Avouac*, 2001; *Kirby and Whipple*, 2001; *Lague and Davy*, 2003; *Kirby and Whipple*, 2012]. Fluvial transport of sediment and incision into bedrock is widely assumed to depend to first order on the shear stress that is exerted by flowing water at the river bed [e.g., *Bagnold*, 1977; *Howard and Kerby*, 1983; *Whipple*, 2004]. Because bed shear stresses depend on the slope of the water surface and the flow velocity, and thus the depth of water, river incision depends on climate and topography. By using upstream drainage area as a proxy for water discharge, the expression for bedrock river incision takes the form of the simple but popular stream power model [e.g., *Whipple and Tucker*, 1999; *Lague*, 2014]:

$$\bar{I} = KA^m S^n, \tag{1}$$

which relates the rate of long-term bedrock river incision $\bar{I}$, to drainage area A and channel slope S to powers of m and n, respectively. In this formulation, rock erodibility and climatic effects are folded into an erosional efficiency parameter, K, whereas sediment-flux-dependent tools and cover effects [e.g., *Sklar and Dietrich*, 2004] are not explicitly accounted for. In topographic steady state, the stream power model predicts a power law relationship between channel slopes and drainage area within catchments with uniform rock uplift rate and erosional efficiency. This predicted scaling mimics observed scaling in fluvial landscapes [*Flint*, 1974] known as Flint's law:

$$S = k_s A^{-\theta}, \tag{2}$$

where k_s is the channel steepness index and θ is the concavity index [*Whipple and Tucker*, 1999]. Based on the stream power law and provided topographic steady state, the channel steepness index is predicted to increase monotonically with long-term incision rate and the concavity index is predicted to be equal to m/n [e.g., *Whipple et al.*, 2013]. Despite its simplicity and known shortcomings [e.g., *Lague*, 2014], the stream power model has been widely adopted due to the ease of measuring channel slopes and drainage areas from digital elevation models [*Wobus et al.*, 2006]. It further provides a convenient framework to relate catchment-scale erosion rates to topographic relief, which scales with the channel steepness index [*DiBiase et al.*, 2010]. The utility of this approach has been confirmed with empirical data that show robust trends between channel steepness index and detrital [10]Be-derived erosion rates across different landscapes [e.g., *Ouimet et al.*, 2009; *DiBiase et al.*, 2010; *Cyr et al.*, 2010; *Scherler et al.*, 2014a; *Mandal et al.*, 2015]:

$$E_{10Be} \propto k_s{}^\phi, \tag{3}$$

where E_{10Be} is [10]Be-derived erosion rate and ϕ is an empirical exponent. The scaling parameters of this relationship vary widely between landscapes, as a result of differences in climate and/or rock erodibility [*Kirby and Whipple*, 2012; *Lague*, 2014]. This is expected, as it has long been recognized that the efficiency of geomorphologic processes, river incision in particular, depends on the hydrology and climatic regime [e.g., *Wolman and Miller*, 1960; *Molnar et al.*, 2006]. As argued by *Tucker* [2004], *Lague et al.* [2005], and *DiBiase and Whipple* [2011], variations in both the magnitude of erosion rate and the nonlinearity of the relationship between E and k_s (as expressed by ϕ) can result from the size and frequency of floods that are large enough to overcome detachment and transport thresholds [e.g., *Tucker and Bras*, 2000; *Snyder et al.*, 2003] and incise bedrock. Such threshold effects cannot be accounted for by equation (1), which assumes a constant effective discharge that scales with drainage area A.

The degree to which spatial or temporal variations in discharge variability can affect the relationship of equation (3) depends largely on the size of incision thresholds and the tail of the discharge distribution i.e., the magnitude and frequency of large floods [e.g., *Tucker and Bras*, 2000; *Molnar et al.*, 2006]. *DiBiase and Whipple* [2011] examined this problem in the San Gabriel Mountains of southern California and suggested that the direction and degree to which incision rates respond to climatic changes additionally depend on the channel steepness. Using a model with a stochastic distribution of floods, they showed that in their study area, incision rates are, for a wide range of steepness values, relatively insensitive to changes in mean annual precipitation above ~500 mm yr^{-1}. However, these predictions strongly depend on the relationship between the mean and variability of discharge (or precipitation), which is not well constrained.

In this study, we follow a similar approach to explore the degree to which accounting for incision thresholds and a stochastic distribution of floods explains the connection between climate, topography, and erosion rate in the Himalaya and the Eastern Tibetan Plateau. We have two main objectives. First, we aim to characterize the spatial and temporal variations in stream discharge throughout the mountainous regions of South and East Asia. While modern rainfall patterns are well constrained from satellite-derived

observations (e.g., Tropical Rainfall Measuring Mission data, 1998–2015), quantifying the frequency and magnitude of floods has been difficult due to sparse gauging records. Thus, we use satellite observations to upscale existing gauging records across the whole mountain range. Second, the past decade has seen an explosion in detrital cosmogenic [10]Be-derived erosion rate measurements in the Himalaya and the Eastern Tibetan Plateau [*Wobus et al.*, 2005; *Harkins et al.*, 2007; *Finnegan et al.*, 2008; *Ouimet et al.*, 2009; *Godard et al.*, 2010, 2012, 2014; *Scherler et al.*, 2014a]. While individually, these data sets define relatively robust relationships between topographic metrics and erosion rate, overall there is an ~3–5 times difference in erosional efficiency between the two regions. Thus, we use our analysis of discharge records in the first part of the paper to test whether the difference in erosional efficiency can be explained by regional differences in monsoonal patterns of precipitation and discharge.

In the following, we will first provide the theoretical framework of our study and a brief overview of the stochastic-threshold stream power model (section 2). We then review published [10]Be-derived erosion rates from the Himalaya and Eastern Tibet that expose regional differences in erosional efficiency (section 3). In section 4, we present an analysis of existing discharge records and gridded precipitation data from both field areas to constrain runoff mean and variability parameters. In section 5, we present the application of the stochastic-threshold stream power model to the Himalaya and Eastern Tibet, followed by an evaluation and discussion of model results for both landscapes. Last, we discuss the implications of this model for temporal variations in monsoon strength and landscape evolution (section 6).

2. Theoretical Framework

2.1. The Stochastic-Threshold Stream Power Model

In the shear stress, or similarly, stream power model (SPM) of detachment-limited channel incision, the local and instantaneous incision rate, I, is cast as a power function of the mean bed shear stress, τ_b [e.g., *Howard and Kerby*, 1983; *Whipple and Tucker*, 1999]. Here we follow the form proposed by *Tucker* [2004]:

$$I = k_e\left(\tau_b^a - \tau_c^a\right), \tag{4}$$

where τ_c is a threshold shear stress that has to be overcome before incision occurs, a is an exponent that can be related to the incision process [*Whipple et al.*, 2000a], and k_e is an erodibility parameter that quantifies the erodibility of the substrate. The erodibility parameter is typically the least constrained parameter in applications of the SPM to natural landscapes, whereas both τ_b and τ_c are commonly related to hydraulic geometry relationships that largely stem from alluvial rivers [e.g., *Howard et al.*, 1994; *Tucker and Bras*, 2000]. Here we follow previous approaches and assume steady, uniform flow in wide, open channels, so that bed shear stress can be expressed by:

$$\tau_b = k_t\left(\frac{Q}{W}\right)^\alpha S^\beta, \tag{5}$$

where k_t is a constant that relates to the flow resistance, Q is water discharge, W is channel width, S is the downstream gradient of the water surface (approximated by the channel bed slope), and α and β are exponents that depend on the flow resistance relationship ($\alpha = 3/5$, $\beta = 7/10$ in the Gauckler-Manning-Strickler relationship, and $\alpha = \beta = 2/3$ in the Darcy-Weissbach relationship) [*Howard*, 1994].In steady state landscapes of uniform lithology and rock uplift rates, the bankfull channel width of bedrock rivers W_b is typically described by a power law relationship with mean-annual discharge $\overline{Q}$ [*Montgomery and Gran*, 2001; *Wohl and David*, 2008] according to:

$$W_b = k_w \overline{Q}^{\omega_b}, \tag{6}$$

where k_w and ω_b are empirical scaling parameters. In addition to downstream changes in channel geometry, it is also necessary to parameterize how stochastic discharge events map into stochastic bed shear stresses. This is typically done using a geometrical treatment of at-a-station changes in channel width W as a function of discharge:

$$\frac{W}{W_b} = \left(\frac{Q}{\overline{Q}}\right)^{\omega_s}, \tag{7}$$

where ω_s is an empirical scaling parameter [*Tucker*, 2004; *Turowski et al.*, 2008]. Cross-sectional flow models indicate that ω_s stays near a value of 0.25 over a wide range of channel geometries due to a competition

between increasing channel width for gentle banks and increasing sidewall friction for steep banks [*DiBiase and Whipple*, 2011]. In many landscapes, the mean annual discharge can be related to the mean annual catchment-integrated runoff $\overline{R}$ and drainage area A according to

$$\overline{Q} = \overline{R}A^c \tag{8}$$

where c is an exponent that is often close to unity in upland landscapes [*Tucker and Bras*, 2000]. Assuming $c = 1$ and combining equations (5) to (8) with the incision model of equation (4), and a channel-steepness representation of channel slope from equation (3), the following stochastic-threshold SPM can be derived [*DiBiase and Whipple*, 2011]:

$$I = K\,Q^{*\gamma}\,k_s^n - \psi, \quad K = k_e k_t^a k_w^{-\alpha a}\overline{R}^m, \quad \psi = k_e \tau_c^a \tag{9}$$

with the exponents $m = a\alpha(1 - \omega_b)$, $n = a\beta$, $\gamma = a\alpha(1 - \omega_s)$, and the normalized discharge $Q^* = Q/\overline{Q}$. Note that m and n are the same exponents as in equation (1). For comparison with field data, we used the normalized steepness index, $k_{sn} = SA^{\theta\mathrm{ref}}$, where the reference concavity index, θ_{ref}, is fixed to be $m/n = 0.45$ [*Wobus et al.*, 2006]. In this formulation of bedrock river incision, the influence of climate can occur in two ways: through the mean annual runoff, $\overline{R}$, and through the discharge variability, expressed through variation in Q^*. The strength with which these two climate properties affect the incision process largely depends on the two exponents m and γ. Thus, even if the stream power exponent, n, is equal to one, a nonlinear relationship between I and k_{sn} can emerge due to the combination of variable discharge and the presence of an erosion threshold [*Tucker*, 2004; *Lague et al.*, 2005; *DiBiase and Whipple*, 2011]. If incision thresholds are assumed to be negligible ($\psi = 0$) then a single, effective discharge (e.g., bankfull flood [*Wolman and Miller*, 1960]) can be incorporated into the erosional efficiency parameter, K, and equation (9) simplifies to $I = Kk_s^n$, which is an alternative formulation of equation (1). In topographic steady state, the long-term erosion rate of a catchment, E, is equal to the long-term incision rate, $\bar{I}$, which we obtain by combining the stochastic-threshold SPM of equation (9) with a probability density function (pdf) that describes the frequency of any given discharge magnitude, and integrating over the range of all possible discharges [*Tucker and Bras*, 2000; *Tucker*, 2004; *Lague et al.*, 2005; *DiBiase and Whipple*, 2011]:

$$E = \bar{I} = \int_{Q_c^*}^{Q_m^*} I(Q^*, k_s)pdf(Q^*)dQ^*, \tag{10}$$

where Q_m^* represents the maximum possible normalized discharge and Q_c^* stands for the normalized critical discharge that is required to overcome the threshold shear stress. The exact value of Q_m^* is difficult to define, as the recurrence time for the largest flood events may be longer than the longest observational records. For instance, in partly glaciated catchments, extremely large but rare floods can occur due to the outburst of glacial lakes [e.g., *Montgomery et al.*, 2004; *Scherler et al.*, 2014b]. However, for a wide range of parameter values the integral in equation (10) converges rapidly and is insensitive to the choice of Q_m^* [*Lague et al.*, 2005]. The normalized critical discharge, Q_c^*, can be obtained by setting $I = 0$ in equation (9)

$$Q_c^* = \left(\frac{\psi}{Kk_s^n}\right)^{\frac{1}{\gamma}} = \left(\frac{\tau_c k_w^\alpha}{k_t \overline{R}^{\alpha(1-\omega_b)} k_s^\beta}\right)^{\frac{a}{\gamma}}. \tag{11}$$

From equation (11) it can be seen that Q_c^* depends not only on the threshold shear stress but also on parameters that describe water flow across the bed, specifically channel steepness (k_s), the width index (k_w), and the mean annual runoff ($\overline{R}$). Hence, the influence of the threshold term in controlling long-term incision rates depends in different ways on how climate expresses itself in mean discharge and discharge variability and on how this changes across different parts of a landscape [*DiBiase and Whipple*, 2011]. Thus, one emphasis of this paper will be determining how the mean and variability of discharge varies across our study area.

2.2. Modeling Approach

The stochastic-threshold SPM provides a theoretical foundation to account for the effects of climate on mean discharge and discharge variability in the context of bedrock river incision. The specific form of the stochastic-threshold SPM shown in equations (9) and (10) is particularly suitable for comparison with landscape-scale data such as ^{10}Be concentrations in stream sediments, which reflect catchment-average hillslope erosion rates, as all of the input parameters are independent of drainage area and representable by scalar values [*DiBiase and Whipple*, 2011]. Importantly, the slope and width of a river channel are defined by k_s and k_w,

respectively. The necessary assumptions that allow us to use these equations and compare modeled incision rates with ^{10}Be-derived erosion rates are: (i) that the studied catchments are in topographic steady state so that hillslopes and rivers erode uniformly at the same rate; (ii) that precipitation and rock uplift rates are approximately uniform within a catchment; and (iii) that the topographic and hydrologic parameters that enter equations (9) and (10) are representative for the time scales implied by ^{10}Be-derived erosion rates (typically 10^2–10^3 year time scales for the data in this study). Positive correlations between ^{10}Be-derived erosion rates and k_{sn} [e.g., *Ouimet et al.*, 2009; *DiBiase et al.*, 2010; *Scherler et al.*, 2014a] support the notion of topographic steady state, and as long as catchments are sufficiently small ($< \sim$1000 km^2), assumptions (i) and (ii) appear reasonable. While the third assumption (iii) is unproblematic with respect to topographic parameters, due to slow changes in topography, it is more difficult to evaluate with respect to the hydrologic conditions, because climatic changes can be fast and quantitative paleo-hydrological data are rare. We will revisit this issue in the discussion of our results.

3. Characteristics of Study Area and Erosion Rates From Prior Work

Our study focuses on the monsoonal regions of mountainous Asia that border the Tibetan Plateau to the south and east (Figure 1a). These areas are regions of active tectonics and comprise a wide range of topographic relief and rock uplift rates. According to the different tectonic and climatic settings, we distinguish two different geographic regions in this study: the Himalaya and Eastern Tibet.

3.1. Study Regions
3.1.1. Himalaya
The Himalaya forms the southern margin of the Tibetan Plateau and is the result of the ongoing collision between India and Eurasia and associated crustal shortening [e.g., *Molnar and Tapponnier*, 1975; *Avouac*, 2003]. Surface elevations rise from a few hundred meters in the Indo-Gangetic Plains to more than 5 km on the plateau, over a distance of typically less than 200 km. Active shortening is considered to be accommodated mostly by slip on the Main Himalayan Thrust fault, which separates the Indian plate from the orogenic wedge, and to a lesser degree by internal shortening within the wedge [*Avouac*, 2003]. Exhumation of the orogenic wedge has been ongoing since at least the Neogene, potentially linked to the intensity of the Asian monsoon [*Clift et al.*, 2008a]. Exhumation rates deduced from low-temperature thermochronology range between ~0.5 and 5 mm yr^{-1} [*Thiede and Ehlers*, 2013].

The Himalaya receives among the worldwide highest amounts of rainfall (up to >4000 mm yr^{-1} [*Miehe et al.*, 2001]) that are focused within one or two relatively narrow bands parallel to the range (Figure 1b), where surface elevations rise steeply [e.g., *Bookhagen and Burbank*, 2006]. Very high precipitation during the summer monsoon season contrasts with very low precipitation during winter, especially in the Central Himalaya. Farther to the west, westerly-derived precipitation increases and causes another peak in precipitation between late winter and early spring [e.g., *Miehe et al.*, 2001], primarily as snowfall at high elevations [*Winiger et al.*, 2005; *Wulf et al.*, 2010]. Despite considerable ice and seasonal snow coverage in the high elevations of the Himalaya, modeling studies suggest that in the Ganges drainage system, the melt-water contribution to runoff is minor compared to that from rainfall [*Immerzeel et al.*, 2010; *Bookhagen and Burbank*, 2010].

The bedrock in the Himalaya can be broadly classified into four different tectonostratigraphic units that are found along the entire Himalayan arc [e.g., *Gansser*, 1964; *Hodges*, 2000; *Yin*, 2006]. The southernmost unit is the Subhimalaya, which mostly consists of weakly consolidated Neogene-Quaternary sediments that were eroded from the growing orogen and deposited in the foreland. Subhimalayan rocks are exposed in the Siwaliks, a chain of low-relief hills (<1000 m relief) that have formed above actively rising anticlines [e.g., *Lavé and Avouac*, 2001]. Structurally higher and to the north of the Subhimalaya follows the Lesser Himalayan Sequence (LHS), which consists mainly of low-grade metasedimentary Proterozoic rocks of the Indian passive margin. The structurally next higher unit is the High or Greater Himalayan Sequence (HHS), which comprises mostly high-grade metamorphic gneisses, granites, and migmatites. Structurally highest is the Tethyan Himalaya, largely made up of Neoproterozoic-Paleogene sedimentary and metasedimentary rocks that comprise the cover rocks of the former Indian passive margin and are mostly exposed in areas located north of the Himalayan crest.
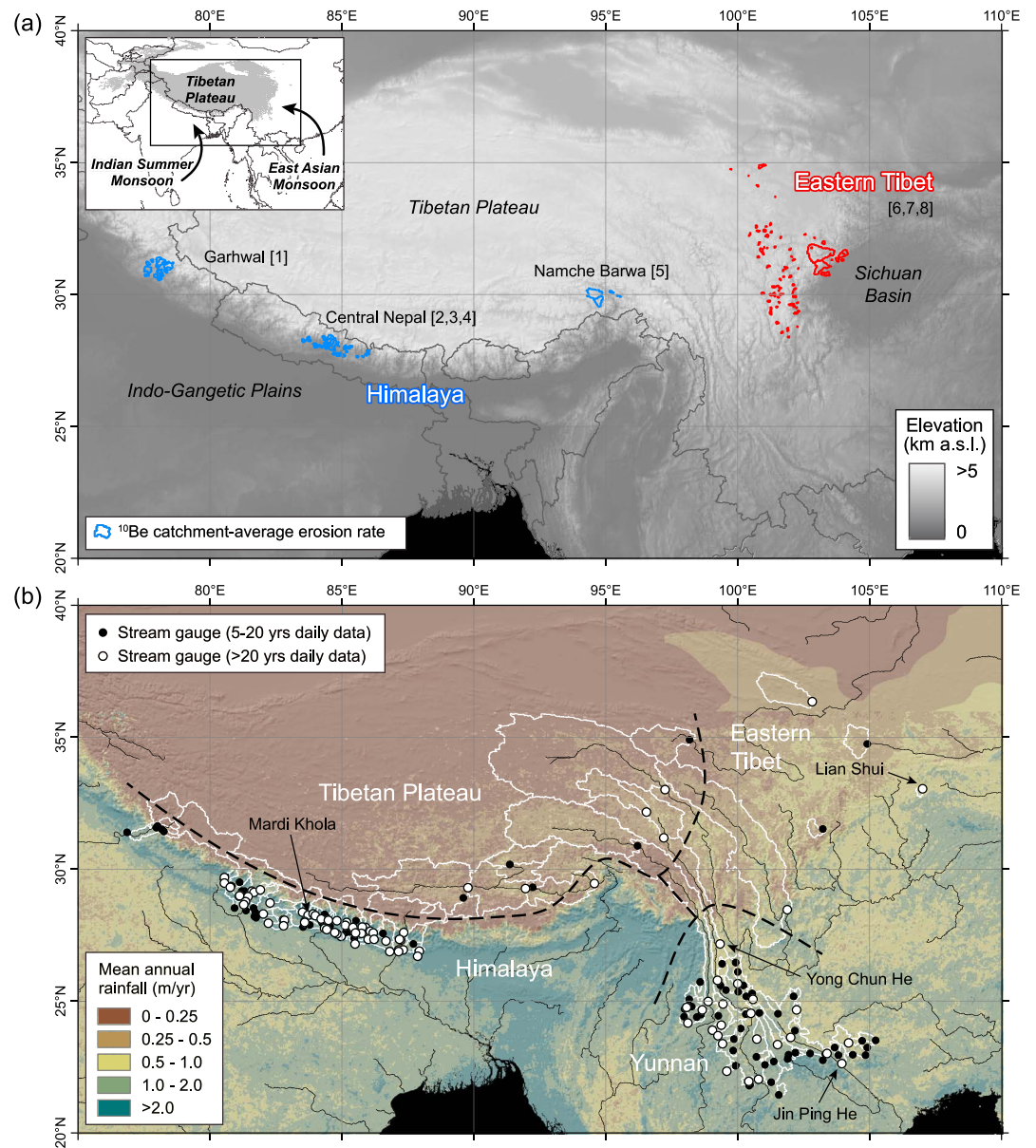
Figure 1. Overview of the study area and data sets. (a) Digital elevation model (DEM) with drainage areas of published [10]Be catchment-average erosion rates. Himalayan data sets (blue): (1) *Scherler et al.* [2014a]; (2) *Wobus et al.* [2005]; (3) *Godard et al.* [2012]; (4) *Godard et al.* [2014]; (5) *Finnegan et al.* [2008]. Eastern Tibet data sets (red): (6) *Harkins et al.* [2007]; (7) *Ouimet et al.* [2009]; (8) *Godard et al.* [2010]. The gray lines indicate political borders. (b) Mean annual rainfall based on Tropical Rainfall Measuring Mission (TRMM) data (provided by B. Bookhagen, http://www.geog.ucsb.edu/~bodo/TRMM/) for latitudes ≤36° and Global Precipitation Climatology Center (GPCC) data [*Meyer-Christoffer et al.*, 2011] for latitudes >36°. The black and white circles give locations of stream gauges with 5–20 yr and >20 yr of daily discharge observations, respectively. The black lines are rivers, and the white polygons delineate drainage areas. The dashed black lines demarcate geographic zones used to differentiate the discharge data.

For our analysis, we compiled [10]Be concentrations of river sediments from five published data sets from the Himalaya (*n* = 67 samples) [*Wobus et al.*, 2005; *Finnegan et al.*, 2008; *Godard et al.*, 2012, 2014; *Scherler et al.*, 2014a] and recalculated catchment-averaged erosion rates following the approach of *Scherler et al.* [2014a] (Table S1 and Text S1 in the supporting information). Catchments are draining a suite of high-grade metamorphic, intrusive, low-grade metamorphic, and sedimentary rocks. We performed simple lithological classification of the catchments into dominantly (>50%) high-grade metamorphic and intrusive rocks versus low-grade metamorphic and sedimentary rocks (Table S2), based

on information and geological maps provided in the original papers, and a 1:1,500,000 geological map of the Tibetan Plateau and adjacent areas [*Pan et al.*, 2004]. We note that several other [10]Be data sets from the Himalaya were published after we had assembled the data set used in this study. They cover study areas in Ladakh [*Munack et al.*, 2014; *Dietsch et al.*, 2015], Bhutan [*Portenga et al.*, 2015; *Le Roux-Mallouf et al.*, 2015; *Adams et al.*, 2016], Garhwal [*Morrell et al.*, 2015], eastern Nepal [*Olen et al.*, 2015], Sikkim [*Abrahami et al.*, 2016], and Himashal Pradesh [*Olen et al.*, 2016]. The data from Ladakh would be difficult to include in our analysis due to the lack of discharge data from this arid region. Most of the other data sets occupy areas of the erosion rate-k_{sn} space where we have a lot of data (and scatter) already.

We analyzed the topography of each sample catchment, using a 90 m resolution Shuttle Radar Topography Mission (SRTM) digital elevation model (DEM) [*Farr et al.*, 2007], in which gaps have been filled with data from topographic maps (http://viewfinderpanoramas.org/dem3.html; by *de Ferranti* [2014]) and the TopoToolbox v2 [*Schwanghart and Scherler*, 2014]. We analyzed stream profiles by measuring their concavity index (θ) and calculating the normalized catchment-average channel steepness index based on $\theta_{ref} = 0.45$ (Text S2 and Table S2).

3.1.2. Eastern Tibet

The second region comprises the eastern margin of the Tibetan Plateau, including the Longmen Shan, which together we refer to as "Eastern Tibet" for brevity. Coming from the Sichuan Basin with surface elevations of a few hundred meters, the topography rises steeply over a very short distance across the Longmen Shan but does not reach as high elevations as in the Himalaya, and stays below 5 km across most of the region. This region is tectonically active, as evidenced for example by the M_w 7.9 Wenshuan Earthquake in 2008 [e.g., *Zhang et al.*, 2010], but rock uplift rates are on average lower than in the Himalaya [*Kirby et al.*, 2002; *Kirby and Ouimet*, 2011]. Most crustal thickening is considered to have occurred during the Cenozoic and to be the result of outward lower crustal flow from beneath the high central Tibetan Plateau [*Royden et al.*, 1997; *Kirby and Ouimet*, 2011]. Exhumation rates based on low-temperature thermochronology are generally lower than in the Himalaya and appear to be as high as 1–2 mm yr^{-1} near the mountain front, but much lower in more interior parts [e.g., *Kirby et al.*, 2002]. Precipitation in Eastern Tibet is sourced from the East Asian monsoon and occurs also mostly during summer [e.g., *Miehe et al.*, 2001]. Compared to the Himalaya, peak elevations and ice coverage are lower in this region, as is the spatial variability of precipitation (Figure 1b).

Most of the rocks in Eastern Tibet have been assembled in their present position during a Mesozoic transpressional event that involved Precambrian basement rocks and Neoproterozoic through Permian cover rocks, which formed the passive margin of the Yangtze Craton [e.g., *Burchfiel et al.*, 1995]. During this orogeny, a thick sequence of flysch sediments (the Songpan-Ganzi flysch) was deposited directly to the west and was later thrusted onto the Yangtze Craton during its collision with the North China block. The Songpan-Ganzi flysch is now exposed in large areas west of the Longmen Shan and contains several Mesozoic intrusive rocks that are typically several 100 km^2 in map-area [*Pan et al.*, 2004]. Present-day rock uplift in Eastern Tibet is less well defined compared to the Himalaya but appears to be focused in the Longmen Shan and to level off toward the east [*Kirby et al.*, 2003].

We compiled three detrital [10]Be data sets from Eastern Tibet ($n = 82$) [*Harkins et al.*, 2007; *Ouimet et al.*, 2009; *Godard et al.*, 2010] and recalculated catchment-averaged erosion rates and drainage network geometries as described above for the Himalaya and detailed further in Texts S1 and S2 and Tables S1 and S2). We note that the recently published [10]Be-data set by *Ansberque et al.* [2015] from Eastern Tibet, which is not included here, occupies the same erosion rate-k_{sn} space as the earlier data sets.

3.2. Regional Differences in Erosional Efficiency

Figure 2 shows the recalculated [10]Be-derived catchment-average erosion rates as a function of normalized channel steepness index, k_{sn}. In the Himalaya (Figure 2b), the data span k_{sn} values of approximately 50 to 400 m$^{0.9}$ and erosion rates of 0.1–3.5 mm yr^{-1} (Table S2). There is no discernible difference in the k_{sn}-erosion rate relationship between samples from rivers that drain mostly low-grade metamorphic rocks (LHS) and those from catchments that drain mostly high-grade metamorphic and magmatic rocks (HHS). This observation is consistent with the analysis of *Lavé and Avouac* [2001], who estimated that
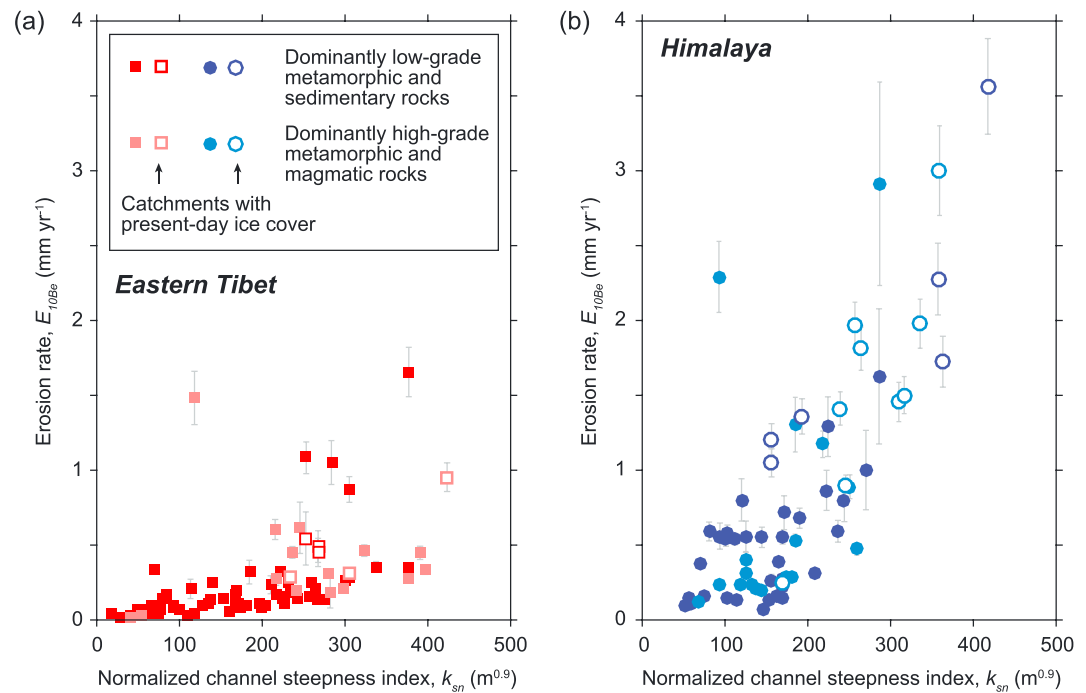
Figure 2. Catchment-average erosion rates, $E10Be$, and normalized channel steepness indices, k_{sn}, for (a) Eastern Tibet (red squares) and (b) the Himalaya (blue circles). The dark and light colors distinguish between dominant (>50% by area) rock types within the catchment. The filled and open symbols denote catchments with no and 1–20% present-day ice cover, respectively.

differences in erodibility between LHS and HHS rocks are ~20%, which is a value that is well within the scatter and uncertainty of the ^{10}Be data. In Eastern Tibet (Figure 2a), the data span a similar range of k_{sn} values, from ~15 to 400 m$^{0.9}$, but the corresponding erosion rates reach a maximum value of ~1.7 mm yr^{-1}, and for most samples erosion rates are <0.5 mm yr^{-1}. Like in the Himalaya, there exists no systematic offset of the channel steepness-erosion rate relationship that could be confidently linked to different rock erodibility, as already observed by *Kirby and Ouimet* [2011], although most of the higher erosion rate samples drain catchments where crystalline rocks are dominantly exposed.

In both regions, we observe several samples that plot with significantly higher erosion rates than the trend. Some of these samples stem from the glaciated Gonga Shan massif and have been noticed and excluded from more detailed analysis in the original study [*Ouimet et al.*, 2009], as they were considered to be affected by landslides and glacially derived sediments. For completeness, we show these data points here but excluded them and other samples that were deemed biased in the original publications. We also excluded samples that stem from catchments with drainage areas <2 km^2 or >1000 km^2, as very small catchments can be biased by landsliding [*Niemi et al.*, 2005; *Yanites et al.*, 2009], and large basins might have problems with temporal variability in sediment supplied from tributaries with different hypsometry and thus ^{10}Be production rates [*Lupker et al.*, 2012] or with spatial variations in climate and rock uplift and associated problems calculating representative k_{sn} values. We also excluded samples from catchments with ice cover >20%, as subglacially derived material that is shielded from cosmic rays can bias estimates of erosion rate [e.g., *Godard et al.*, 2012]. As a result, we used 61 out of 67 samples from the Himalaya and 68 out of 82 samples from Eastern Tibet for further analysis and our modeling in section 5.

Based on the apparent trend of the channel steepness-erosion rate data in the Himalaya and Eastern Tibet, we fit the data with a power law as in equation (1) and using least squares regression (Figure S3a in the supporting information). The resulting relationships differ between the regions. In the Himalaya, the best fit model has a power law exponent ϕ of ~2, whereas in Eastern Tibet, $\phi \sim 1$. In both regions, scatter in the data is quite large and R^2 values are 0.75 and 0.46 in the Himalaya and Eastern Tibet, respectively, suggesting intraregional variability that is not accounted for by channel steepness.

Because the influence of rock type on erosion rate in the Himalaya and Eastern Tibet appears to be negligible (Figure 2) and differences in erodibility (or rock type) within each region are probably higher than between the regions, it appears likely that some of the scatter within and differences between the regions are due to differences in annual runoff that lead to differences in erosional efficiency. In Eastern Tibet, catchment average mean annual precipitation ranges from ~300 to 1300 mm yr^{-1} (Table S2), whereas in the Himalaya it ranges from ~500 to 4500 mm yr^{-1}. Changing mean runoff alone influences erodibility by a factor with an exponent m (see equation (9)), which typically ranges from ~0.3 to 0.8, depending on incision model parameters [*DiBiase and Whipple*, 2011; *Ferrier et al.*, 2013], and is thus insufficient to explain the difference in erosional efficiency between the two landscapes (Figure S3b).

This simple way of factoring-in differences in precipitation does not help to explain the different channel steepness-erosion rate relationships we observe. Possible reasons include the following: (1) precipitation is a poor indicator of stream discharge; (2) there are differences in not just the mean, but also the variability of discharge events between the Himalaya and Eastern Tibet; or (3) we have an incomplete understanding of the way that rock strength and/or erosion thresholds are expressed in these landscapes. For the remainder of this paper, we focus on finding out if a stochastic-threshold SPM is able to explain the systematic regional differences and also the observed scatter within the data from the Himalaya and Eastern Tibet.

4. Discharge Analysis

4.1. Daily Discharge Data

To characterize regional trends in discharge and discharge variability, we compiled daily discharge data from 199 river gauging stations located in China, India, and Nepal (Figure 1b). Most of the Chinese stations are situated in the Yunnan province, and their records have been digitized as part of the China Hydrology Data Project at the University of Washington [*Henck et al.*, 2010]. This data set also comprises a few records from Tibet. We obtained additional records from the Sichuan, Qinghai, Gansu, and Shaanxi provinces through the Global Runoff Data Center, 56068 Koblenz, Germany. Discharge records from Nepal were obtained through the Nepalese Department of Hydrology and Meteorology. Our data from Himalayan rivers in India are restricted to the Sutlej River and tributaries in northwestern India [*Wulf et al.*, 2012].

Prior to the analysis, we examined each of the data sets by plotting the hydrographs and searching for data gaps and unreasonable values. For example, several of the Yunnan station records contained individual years, where daily discharge appeared to be a scaled version of daily discharge in all of the other years, presumably by a factor of ~10 or 1/10. Because we do not know the exact nature of this systematic offset, we excluded the respective years from our analysis. We also excluded years or entire records that contained relatively short data gaps, but always during a particular season of the year. Furthermore, we searched for dams in the drainage areas using Google Earth [http://www.google.com/earth/] and excluded stations where strongly subdued hydrographs suggest dam existence or construction during the time of measurement.

We derived the upstream drainage area for each station using the DEM and the provided coordinates, which we often found to be off the river, sometimes by kilometers. Using Google Earth and an iteration of drainage basin extraction, drainage area calculation, and comparison with published drainage areas, we obtained our best estimate of the true location of the gauging station. We note that in some cases, the published drainage areas appear also to be wrong, as indicated by unreasonably low or high runoff values compared to neighboring stations. In such cases, we retained the station if the published location was very close (<~3 km) to a river so that the obtained and the published drainage areas were within approximately 30%. Otherwise, we discarded the station from our analysis. Details on the discharge stations, including the published and our relocated coordinates and published and recalculated drainage areas, can be found in the data repository in Table S3.

To facilitate regional comparison, we grouped the discharge records, based on the geographic position of their drainage areas, into four regions: Himalaya, Tibet, Yunnan, and Eastern Tibet (Figure 1b). Unfortunately, Eastern Tibet is underrepresented in our data set. On the other hand, we have discharge records from areas in Yunnan and Tibet, for which we are missing erosion rates, and which we therefore do not use in the modeling. We also note at this point that although the erosion rate data from the Namche Barwa area may appear to be within our Tibetan region (Figure 1), this area is, in terms of erosion rates and precipitation, more similar to the Himalaya than to Tibet [*Finnegan et al.*, 2008].
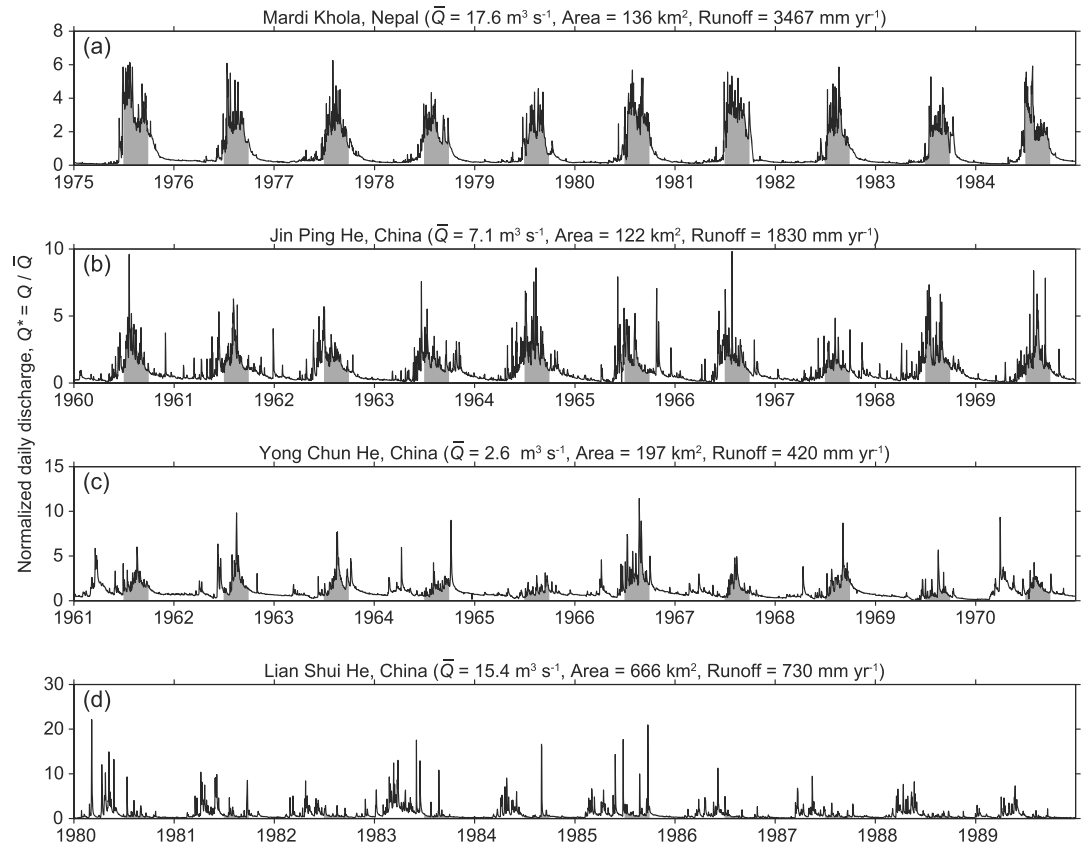
Figure 3. Hydrographs from selected gauging stations showing time series of normalized daily discharge, Q^*. $\overline{Q}$ is mean annual discharge; runoff is $\overline{Q}$ divided by drainage area. See Figure 1b for locations. The shaded areas under the curves mark time periods from July to September, which are also present in panel (d) and in line with those of the other panels, but are difficult to see due to the scale of the figure. Note change in scale of y axis.

4.2. Monsoonal Discharge Regimes

Figure 3 shows 10 year spanning hydrographs from four selected rivers to highlight first-order patterns and differences across our study area (see Figure 1b for locations). The Mardi River is a relatively small ($A = 136$ km^2) tributary of the Seti River in Central Nepal and reflects a typical rainfall-dominated discharge regime in the Himalaya. From the almost 3500 mm yr^{-1} annual runoff, 71% occurs during the months July, August, and September, reflecting the core season of the Indian summer monsoon. Although discharge is high during summer, there is not much variability, neither during the summer, nor between different years. Summer discharge is mostly between two and six times the mean annual discharge, $\overline{Q}$. During the rest of the year (October until June), discharge stays consistently below 2×$\overline{Q}$ and below 0.5×$\overline{Q}$ between November and May.

The Jin Ping River (Figure 3b), located in southern China, is somewhat smaller ($A = 122$ km^2) and has a lower annual runoff (1830 mm yr^{-1}). Despite a pronounced summer discharge maximum, discharge events with more than 2×$\overline{Q}$ occur throughout the year. Compared to the Mardi River, the high-discharge season appears to last longer, discharge variability appears to be higher, and normalized peak discharges reach higher values.

Farther northwest, at the southeastern margin of the Tibetan Plateau, the Yong Chun River in China (Figure 3c) is similar in size ($A = 197$ km^2) to the Mardi River but exhibits much lower mean runoff (420 mm yr^{-1}). The highest discharge events still occur during summer, but the total discharge during the rest of the year is equal in size. High-discharge events appear to be fewer in numbers but have relative magnitudes that are comparable to the Jin Ping River (5–10×$\overline{Q}$).

The Lian Shui River is located near the northern margin of the Szechuan Basin, has a drainage area of 666 km^2, and 730 mm yr^{-1} annual runoff (Figure 3d). Compared to the previous hydrographs, discharge in the Lian Shui River appears more variable, with peak discharge events of up to 20×$\overline{Q}$. Most high-discharge events occur during spring and summer, but in some years high discharges also occur during fall and winter.

In summary, a typical monsoonal discharge regime is characterized by distinct modes of high and low discharges, which are concurrent with the seasonal variation of precipitation. However, the time periods during which these discharge regimes prevail and the discharge variability for each regime may vary depending on climatic gradients. In our presentation of flow regimes so far, we deliberately neglected station records that are dominated by snowmelt -generated runoff, such as those with large drainage areas on the Tibetan Plateau. We will address such catchments in section 4.4.

4.3. Frequency-Magnitude Distribution of Monsoonal Discharges

Turcotte and Greene [1993] and *Molnar et al.* [2006] argued that the exceedance probability distribution of large floods could often be described with a power law, where a lower exponent indicates a heavier tail, and thus a higher variability. However, a power law does not describe well the rollover to infrequent low discharge events [*Lague et al.*, 2005], and, as we will show here, there exist more complex discharge distributions where power law behavior breaks down over a significant range of the discharge distribution. Alternatively, discharge distributions have been described with an inverse gamma distribution that combines an exponential distribution for low discharges with a power law distribution for high discharges [*Crave and Davy*, 2001; *Lague et al.*, 2005; *DiBiase and Whipple*, 2011; *Lague*, 2014]. For the inverse gamma distribution, the probability density function (pdf) of normalized discharge, $Q^* = Q/\overline{Q}$, is:

$$\text{pdf}_{\overline{Q},k}(Q^*) = \frac{k^{k+1}}{\Gamma(k+1)} \exp\left(-\frac{k}{Q^*}\right) Q^{*-(2+k)},$$ (12)

where Γ is the gamma function and k is a dimensionless variability parameter, with higher values reflecting lower variability. The associated cumulative distribution function (cdf) is:

$$\text{cdf}_{\overline{Q},k}(Q^*) = \Gamma(k/Q^*, k+1),$$ (13)

where $\Gamma(a, b)$ is the incomplete gamma function [cf., *Lague et al.*, 2005].

Most of the hydrographs shown in Figure 3 display a bimodal distribution, with a low-flow regime during winter and a high-flow regime during summer. Because these discharge regimes often exhibit different variability, it is difficult to fit the entire discharge distribution with a single inverse gamma distribution. In some regions, however, distinguishing the different flow regimes by their season yields better fits of the data. For the Mardi River in the Himalaya (Figure 3a), two flow regimes can be well captured with different inverse gamma distributions when considering the months July to September, and November to May separately, while omitting the months of June and October, which display a transitional flow regime (Figures 4a and 4b). In this case, the discharge variability of the high- and low-discharge regime is similar ($k_h = 5.2$ and $k_l = 4.2$, respectively), but the mean discharge during the summer is more than 10 times that from November to May. For other station records, it is not always possible to separate different flow regimes based on distinct time periods (cf., Figures 3c and 3d). Yet many of the analyzed records show a pronounced kink in their cdf, indicative of at least two different modes of discharge. Therefore, we fit the cdf of each discharge record with a weighted sum of two inverse gamma distributions, but without imposing any temporal constraints:

$$\text{cdf}_{\overline{Q}_h,\overline{Q}_l,k_h,k_l,f}(Q^*) = f\Gamma\left(k_h/Q_h^*, k_h + 1\right) + (1 - f)\,\Gamma\left(k_l/Q_l^*, k_l + 1\right),$$ (14)

where the subscripts h and l refer to a high- and low-flow regime, respectively, and f is the fraction of the high-flow regime (between 0 and 1). For the Mardi River, the resulting mean discharges ($\overline{Q}_h$, $\overline{Q}_l$) are very close to those obtained by fitting the seasonal data and the discharge variability (k_h, k_l) is almost the same for the high-flow regime, but different for the low-flow regime (Table 1 and Figures 4c and 4d). This is because we have now included the entire record, including the transitional periods during June and October. The fraction of the high-flow regime ($f = 0.26$) corresponds almost exactly to the 3 months during summer, which we previously identified as the core monsoon season of high discharge. Comparison of temporally constrained versus unconstrained fitting of the discharge records from all stations shows that the discharge magnitude
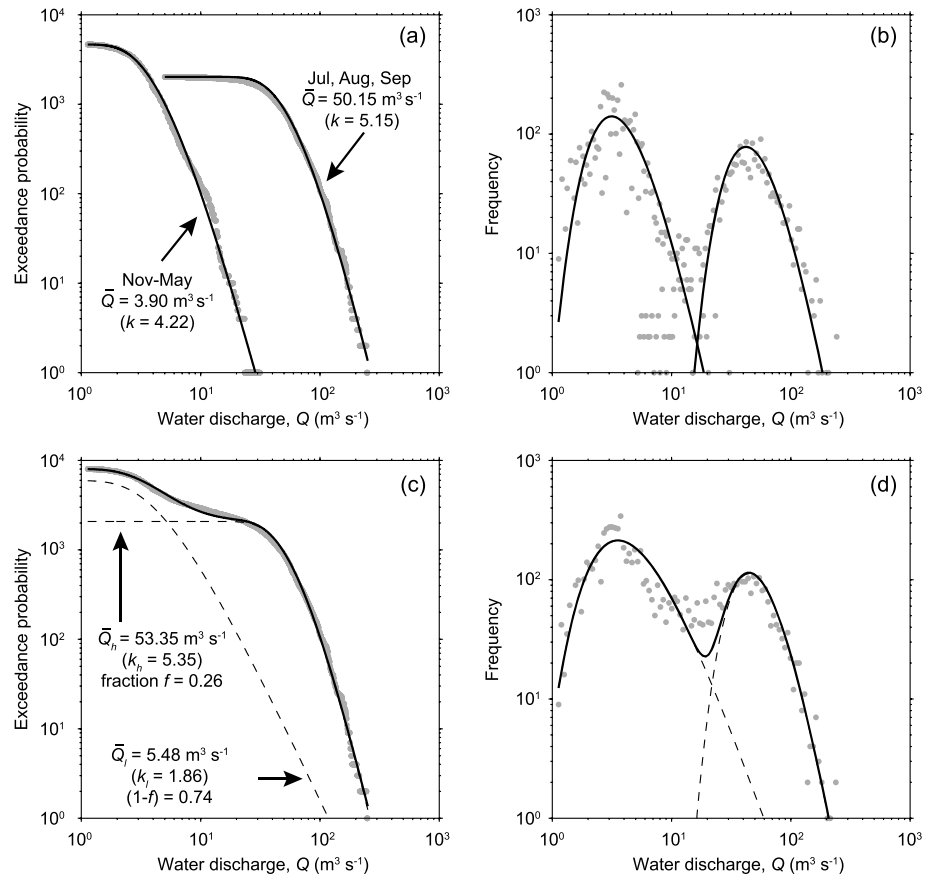
Figure 4. Distribution of daily discharges in the Mardi Khola, Nepal (1974–1995). (a) Number of days with discharge greater than Q for periods from July to September and from November until May, fit with an inverse gamma-distribution model [e.g., *Lague et al.*, 2005]. (b) Frequency-magnitude distribution for the same periods as in Figure 4a. (c) Number of days with discharge greater than Q for the entire year, fit with a weighted sum of two inverse gamma distribution functions (see text for details). (d) Frequency-magnitude distribution for the entire year.

during the summer and winter season is very well captured by the unconstrained fitting, while the discharge variability shows more scatter (Figure S4), which we explain by the loss of a clear seasonal signature when moving northeast in our study area.

Because the daily discharge records have lengths that vary substantially, we assessed the effect of record length on the precision of the fit parameters, based on 43 year long daily discharge records from two rivers in Nepal (Kali Gandakhi and Rapti). We fit daily discharge distributions ranging from 1 to 43 full years that we randomly sampled from the entire record. We repeated this procedure 500 times to obtain reasonable statistics. With increasing sample lengths, each of the best fit parameters asymptotically approaches a long-term stable value, but at shorter sample lengths (below ~10 years), there exists considerable spread (Figure S5). The variance of the discharge variability parameter evolves similarly for the high-flow (k_h) and the low-flow regime (k_l), but at smaller sample numbers, the distributions are skewed toward higher and lower values, respectively. It is also notable that even for sample lengths of >20 years, outliers exist that are sometimes

Table 1. Discharge Variability Parameters for the Mardi Khola, Nepal

		Temporally Constrained Fit		Temporally Unconstrained fit	
Parameter	Symbol	Jul–Sep	Nov–May	High-Flow Regime	Low-Flow Regime
Average discharge (m^3 s^{-1})	$\overline{Q}$	50.15	3.90	53.35	5.48
Discharge variability	k	5.15	4.22	5.35	1.86
Annual fraction	f	0.25	0.58	0.26	0.74
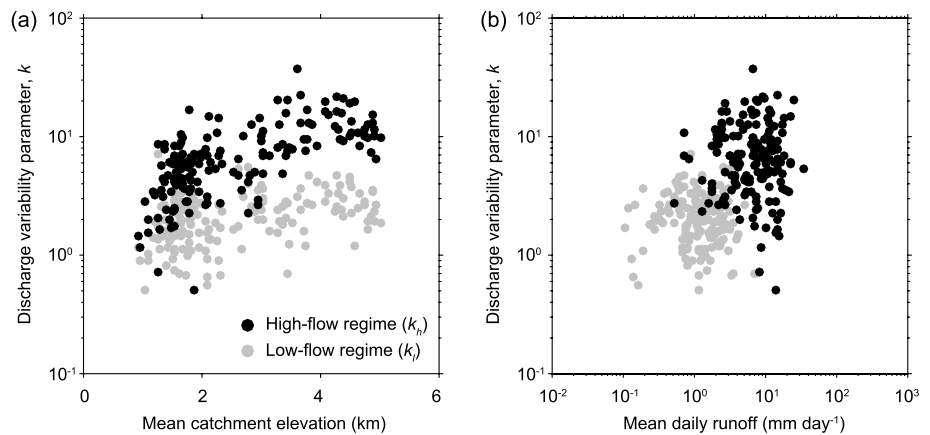
Figure 5. Discharge variability parameter k as a function of (a) mean catchment elevation, as a proxy for increasing contribution of snowmelt runoff, and (b) mean daily runoff during the high- and low-flow discharge regimes. Larger k values reflect lower variability. Only discharge records with lengths >5 years are shown.

far (>50%) from the long-term value. In the two cases considered here, the high-flow fraction f is approximately 0.25. In the case of yet lower high-flow fractions, the number of observations for a given record length that can be used to define the discharge variability of the high-flow regime will be fewer. Most likely, this will also affect how well the parameter can be recovered. The fact that both k_h and k_l appear similarly sensitive to record length despite a factor of 3 difference in their share of the entire record (~25% versus ~75%) can be explained by the differences in variability (k values): when discharge variability is high (k values are low), more observations are needed to recover rare events. The influence of record length on f will also affect the mean discharges during the high- and low-flow regime, which have to obey $\overline{Q} = f\overline{Q}_h + (1-f)\overline{Q}_l$. In fact, the highest $\overline{Q}_h^*$ values across the study area are associated with the lowest f values (Figure S6).

In summary, while record length does affect the precision at which we can constrain the parameters in equation (14), it is difficult to define a minimum record length. Based on qualitative assessment, we chose a minimum duration of 5 years and excluded records with lengths <5 years from our further analysis. We also excluded records in which the fit yielded f values lower than 0.07, as the corresponding Q_h^* values appear anomalously high (Figure S6), although they may be correct.

4.4. Regional Patterns of Monsoonal Discharge Variability

Before addressing regional similarities and differences in discharge variability that may be linked to climate in one way or the other, we assessed potentially important influences of drainage area, snowmelt, and runoff on the observed discharge variability. Analysis of discharge records from drainage basins in the Lesser Himalaya of Nepal, which have variable sizes, but are all developed in similar lithology and experience similar snow-free climate, suggests that daily discharge variability shows no trend with drainage area below ~5000 km², which is above the upper size limit of the catchments with ^{10}Be-derived erosion rates (Figure S7). It is well known that snowmelt-dominated runoff regimes are different from rainfall-dominated runoff regimes [e.g., *Pitlick*, 1994], but we have no information on the actual contribution of snowmelt to the measured discharges, except for the Sutlej River [*Wulf et al.*, 2015]. Comparison of discharge variability with catchment mean elevation as a proxy for snowmelt-dominated runoff suggests that both k_h and k_l increase with snowmelt runoff, although there exists considerable scatter (Figure 5a). Provided that mean catchment elevation does not correlate with any other factors that influence discharge variability, a higher contribution of snowmelt to discharge lowers discharge variability. Finally, we compared the low- and high-flow discharge variability with the mean daily runoff during the corresponding regimes (Figure 5b). Although discharge variability during the high-flow regime is on average lower (higher k values), we found no systematic trend within the data of a given regime.

The above analysis indicates that the amounts of snowmelt likely have an influence on discharge variability and that some of the modeled parameters may be sensitive to limited record lengths. Despite these complicating factors, and a large range of mean annual runoff within the entire study area, it is
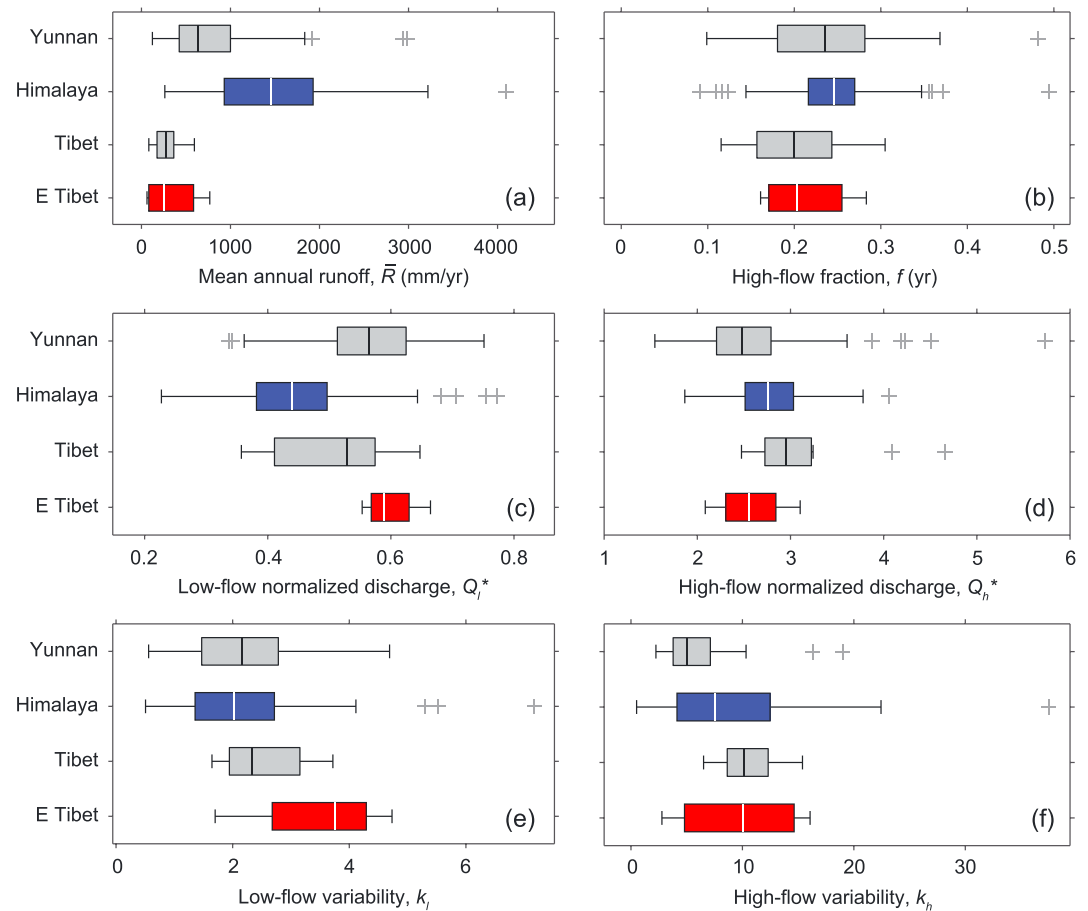
Figure 6. Regional characteristics of discharge variability. (a) Mean annual runoff, $\bar{R}$. (b) Fraction of high-flow regime, f. (c) Normalized mean discharge during the low-flow regime, Q_l^* and (d) during the high-flow regime, Q_h^*. (e) Discharge variability for the low-flow regime, k_l and (f) for the high-flow regime, k_h. The boxes correspond to central 50% of the data with the median values indicated by vertical bars. The whiskers extend to the last data point that is within a distance of 1.5 times the interquartile (25–75%) data range. The crosses denote data points beyond this distance. Number of samples per region: Yunnan = 68, Himalaya = 91, Tibet = 11, Eastern Tibet = 5. Only discharge records with lengths >5 years were used.

remarkable that regional differences in the discharge variability parameters are relatively small (Figure 6). Specifically, the discharges during the high- and low-flow regime are remarkably similar between the regions when normalized to the mean annual discharge, although low-flow discharges are on average higher in Eastern Tibet compared to the Himalaya (*t* test: $\alpha = 0.05$, $p = 0.029$) (Figure 6c). In addition, the annual fraction of the high-flow regime, f, typically ranges between 0.15 and 0.3, that is, approximately 2–4 months, with little variation between the regions and no significant difference between the Himalaya and Eastern Tibet ($p = 0.41$) (Figure 6b). In other words, despite pronounced regional differences in mean annual runoff, $\bar{R}$ (Figure 6a), its decomposition into low- and high-flow regimes is similar.

The highest discharge variability, on average, in the high-flow regime (low k_h values) occurs in Yunnan, and the lowest variability occurs in Tibet and Eastern Tibet (Figure 6f), as we would expect from the absence and dominance in snowmelt runoff, respectively. The differences in k_h values between the Himalaya and Eastern Tibet are not significant ($p = 0.5$). While the low-flow discharge variability appears on average lower (higher k_l values) in Eastern Tibet than in the Himalaya, this difference is statistically not significant ($p = 0.47$) (Figure 6e). Summaries of regional statistics of the fit discharge parameters are given in Table 2, showing that the largest difference in discharge between the Himalaya and Eastern Tibet is related to mean annual runoff, whereas differences in mean high-flow discharge and discharge variability are rather small.

**Table 2.** Regional Statistics of Fit Discharge Parameters

		Q_h^*		Q_l^*		k_h		k_l		f	
Region	N^a	Mean ± 1σ	Median	Mean ± 1σ	Median	Mean ± 1σ	Median	Mean ± 1σ	Median	Mean ± 1σ	Median
Himalaya	82	2.81 ± 0.41	2.76	0.44 ± 0.12	0.43	8.88 ± 6.50	7.53	2.18 ± 1.13	2.02	0.24 ± 0.06	0.25
Tibet	11	3.16 ± 0.66	2.95	0.51 ± 0.11	0.53	10.49 ± 2.63	10.16	2.50 ± 0.71	2.33	0.21 ± 0.06	0.20
Eastern Tibet	4	2.57 ± 0.42	2.55	0.61 ± 0.05	0.60	9.72 ± 6.03	10.02	3.49 ± 1.28	3.75	0.21 ± 0.05	0.20
Yunnan	670	2.65 ± 0.72	2.485	0.57 ± 0.11	0.57	5.77 ± 2.99	5.05	2.17 ± 0.95	2.02	0.23 ± 0.08	0.24

[a]Only stations with discharge records longer than 5 years and a minimum f value of 0.07 were considered in the statistics. See text for details.

4.5. Discharge Estimates From Gridded Precipitation Data

Our aim is to obtain a better understanding of how climatic variations and associated changes in discharge affect erosion rates. But for most of the catchments with erosion rate data, we do not have any discharge records. In relatively small ($<10^3$ km²) drainage basins, however, it is reasonable to assume uniform climatic conditions and that the mean annual runoff, $\overline{R}$, can be related to the mean annual precipitation, $\overline{P}$, and mean annual losses due to interception and evapotranspiration, $\overline{ET}$, by $\overline{R} = \overline{P} - \overline{ET}$ [*Tucker and Bras*, 2000]. $\overline{ET}$ is likely a complex function of climate, soil, vegetation, and highly variable throughout the study area, which makes it difficult to calibrate. Thus, we opted for an empirical approach to link $\overline{R}$ and $\overline{P}$ by using gridded climatic data sets that allow us to derive $\overline{R}$ for the drainage areas of both the erosion rate sample catchments and the discharge stations. We derive the mean annual discharge, $\overline{Q}$, for any catchment by multiplying $\overline{R}$ with the drainage area. Because precipitation is difficult to constrain in high mountain regions, and there are advantages and disadvantages of alternate approaches to obtain precipitation maps, we compared four gridded climatic data sets that are based on different inputs (see Text S3 and Figure S8).

For our analysis, we focus on two data sets that show reasonably good agreement with discharge data (Figure 7). The first data set comprises a global 4 km resolution grid of mean annual rainfall [provided by B. Bookhagen; http://www.geog.ucsb.edu/~bodo/TRMM/] that was derived from the 2B31 data set of the spaceborne Tropical Rainfall Measuring Mission (TRMM) [*Kummerow et al.*, 1998]. Because this TRMM data set comprises only 12 years (1998–2009), we also used the 0.25°-resolution map of mean annual precipitation from the Global Precipitation Climatology Centre (GPCC), which is mainly based on weather station records from the period of 1951–2000 [*Meyer-Christoffer et al.*, 2011]. For each catchment, we calculated the mean annual precipitation (MAP) as the arithmetic mean from nearest-neighbor interpolation of each precipitation data set to the DEM-based drainage areas. To determine an empirical relationship between mean runoff and MAP, we fit a second order polynomial to the data of catchments for which we have discharge data.
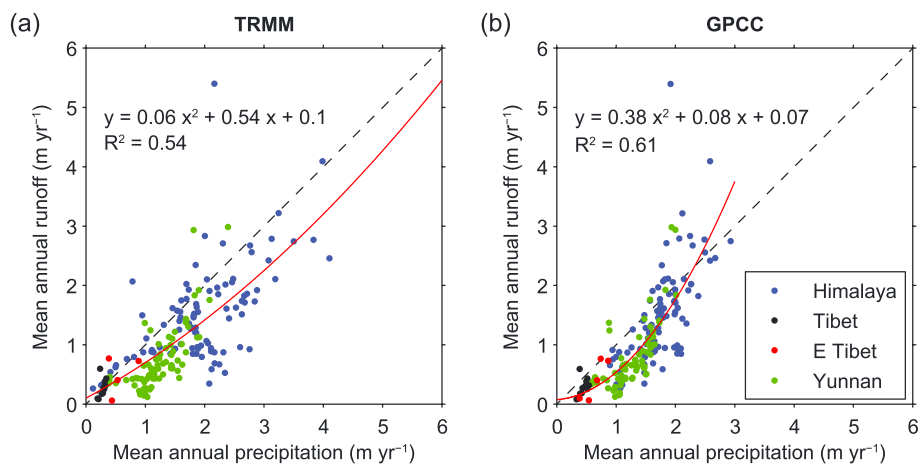
Figure 7. Comparison of mean annual runoff derived from stream gauges with mean annual precipitation derived from (a) the Tropical Rainfall Measuring Mission (TRMM) [*Kummerow et al.*, 1998] and (b) the Global Precipitation Climatology Centre (GPCC) [*Meyer-Christoffer et al.*, 2011]. The red curves depict fitted second order polynomials given by equation.

To determine the mean annual runoff for ungauged basins for which [10]Be-derived erosion rates exist, we measured mean annual precipitation from the GPCC and TRMM data sets and used the empirical relationships calibrated to the discharge station data (Figure S8). Because the discharge variability parameters (k_h, k_l) do not display any significant spatial trends, we simply used the regional median values from the Himalaya and Eastern Tibet and did not vary them any further from basin to basin. Although one could include an elevation-dependent k (Figure 5a), such changes in discharge variability only minimally affect erosional efficiency, as shown below (section 5.6).

## 5. Application of the Stochastic-Threshold Stream Power Model

5.1. Rationale

Our analysis of gridded precipitation and daily discharge data from the study area in the previous section has yielded a model that allows us to represent the pdf of daily discharges in equation (10) with reasonable accuracy. Although the discharge data span time periods of a few decades at most, the similarity in flow regimes over a large region argues for a systematic discharge variability that we assume is also characteristic over the integration timescales of the [10]Be erosion rate measurements (hundreds to thousands of years). In the following section we will use this discharge model in conjunction with the stochastic-threshold stream power model (stochastic-threshold SPM) from section 2 to determine (a) if the difference in erosional efficiency between the Himalaya and Eastern Tibet can be explained by differences in discharge regimes and (b) the extent to which changes in monsoon intensity influence the relationship between channel steepness and erosion rate. Prior to that, we will first specify the other variables and parameters that we need for the modeling.

5.2. Channel Width-Discharge Relationship

One of the important properties of river channels that dictate the energy expenditure of flowing water on its bed is the channel width [*Bagnold*, 1977]. To constrain the channel width index, k_w, (equation (6)) in the study areas, we mapped channel widths from high-resolution satellite images in Google Earth using the *ChanGeom* technique [*Fisher et al.*, 2013]. Bankfull channel margins were hand-digitized in Google Earth using scour, vegetation, and sediment trimlines as well as staining on bedrock walls. We mapped channel widths only for a fraction of the catchments for which [10]Be-derived erosion rates have been measured: 18 out of 61 in the Himalaya and 18 out of 68 in Eastern Tibet (see Figure S9 for spatial distribution). For most of the sampled catchments, river channels were difficult to observe due to lack of high-spatial resolution imagery, poor image orthorectification, and/or channel obstruction due to topographic shadowing, clouds, and vegetation coverage. Channel polygons were then processed using the *ChanGeom* algorithms to create a channel width measurement every 1–3 m along the channel. Channel width errors associated with the technique have been shown to be negligible when compared to field and lidar data sets and depend on the resolution of the rasterized polygon and the underlying resolution of the imagery [*Fisher et al.*, 2013]. In this study, image resolution ranged from 1 to 3 m, yielding an overall channel width error estimate of ~5%, based on the analysis in *Fisher et al.* [2013]. Drainage areas were derived from the 90 m resolution SRTM DEM and mean annual discharge was based on the calibrated TRMM and GPCC data sets (see section 4.5).

When considering the channel width data for each of the measured reaches individually, there exists considerable scatter and the power law fits have coefficients of determination that are on average only ~0.27 (Table S4). We attribute most of the scatter to small-scale variations that include nonuniform lithological conditions, including structural heterogeneities and alluvial reaches [e.g., *Duvall et al.*, 2004; *Allen et al.*, 2013], and transient obstructions and responses to landslides and debris flows [e.g., *Korup*, 2006; *Ouimet et al.*, 2008]. These factors tend to be averaged out when merging the measurements from different rivers (Figure 8). The best power law fit for all our data from the Himalayan channels yields a scaling exponent ω_b, of 0.38. This exponent is similar to the one obtained by *Craddock et al.* [2007] from field measurements of much smaller tributaries ($<$12.4 km^2) of the Marsyandi River in Nepal, sourced primarily from monsoon discharge. Work along the larger Goriganga River in northern India (480–2230 km^2) yields scaling exponents ranging from -1.2 to 4.4 across different tectonic units, with an overall exponent of 0.23 [*Fisher et al.*, 2012], potentially pointing at a discrepancy between channel-width scaling in large river systems and those studied here. In Eastern Tibet, the power law exponent is somewhat lower (0.34), which is largely due to a few relatively wide channels with low discharge and relatively narrow channels with very high discharge (Figure 8b). Data on
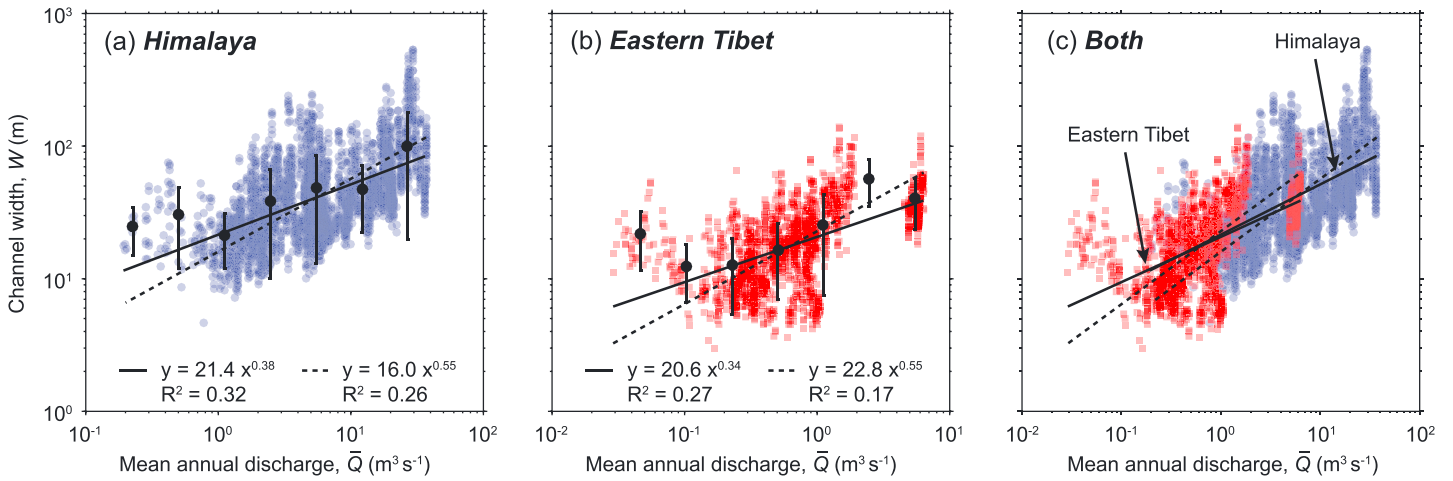
Figure 8. Channel width-discharge scaling in the (a) Himalaya and (b) Eastern Tibet. The black dots represent log-binned averages ($\pm 1\sigma$). (c) The data from both regions together. Power law models were fitted to all data points. The dashed lines indicate fits in which the power law exponent in equation (6) is fixed to 0.55, which is required for the SPM in equation (9),to remain dimensionally correct when $\theta_{ref} = 0.45$. Discharge is based on Tropical Rainfall Measuring Mission (TRMM) data. See text for details.

large river systems in Eastern Tibet (10^2 to 10^4 km^2) produce scaling exponents ranging from 0.36 to 0.63 with drainage area [*Kirby and Ouimet*, 2011].

For the stochastic-threshold SPM to be dimensionally correct (see section 3), the exponent ω_b is coupled to the resistance relation and the choice of the reference concavity, θ_{ref} [*DiBiase and Whipple*, 2011]. A Darcy-Weissbach resistance relation and a reference concavity of 0.45 yield a reference $\omega_{b,ref}$ value of 0.55, which we used in our modeling. When keeping the power law exponent constant and forcing the fit of equation (6) through our data, the normalized channel width indices, $k_{wn} = W/Q^{\omega_{b,ref}}$ [*Turowski et al.*, 2008; *Lague*, 2014], are in both regions <30% different from the values of the unconstrained fit, with ω_b values of 0.38 in the Himalaya and 0.34 in Eastern Tibet (Figure 8). In our modeling, we used regionally constant k_{wn} values of 16 m$^{-0.65}$ s$^{0.55}$ for the Himalaya and 23 m$^{-0.65}$ s$^{0.55}$ for Eastern Tibet. The dependence of Q_c^* on k_w in equation (11) introduces a nonlinear effect that makes determining the influence of changing channel width nontrivial [*Lague*, 2014]. However, neglecting threshold effects ($\tau_c = 0$), we can estimate the change in erosional efficiency through changes in k_{wn} from equation (9). Assuming $a\alpha \approx 1$, the ~25% lower k_{wn} values in the Himalaya compared to Eastern Tibet result in approximately 25% greater erosional efficiency, which is much less than what we observe. If we were to account for all of the observed ~5 times increase in erosional efficiency at k_{sn} values >300 m$^{0.9}$ (Figure 2) with regional differences in channel width, k_{wn} values would have to be 5 times higher in Eastern Tibet compared to the Himalaya.

5.3. Incision Threshold

Most bedrock rivers do not expose bedrock across their entire bed; instead they often have parts of their bed mantled by a thin veneer of sediment [e.g., *Tinkler and Wohl*, 1998; *Whipple*, 2004; *Turowski et al.*, 2008]. The threshold shear stress, τ_c, in equation (4) can thus be interpreted to reflect, at a minimum, the bed shear stress that is needed to mobilize alluvial bed material before bedrock incision can occur, and potentially much greater if erosion by plucking is important [*Snyder et al.*, 2003]. Following previous studies [e.g., *Lavé and Avouac*, 2001; *DiBiase and Whipple*, 2011; *Attal et al.*, 2011], we assume that the threshold shear stress, τ_c, can be approximated by the shear stress required for initial motion of sediment using a *Shields* [1936] criterion:

$$\tau_c^* = \frac{\tau_c}{D_{50} g (\rho_s - \rho_w)}, \tag{15}$$

where τ_c^* is the Shields number, D_{50} is the median grain diameter, g (9.81 m s^{-2}) is gravitational acceleration, and ρ_s (2.7 g cm^{-3}) and ρ_w (1 g cm^{-3}) are the densities of the sediment and water, respectively. Because we have no constraints on the magnitude of τ_c in the studied rivers of the two regions, we chose the incision threshold to be a free parameter in our modeling, but with different degrees of simplification.
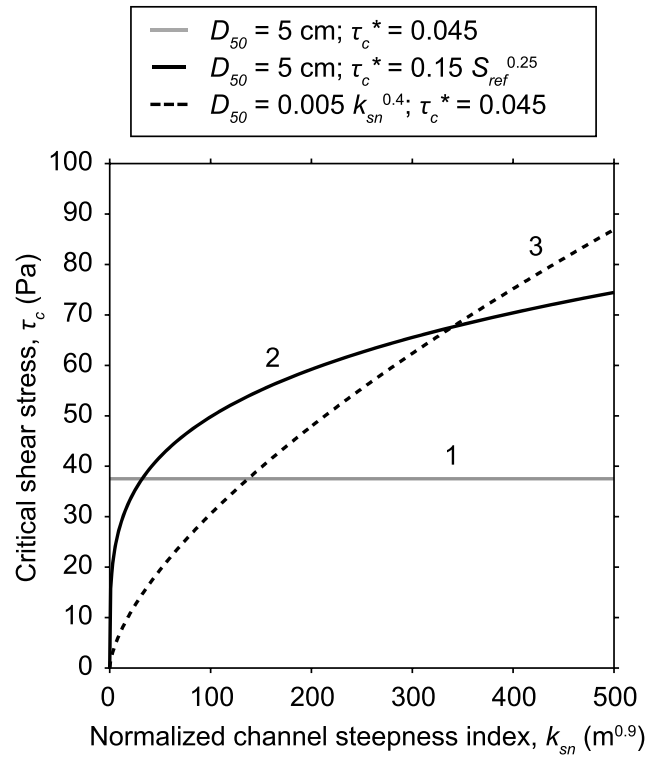
Figure 9. Relationship between critical shear stress, τ_c, and channel steepness index, k_{sn}, that were used in this study: (1) Median grain size, D_{50}, and Shields number, τ_c^*, are constant. (2) Constant D_{50}, but τ_c^* depends on channel slopes [*Lamb et al.*, 2008]. Reference channel slopes, S_{ref}, are calculated with equation (2), based on k_{sn} and a reference drainage area ($A_{ref} = 100$ km^2). (3) k_{sn}-dependent D_{50} and slope-dependent τ_c^*. See text for details.

Lavé and Avouac [2001] estimated the Shields number to be 0.03 based on river incision in the sub-Himalaya of central Nepal. This value is at the lower end of the 0.03–0.08 range of values reported in the literature [*Buffington and Montgomery*, 1997]. Here we initially assumed a constant Shields number of 0.045 [*Miller et al.*, 1977; *Yalin and Karahan*, 1979], and a median grain size that is regionally uniform, which implies that threshold shear stresses are uniform across all catchments (Figure 9, curve 1). Such a simplification appeared justified in a similar study from the San Gabriel Mountains, in which grain sizes showed no systematic trend with channel steepness in basins with drainage areas <100 km^2 [*DiBiase and Whipple*, 2011]. As grain sizes tend to decrease during transport for large river systems [see *Attal and Lavé*, 2006, and references therein], some studies implemented a power law scaling between grain size and drainage area [e.g., *Lavé and Avouac*, 2001]. However, we lack suffi-cient observational constraints from our study regions to calibrate such a model. Furthermore, simple downstream fining relationships are complicated to apply in mountainous regions due to tributary input of coarse material [*Rice et al.*, 2001]. Indeed, a detailed study of bed load along the Marsyandi River, cen-tral Nepal, yielded no downstream fining, but instead slight coarsening of grain sizes [*Attal and Lavé*, 2006]. We next relaxed our simplifying assumption of uniform grain sizes and constant threshold shear stress in two ways. First, we considered spatial variability in the Shields number (τ_c^*) as a function of channel slope [*Lamb et al.*, 2008] according to:

$$\tau_c^* = 0.15 \, S^{0.25}. \tag{16}$$

The increase of critical shear stress for initial sediment motion with slope is considered to be the combined effect of grain emergence, changes in local flow velocity, and turbulent fluctuations that result in a concur-rent increase in the ratio of bed-roughness scale to flow depth [*Lamb et al.*, 2008; *Prancevic and Lamb*, 2015]. To be applicable in our modeling scheme, we tested the effects of equation (16) by replacing S with a reference slope, S_{ref}, that we calculated based on k_{sn} and a reference drainage area ($A_{ref} = 100$ km^2) (Figure 9, curve 2). The resulting τ_c^* values ranged from 0.038 ($k_{sn} = 16$ m$^{0.9}$) to 0.085 ($k_{sn} = 418$ m$^{0.9}$).

Second, we considered spatial variability in bed load grain sizes that may be related to different degrees of physical disintegration and chemical weathering. The idea is that hillslope sediment in slowly eroding land-scapes has on average a smaller grain size, because it is exposed for a longer time to weathering processes [*Sklar and Dietrich*, 2006; *Sklar et al.*, 2016]. In a recent study from northern California, *Attal et al.* [2015] observed that characteristic hillslope and bed load grain sizes both increase with stream power, a quantity that is similar to channel steepness. Based on their data, *Attal et al.* [2015] suggest a power law dependency of grain size on stream power with an exponent <1. To examine the effects of such a relationship on our stochastic-threshold SPM, we adopted a similar relationship with channel steepness of the form

$$D_{50} = k_{50} \, k_{sn}^{q} \tag{17}$$

Table 3. Constant Parameters Used in the Model

Parameter	Value	Unit	Description	Equation
a	3/2	dimensionless	Stream power law exponent	(4)
k_t	1000	(kg m$^{-7/3}$ s$^{-4/3}$)	Flow resistance factor	(5)
α	2/3	dimensionless	Exponent in the flow resistance equation	(5)
β	2/3	dimensionless	Exponent in the flow resistance equation	(5)
θ_{ref}	0.45	dimensionless	Reference channel concavity	(2)
ρ_w	1	(g cm^{-3})	Density of water	(15)
ρ_s	2.7	(g cm^{-3})	Density of sediment	(15)
τ_c^*	0.045	dimensionless	Shield's number	(15)
ω_s	0.25	dimensionless	At-a-station discharge-channel width scaling exponent	(7)
ω_b	0.55	dimensionless	Downstream discharge-channel width scaling exponent	(6)

where k_{50} and q are empirical constants. Because k_{sn} is positively correlated with erosion rates (equation (3); Figure 2), equation (17) relates lower erosion rates, or similarly longer residence time near the Earth's surface and by inference larger degrees of weathering, with smaller grain sizes, and vice versa (Figure 9, curve 3).

Both equations (16) and (17) result in spatially variable threshold shear stress, τ_c, as a function of k_{sn} but for different reasons. While equation (16) modifies the Shields number, τ_c^*, without affecting the median grain size D_{50}, equation (17) does the opposite. The disadvantage of using k_{sn} as the controlling variable is the fact that the data from Eastern Tibet and the Himalaya imply different erosion rates (hillslope residence times) for a given k_{sn}. A possible way to compensate for this would be to use different scaling factors in both regions, but as this adds another parameter that we have no constraints on, we opted for not doing so. Hence, spatial variation in τ_c results in different relative importance of threshold effects as a function of k_{sn} but does not affect first-order regional differences in erosional efficiency.

5.4. Other Constraints and Model Evaluation

The remaining parameters of the stochastic-threshold SPM are shown in Tables 3 and 4. Several of the parameters are common to the two regions (Table 3), such as the stream power law exponent. A value of $a = 1$ was used by *Lavé and Avouac* [2001] in their study of Holocene incision rates in the sub-Himalaya of Central Nepal and the Lesser Himalaya of eastern Nepal. However, we use a value of $a = 3/2$ (corresponding to $n = 1$ when combined with the Darcy-Weissbach resistance relation), based on the assumption that steady state bedrock rivers mantled with sediment are close to being transport-limited, and thus share a similar scaling with shear stress as common bed load transport relationships [e.g., *Whipple and Tucker*, 2002; *Sklar and Dietrich*, 2006; *DiBiase and Whipple*, 2011]. As shown by *Whipple and Tucker* [2002], if the shear stress exponent for detachment-limited incision is greater than that for bed load transport ($n > 1$), channels must become increasingly buried in sediment as relief and erosion rate increase—a process that will tend to force channels into a transport-limited condition in which $n \sim 1$ pertains. Field observations from the Himalaya support the presence of sediments covering actively incising river beds. For example, in the postmonsoon season, extended portions of the Sutlej River fall almost dry, due to diversion of its waters through hydropower

Table 4. Region Specific Parameters Used in the Model

Parameter	Unit	Description	Values	
			Himalaya	Eastern Tibet
k_{wn}	[m$^{-0.65}$ s$^{0.55}$]	Normalized channel width index[a]	16	23
Q_h^*	dimensionless	Normalized high-flow discharge	2.81	2.57
Q_l^*	dimensionless	Normalized low-flow discharge	0.44	0.61
k_h	dimensionless	High-flow discharge variability	8.9	9.7
k_l	dimensionless	Low-flow discharge variability	2.2	3.5
f	dimensionless	High-flow fraction	0.24	0.2[b]

[a]Based on discharge estimates derived from the TRMM data set.
[b]To maintain a normalized mean discharge of 1, this parameter is slightly lower than measured (cf. Table 2).

tunnels, and expose a sediment-mantled river bed. Also note that both values, $a = 1$ and $a = 3/2$, are consistent with erosion by plucking as the main incision process [*Whipple et al.*, 2000a]. We furthermore use the Darcy-Weissbach resistance relation, with $k_t = g^{2/3}\rho_w C_f^{1/3}$, and a choice of friction factor, $C_f = 0.01$, similar to previous studies [*Tucker*, 2004; *DiBiase and Whipple*, 2011]. We note that using a constant friction factor for the case in which we adjust the critical shear stress as a function of slope (equation (16)) is clearly oversimplified, given that flow resistance likely increases with increasing grain size. However, at present we lack empirical control on patterns of flow resistance in mountain streams, and so refrain from adding unconstrained degrees of freedom to our model. The remaining parameter that we did not constrain is the erodibility, k_e, in equation (4), which relates excess shear stress to incision rate. By assuming that hillslope erosion rates are equal to river incision rates, we computed the resulting misfit, φ, between the [10]Be-derived erosion rate ($E_{10Be,i}$) and the corresponding modeled long-term incision rate ($E_{m,i}$) from:

$$\varphi(k_e, \tau_c) = \sum_{i=1}^{n} \left(E_{10Be,i} - E_{m,i}(k_e, \tau_c) \right)^2,$$ (18)

where n is the number of samples. Note that we calculate E_m from $\bar{l}$ in equation (10). While the critical shear stress, τ_c, may or may not depend on additional parameters that are distinct for each [10]Be-sample's drainage area (see section 5.3), the erodibility parameter, k_e, is kept constant for all samples from one or both regions, reflecting our assumption that differences in erodibility are probably larger within each region compared to systematic differences in between the two regions. Note that we did not use the analytical [10]Be uncertainties of each sample as weights when computing the misfits, as the geomorphic uncertainties are likely larger and thus more important, but not well represented by the analytical uncertainties. To account for the analytical uncertainties in the [10]Be data, we used a Monte Carlo simulation in which we randomly draw 500 samples for each $E_{10Be,i}$ from within the range of the measured erosion rates $\pm 2\sigma$. We optimized the choice of the free parameters τ_c and k_e for each or both regions by minimizing the misfit between modeled and [10]Be-derived catchment average erosion rates.

### 5.5. Comparing Model Results With [10]Be-Derived Erosion Rates
5.5.1. Constant Incision Threshold Cases: General Behavior

In our first models, we compared results with [10]Be-derived erosion rates from each region individually, using a constant Shields number ($\tau_c^* = 0.045$) and regionally uniform D_{50}. We explored a wide parameter space, with D_{50} between 0 (no threshold) and 20 cm, and k_e between 10^{-15} and 10^{-10} $m^{2.5}$ s^2 kg^{-1}. Figures 10a–10d show the best fit parameter combinations (left) for each of the 500 Monte Carlo runs (squares), and from the ensemble of all Monte Carlo runs (stars), together with the modeled and [10]Be-derived erosion rates (right) for both regions and for different precipitation data sets. Table 5 lists the best fit parameter combinations. In both regions, the best fit parameter combinations from the 500 Monte Carlo runs define a trade-off between k_e and D_{50}: higher D_{50} require higher k_e, and vice versa. This is because higher D_{50} result in higher threshold shear stresses, and—for a given discharge distribution—fewer discharges that are erosive. To compensate for this reduction, the bedrock erodibility, k_e, needs to be higher.

Modeled and [10]Be-derived erosion rates agree reasonably well for erosion rates $< \sim 2$ mm yr^{-1} in the Himalaya and $< \sim 0.4$ mm yr^{-1} in eastern Tibet. Higher [10]Be-derived erosion rates, however, are associated with consistently too-low modeled erosion rates. In the Himalaya, these data points are associated almost exclusively with catchments with contemporary ice cover. Although it cannot be excluded that subglacially derived sediments bias the erosion rate estimates toward higher values [e.g., *Godard et al.*, 2012], we deem it unlikely that this is the only explanation, because the present-day ice cover in these catchments is small (mostly $<10\%$; Table S1) and for erosion rates >1 mm yr^{-1} the integration timescales are <1000 years; hence, they do not extent into periods like the early Holocene, when ice cover was larger [e.g., *Scherler et al.*, 2010; *Heyman*, 2014]. Furthermore, because we include shielding by ice cover when calculating production rates (see the supporting information), any remaining bias requires a dominant share of subglacial sediments in the collected samples.

In both regions the predictive power of the stochastic-threshold SPM with respect to the [10]Be-derived erosion rates is approximately the same when the mean annual runoff for each sample catchment is based on either the discharge-calibrated TRMM precipitation data set (Figures 10b and 10d) or the GPCC data set (Figures 10a and 10c and Table 5). In addition, for GPCC-derived discharge, most of the [10]Be-derived erosion rates $< \sim 1$ mm yr^{-1} in the Himalaya have modeled values that are systematically too high. A similar systematic bias, but for lower erosion rates ($< \sim 0.3$ mm yr^{-1}), appears less pronounced in Eastern Tibet.
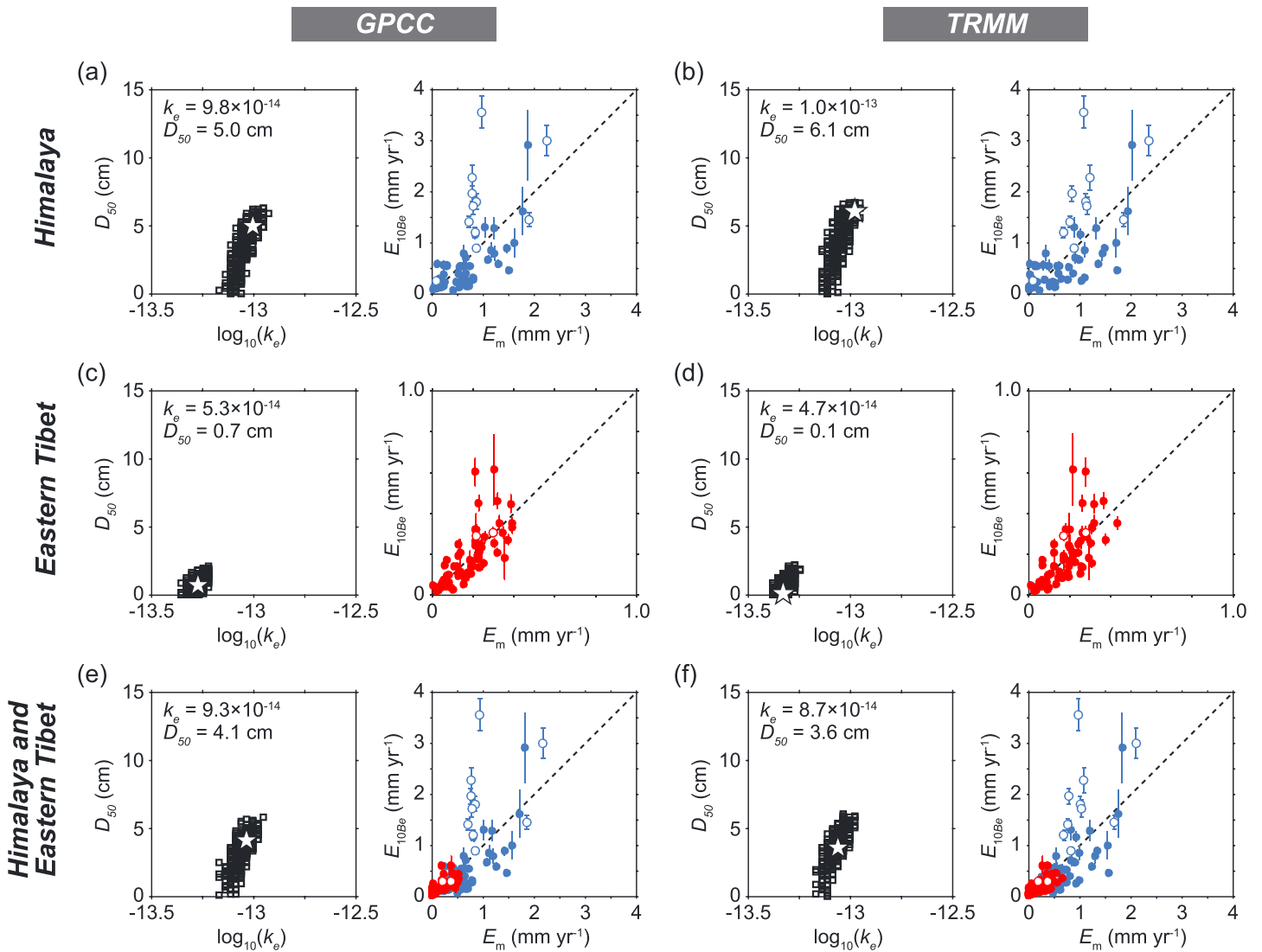
Figure 10. Comparison of best fit results from stochastic-threshold stream power model in the (a and b) Himalaya, (c and d) Eastern Tibet, and (e and f) both regions together. The columns correspond to different gridded precipitation data sets from the Global Precipitation Climatology Center (GPCC) and the Tropical Rainfall Measuring Mission (TRMM; see text for details). For each region and precipitation data set, two panels are shown. The left plot gives the best fit combinations of erosional efficiency, k_e, and median grain size, D_{50}, from each of the 500 Monte Carlo runs (squares) and the best fit parameter combination of all runs (star). The right plot shows the modeled and ^{10}Be-derived erosion rates for the best fit parameter combination of all runs and for all catchments. The dashed line gives 1:1 relationship. The filled and open marker symbols denote catchments with no and 1–20% present-day ice cover, respectively.

In the Himalaya, the ensemble best fit D_{50} values vary between ~5 and 6 cm, a value consistent with D_{50} grain sizes of ~6–10 cm and ~4.5–7 cm from the Nepalese Marsyandi River [*Attal and Lavé*, 2006] and the Kali Gandaki and Narayani rivers [*Mezaki and Yabiku*, 1984], respectively. In Eastern Tibet the ensemble best fit D_{50} values are lower than 1 cm, which implies that no threshold is needed to explain these data. The corresponding value of k_e is ~50% lower than for the Himalaya, which would imply more resistant bedrock. *Godard et al.* [2010] reported D_{50} values from several rivers in the Longmen Shan that are ~7–10 cm, suggesting our best fit grain sizes are unreasonably low. Additionally, it might be expected that the lower value of k_e (i.e., lower erodibility) for Eastern Tibet would be reflected in coarser, rather than finer-grained channel-bed sediment.

When applying the stochastic-threshold SPM to the two data sets simultaneously, the best fit k_e and D_{50} are closer to the best fit parameter combination from the Himalaya alone (Figures 10e and 10f). Although

Table 5. Best Fit Model Results

Model Run	Misfit, $\varphi((m\ s^{-1})^2)$	Grain Size Factor, k_{50} $(10^{-3}\ m^{0.64})^c$	Median Grain Size[d], D_{50} (cm)	Threshold Shear Stress[d], τ_c (kg m^{-1} s^{-2})	Incision Efficiency Factor, k_e (m$^{2.5}$ s^2 kg^{-1})
Area-based simple stream power model[a]	42.7	–	–	–	–
Runoff-based simple stream power model[b]	39.8	–	–	–	–
*Constant D_{50}, constant τ_c**					
Himalaya, GPCC	21.6	–	5.0	37.5	9.8×10^{-14}
Himalaya, TRMM	19.8	–	6.1	45.8	1.0×10^{-13}
Eastern Tibet, GPCC	0.6	–	0.7	5.3	5.3×10^{-14}
Eastern Tibet, TRMM	0.6	–	0.1	0.8	4.7×10^{-14}
Himalaya and Eastern Tibet, GPCC	22.5	–	4.1	30.8	9.3×10^{-14}
Himalaya and Eastern Tibet, TRMM	21.3	–	3.6	27.0	8.7×10^{-14}
*Constant D_{50}, variable τ_c**					
Himalaya and Eastern Tibet, GPCC	23.0	–	2.4	23.9–33.8	9.3×10^{-14}
Himalaya and Eastern Tibet, TRMM	21.6	–	2.9	28.9–40.8	9.3×10^{-14}
*Variable D_{50}, constant τ_c**					
Himalaya and Eastern Tibet, GPCC	24.2	4.4	2.7–4.8	20.8–36.3	9.3×10^{-14}
Himalaya and Eastern Tibet, TRMM	22.7	4.9	2.7–4.8	23.2–40.4	8.7×10^{-14}
*Variable D_{50}, variable τ_c**					
Himalaya and Eastern Tibet, GPCC	23.8	2.7	1.7–3.0	17.0–41.8	9.3×10^{-14}
Himalaya and Eastern Tibet, TRMM	22.5	2.7	1.7–3.0	17.0–41.8	8.7×10^{-14}

[a]Based on $E = Kk_s^n$. See sections 1 and 2 for details.
[b]Based on $E = Kk_s^n \bar{R}^{0.5}$. See section 3.2 for details.
[c]The unit of k_{50} is derived from equation (17), with an exponent $q = 0.4$.
[d]In case of variable D_{50} or τ_c^*, the range of given values refers to k_{sn} values between 100 and 400 m$^{0.9}$.

the misfit between modeled and ^{10}Be-derived erosion rates is almost identical to the case of the Himalayan data alone, the model systematically predicts too high erosion rates at low k_{sn} values in Eastern Tibet, but as the associated deviations are small they do not affect the misfit value by much. This circumstance is directly related to the relatively high threshold, which suppresses erosion at low k_{sn} values and highlights the influence of a constant incision threshold when fitting the data in Eastern Tibet.

5.5.2. Constant Incision Threshold Cases: Controls on Magnitude and Frequency of Erosive Discharges
To illustrate the principal features of the calibrated stochastic-threshold SPM with constant thresholds and present the results in an accessible way, we show in Figure 11 the ^{10}Be-derived erosion rates together with
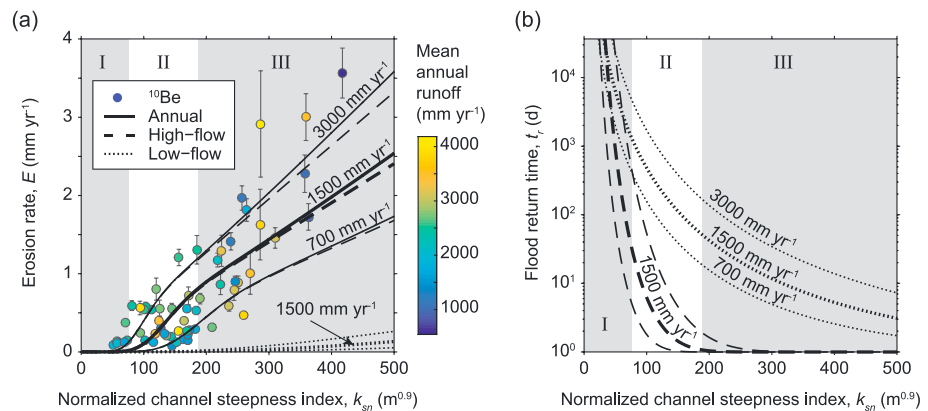
Figure 11. Best fit model results based on 700, 1500, and 3000 mm yr^{-1} mean annual runoff in the Himalaya. (a) Erosion rate-channel steepness relationships based on ^{10}Be-samples and the stochastic-threshold SPM. The solid black lines show total erosion rates, whereas the dashed and dotted lines show erosion rates during high- and low-flow regimes, respectively. The color-coding denotes mean annual runoff based on calibrated TRMM data. (b) Flood return times (in days) of erosive discharges during the high- and low-flow regimes. The background color in each panel indicates boundaries of regimes I-III that correspond to 1500 mm yr^{-1} mean annual runoff, indicated by the thick solid black line in Figure 11a and the thick dashed black line in Figure 11b.
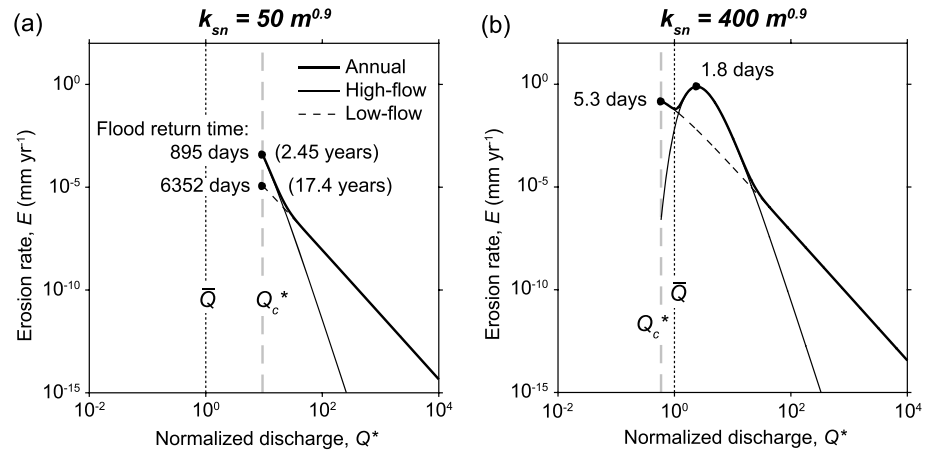
Figure 12. Stochastic-threshold stream power model-derived erosion rate as a function of normalized discharge, calibrated to the Himalaya (see Figure 10b). (a) Model results for $k_{sn} = 50$ m$^{0.9}$. (b) Same as Figure 12a but for $k_{sn} = 400$ m$^{0.9}$. Model results are based on 1500 mm yr^{-1} mean annual runoff, calibrated to the TRMM data. The black dots indicate peaks in low- and high-flow erosion rates and numbers give return times of corresponding discharge events. $\overline{Q}$ indicates the mean annual discharge, and Q_c^* indicates the normalized critical discharge.

model results from the Himalaya, where the back-calculated threshold values are consistent with observations of channel-bed sediment grain size. Model results are shown for mean annual runoff ($\overline{R}$) values of 700, 1500, and 3000 mm yr^{-1}, but in the following, we focus on the case of $\overline{R}$=1500 mm yr^{-1} (mean value for the Himalayan catchments with gauging data; Figure 6a). Three different regimes can be distinguished (Figure 11) [cf., *Lague et al.*, 2005; *DiBiase and Whipple*, 2011]: in the first regime (I), channel slopes are low ($k_{sn} < \sim$70) and return times of flows that surpass the threshold shear stress (τ_c) are >30 days during the high-flow regime and >1500 days during the low-flow regime. In the second regime (II), erosion rates increase nonlinearly with k_{sn}, but nearly all of the incision is achieved during the high-flow regime. In this regime, the return time of erosive high-flow discharge events decreases from ~30 days at $k_{sn} = 70$ m$^{0.9}$ to 1 day at $k_{sn} = 200$ m$^{0.9}$, whereas the return time of erosive low-flow discharge events decreases from ~1500 days to 50 days over the same k_{sn} range (Figure 11). In the third regime (III), the shear stress threshold is small relative to bed shear stresses during the high-flow discharge and the k_{sn}-E relationship is equal to the case without any thresholds [cf., *Lague et al.*, 2005; *DiBiase and Whipple*, 2011]. Channels are steep enough so that erosive discharge events occur frequently even during low-flow discharges, with return times between ~50 days at $k_{sn} = 200$ m$^{0.9}$ and ~5 days at $k_{sn} > 400$ m$^{0.9}$. The relative contribution of low-flow discharge events to the total erosion is <10%.

Figure 12 shows the relative contribution of discharge events of different magnitude to the total erosion rate, as derived from the stochastic-threshold SPM calibrated to the Himalaya, and for mean annual runoff ($\overline{R}$) of 1500 mm yr^{-1}. Threshold effects dominate gentle-sloping channels ($k_{sn} = 50$ m$^{0.9}$), and the critical normalized discharge, Q_c^* is well above the mean annual discharge, $\overline{Q}$, resulting in return times of the most erosive flows of 2.45 and 17.4 years in the high- and low-flow regime, respectively. All geomorphic effective discharges are within the power law domain of the discharge pdf, and most of the incision is achieved by events just able to exceed the threshold shear stress. In steep catchments ($k_{sn} = 400$ m$^{0.9}$) however, Q_c^* is lower than $\overline{Q}$, with return times <6 days. Whereas the distribution of erosion rates during low-flow discharges is characterized by a power law, the distribution has a peak in the case of high-flow discharges. Those events responsible for the bulk of the geomorphic work have discharges higher than $\overline{Q}$, and return times <2 days. It is interesting to note that for $Q < \sim\overline{Q}$ and $Q > \sim20\overline{Q}$, the low-flow regime contributes relatively more to erosion compared to the high-flow regime, simply because discharge events of that magnitude occur more often than in the high-flow regime. However, although the discharge distribution suggests that such events are more frequent during the low-flow regime, their rare occurrence in an absolute sense diminishes the role of these events for the geomorphic work they do. In summary, discharge events that are responsible for the bulk of the geomorphic work are either close to the mean annual discharge or, if $Q_c^* > \overline{Q}$, just able to exceed the threshold shear stress.

5.5.3. Variable Incision Thresholds

The above results show that assuming a constant incision threshold can produce reasonable fits within the Himalaya data set, but when combining the Himalaya and Eastern Tibet data together, we observe systematic mismatches between modeled and ^{10}Be-derived erosion rates for low k_{sn} values. Similar problems of the stochastic-threshold SPM to fit ^{10}Be-derived erosion rates at low k_{sn} values have been observed in the San Gabriel Mountains [*DiBiase and Whipple*, 2011]. One potential solution to this issue is to consider that, as argued in section 5.3, the erosion threshold may vary, either because of a dependence on channel slope or due to erosion rate-dependent grain sizes. We thus calibrated the stochastic-threshold SPM to the ^{10}Be-derived erosion rates from both regions assuming spatially variable incision threshold. The results are shown in Figure 13, together with model predictions from the simple drainage area-based SPM of equation (1), a discharge-based SPM [e.g., *D'Arcy and Whittaker*, 2014], and the best fit solution of the stochastic-threshold SPM with a constant incision threshold. Note that model results in Figures 13b–13f are based on the calibrated TRMM data as our source of mean annual runoff (model results using the GPCC data are similar and shown in Figure S10).

Our way of including variable incision thresholds are for both of the tested cases based on a formulation in which k_{sn} is the independent variable. While the relationship between τ_c^* and channel slope (equation (16)) is fixed, the relationship between D_{50} and k_{sn} is not predefined. Based on model runs with a range of values, we chose for the exponent q in equation (17) the value 0.4 that yielded reasonable results and optimized the factor k_{50}. The best fit values of k_{50} and grain size range that corresponds to $100 \leq k_{sn} \leq 400$ are shown in Table 5. As a general result, we observe that compared to the stochastic-threshold SPM with constant τ_c^* and D_{50}, spatially variable thresholds help in better fitting the low-k_{sn} data from Eastern Tibet. In the Himalaya however, predicted erosion rates appear systematically too high at low ^{10}Be-derived erosion rates. As a result, the combined misfit between ^{10}Be-derived and modeled erosion rates does not change by much. This overprediction at low erosion rates is more strongly developed in the case of variable D_{50} compared to variable τ_c^* and is most pronounced if both τ_c^* and D_{50} vary (Table 5). Overall, the introduction of variable thresholds does not strongly affect the high-k_{sn} data, as shown, for example, in Figure 14 for 1500 mm yr^{-1} mean annual runoff and using the best fit parameters from the models shown in Figures 13c–13e and Table 5.

5.5.4. Summary of Data-Model Comparison

Our effort to reconcile the ^{10}Be-derived erosion rates from the two regions was only partly successful. Although calibrating the stochastic-threshold SPM to each data set yielded reasonable fits between ^{10}Be-derived and modeled erosion rates, the obtained threshold in Eastern Tibet is associated with unreasonably small grain sizes. Thus, modeling the data from the two regions simultaneously produced poor fits for the lowest erosion rate samples, which are the most sensitive to threshold effects [*DiBiase and Whipple*, 2011]. We also observed an apparently systematic bias between ^{10}Be-derived and modeled erosion rates at high erosion rates in the Himalaya. Unfortunately, the number of data points from steep and rapidly eroding areas in the Himalaya is rather limited and most of the existing samples from these areas stem from catchments that were or still are partly ice covered. Although we deem it rather unlikely that subglacial-derived sediments could account for the apparent bias, there remains the possibility that it is due to other sample issues. We discuss a variety of potential reasons for the apparent bias and also for the remaining scattered mismatches between ^{10}Be-derived and modeled erosion rates in section 6.1. To get a better sense of how sensitive the model results are to variations in some of the less well-constrained input parameters, we carried out sensitivity tests that we present in the following section.

5.6. Sensitivity of the Model Results to Variations of the Input Parameters

Some of the parameters that we used for our modeling are not well constrained, whereas others are subject to change over time. It is thus useful to test how sensitive the model results are to variations in these parameters. In Figure 15 we show how variations in different parameters of the stochastic-threshold SPM (by −50%, −25%, 0%, +25%, and +50%) affect the k_{sn}-E relationship that we established for the Himalaya, assuming 1500 mm yr^{-1} mean annual runoff. For comparison, we show the ^{10}Be-derived erosion rates in the background but emphasize that their variability partly reflects differences in mean annual runoff. Note also that the absolute value of mean annual runoff has no effect on the direction and relative magnitude of changes in modeled erosion rates.
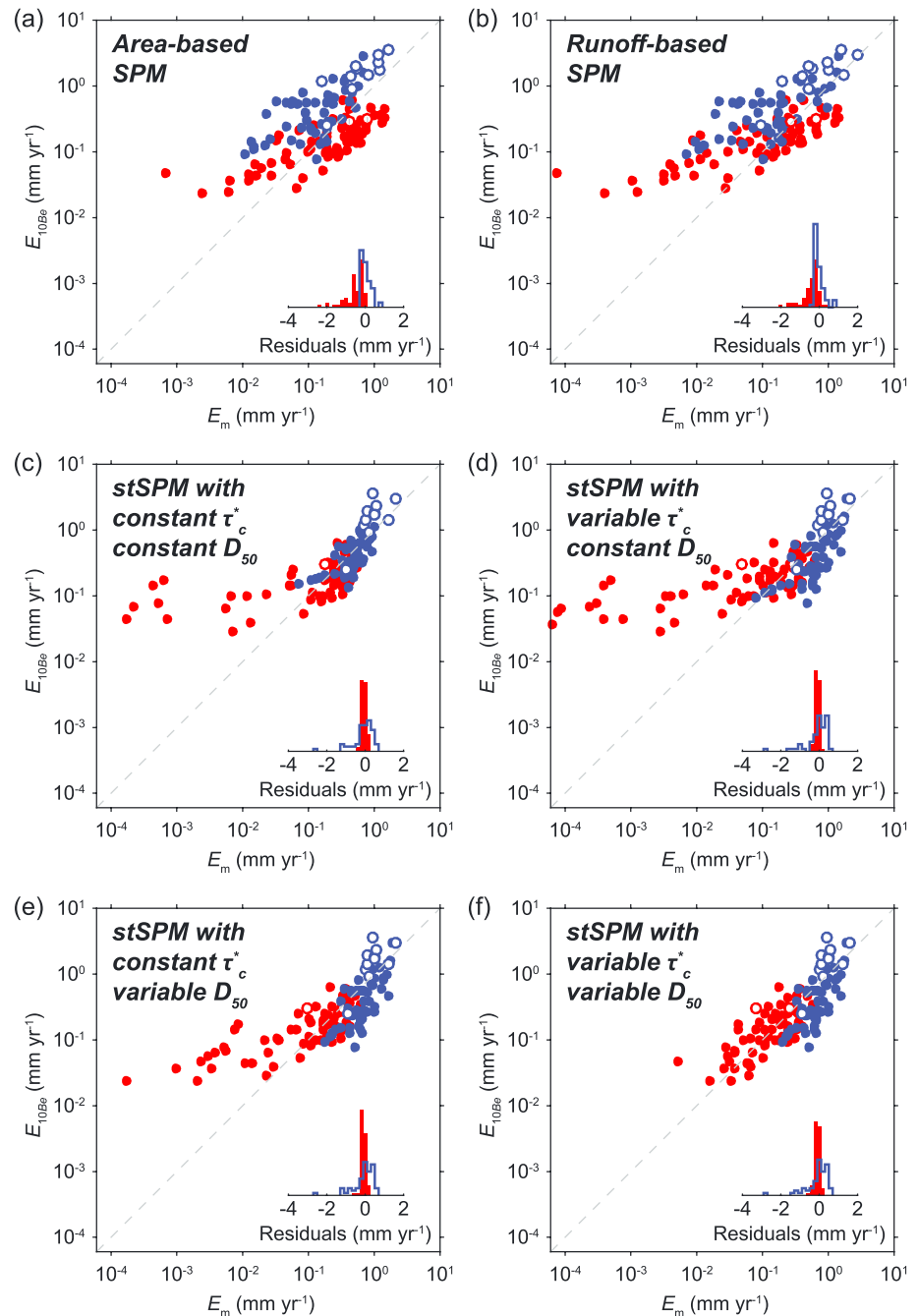
Figure 13. Best fit erosion rate model results for the combined data set from the Himalaya (blue points) and eastern Tibet (red points). The filled and open marker symbols denote catchments with no and 1–20% present-day ice cover, respectively. (a) Simple drainage area-based stream power model (SPM) following equation (1). (b) Runoff-based SPM obtained from TRMM-derived catchment-average mean annual precipitation. (c) Stochastic-threshold stream power model (stSPM) with a constant Shields number, τ_c^*, and constant median grain size, D_{50}. (d) Stochastic-threshold SPM with variable τ_c^* and constant D_{50}. (e) Stochastic-threshold SPM with constant τ_c^* and variable D_{50}. (f) stochastic-threshold SPM with variable τ_c^* and variable D_{50}.

We first assessed the potential impact of precipitation changes on rates of river incision, by varying parameters that relate to the discharge distribution as defined by equation (14). The largest changes in the k_{sn}-E relationship arise from varying the normalized mean high-flow discharge, Q_h^* (Figure 15a). Varying Q_h^* by up to ±50% induces changes in erosion rates that are significantly larger. In contrast, varying the
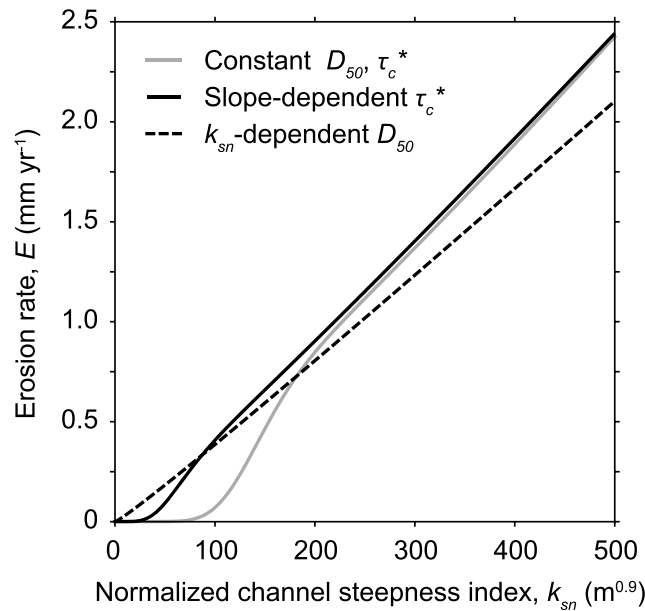
Figure 14. Relationship between channel steepness index, k_{sn}, and erosion rate established for the TRMM-calibrated Himalaya and Eastern Tibet data, assuming 1500 mm yr^{-1} mean annual runoff. For parameter values see Table 5.

normalized mean low-flow discharge, Q_l^*, (Figure 15b) by the same relative amounts has only minor effect on erosional efficiency. The impact of changes in the annual partitioning into high- and low-flow regimes (through the high-flow fraction f) lies in between changes in Q_l^* and Q_h^* (Figure 15c). Changes in both the high-flow and low-flow discharge variability (k_h, k_l) have almost no effect on the k_{sn}-E relationship (Figure 15d). This stems from the fact that the high-flow variability is small (high k_h values), while the mean high-flow discharge is high enough for threshold effects to be unimportant. Only at k_{sn} values between ~130 m$^{0.9}$ and ~250 m$^{0.9}$ would increasing discharge variability (smaller k_h values) result in decreasing erosion rates, because some of the high-flow discharge events would not surpass the threshold anymore. The effect reverses for lower k_{sn} values ($<$130 m$^{0.9}$), where now some of the discharge events are high enough to surpass the threshold so that erosion rates increase. Erosion during the low-flow regime is so low that changes in the low-flow discharge variability, k_l, have no discernible effect (not shown in Figure 15).

Because there is a lot of scatter in the width versus discharge plot, we next assessed the sensitivity of the k_{sn}-E relationship to different choices of k_{wn}. Reducing k_{wn} by 50% results in an $>$100% increase in erosional efficiency, whereas a 50% increase in k_{wn} reduces erosional efficiency by ~35% (Figure 15e). Finally, we tested the impact of variations in the flow resistance coefficient, k_t, which could stem from variations in grain size and thus bed roughness [*Ferguson*, 2007]. Again, variations by up to ±50% result in considerable changes in erosional efficiency by $> \pm$ 50% (Figure 15f).

6. Discussion

6.1. Comparability of Cosmogenic Nuclide-Derived Erosion Rates With Modeled River Incision Rates

A fundamental premise of our study is the comparability of cosmogenic nuclide-derived erosion rates with modeled river incision rates. Although previous studies have demonstrated good correlations between channel steepness indices, k_{sn}, and ^{10}Be-derived catchment-average erosion rates in different landscapes [*Safran et al.*, 2005; *Ouimet et al.*, 2009; *DiBiase et al.*, 2010; *Cyr et al.*, 2010; *Scherler et al.*, 2014a; *Mandal et al.*, 2015], there are several complicating factors that arise when comparing such data [*Lague*, 2014]. First, it is important to note that k_{sn} is a geometric property of river channels presumed to determine their incision rate, whereas cosmogenic nuclide concentrations in river sediments reflect hillslope erosion rates. In topographic steady state, this distinction is not an issue, as rivers set the base level for the adjacent hillslopes and the entire catchment erodes uniformly. In reality, however, hillslope and channel erosion might differ temporarily, as steady state is probably valid only when considering averages over a certain period of time. Large earthquakes, for example, have the potential to rapidly mobilize large amounts of hillslope material that may temporarily exceed river transport capacity and bias the cosmogenic nuclide signature of river sediment [e.g., *West et al.*, 2014]. While this effect leads to overestimating erosion rates, there is also a chance to underestimate erosion rates in rapidly eroding landscapes. If large landslides account for a significant portion of
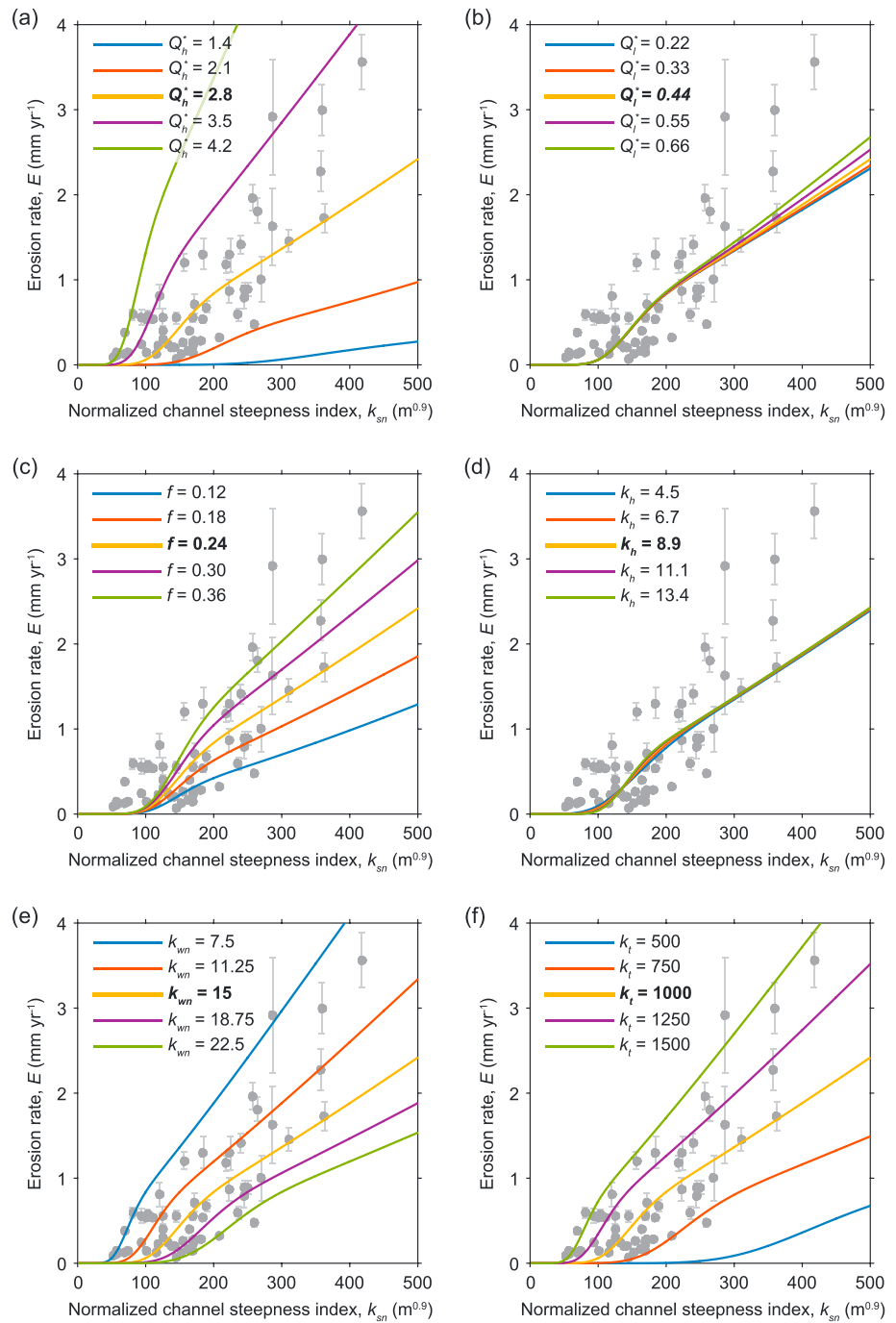
Figure 15. Sensitivity of the k_{sn}-erosion rate relationship calibrated to [10]Be-derived erosion rates from the Himalaya (see Figure 10b) to (a) the normalized high-flow regime, Q_h^*, (b) the normalized low-flow regime, Q_l^*, (c) the annual fraction of the high-flow regime, f, (d) the discharge variability of the high-flow regime, k_h, (e) the normalized channel width index, k_{wn}, with units of m$^{-0.65}$ s$^{0.55}$, and (f) the flow resistance coefficient, k_t, with units of kg m$^{-7/3}$ s$^{-4/3}$.

landscape-scale erosion, cosmogenic nuclides tend to systematically underestimate erosion rates [*Niemi et al.*, 2005; *Yanites et al.*, 2009].

Another difficulty is that the two metrics have different integration timescales [e.g., *Kirchner et al.*, 2001; *Orem and Pelletier*, 2016]. The channel steepness index, k_{sn}, is a geometric characteristic of the present drainage thought to reflect a catchment's response to tectonic and climatic forcing [*Kirby and Whipple*, 2012]. Provided a relatively small catchment with homogeneous rock types and climate, observed spatial variability in k_{sn} values

Table 6. Environmental Factors and Their Potential to Explain the Scatter and Bias at High Erosion Rates Between [10]Be-Derived and Modeled Erosion Rates

Environmental Factor	Potential Explanation for	
	Scatter	Bias at High Erosion Rates
Precipitation in the Long Term		
Different magnitudes	no	no
Different variability	no	no
Vegetation Cover		
Reduced mean discharge	no	no
Reduced peak discharges	no	no
Rock Strength		
Unaccounted differences	yes	perhaps
Landslides		
Recent events	yes	no
Infrequent large events	no	perhaps
River Sediment		
Tools and cover effects	yes	perhaps
Grain size effects	yes	yes
Channel Width		
Unaccounted differences	yes	perhaps
Glaciation		
Subglacial sediments	no	perhaps
Landscape disequilibrium	no	yes

could be due to transient adjustments of the channel geometry to changes in climate or tectonics [e.g., *Whipple*, 2004; *Wobus et al.*, 2006]. The timescale of adjustment depends on the drainage area and the magnitude of erosion rates and can be on the order of 10^6 years [e.g., *Schildgen et al.*, 2012; *Scherler et al.*, 2014a]. Hence, true steady state topography may rarely be achieved. Cosmogenic nuclides, on the other hand, integrate catchment average erosion rates over time periods that scale with the erosion rate. In bedrock with a density of ~2.7 g cm^{-3}, integration times are ~600 years for erosion rates of 1 mm yr^{-1} and ~6000 years for erosion rates of 0.1 mm yr^{-1} [e.g., *von Blanckenburg*, 2005], which is considerably shorter than the time needed for topographic adjustments. Therefore, if orbital-driven climatic variations affect hillslope erosion rates through increased landsliding [*Bookhagen et al.*, 2005], for example, this could be expressed in cosmogenic nuclide-derived erosion rates [e.g., *Schaller and Ehlers*, 2006], but not equally in channel steepness. In addition, it has been recently suggested [*Scherler et al.*, 2015] that in threshold landscapes like the Himalaya, where landsliding is an important erosion mechanism [*Burbank et al.*, 1996], transient periods of river aggradation and rising base levels could reduce landslide frequency and thus hillslope erosion rates, but the effects on k_{sn} would be minor. Finally, because integration times depend on erosion rates themselves, shorter climatic changes may affect cosmogenic-nuclide-derived erosion rates in steep landscapes but not those in gentle landscapes, creating disparities among catchments that erode at different rates.

The uncertainties related to these factors are difficult to quantify but can probably be substantially larger than the analytical uncertainties. Therefore, k_{sn}-erosion rate relationships based on cosmogenic nuclides are likely inherently noisy, especially at higher erosion rates and k_{sn} values. In more slowly eroding landscapes, both [10]Be-derived erosion rates and k_{sn} values are more resilient to transients in climate and tectonics, but differences in erosional efficiency are also much harder to detect [*Kirby and Whipple*, 2012]. The data from Eastern Tibet support this notion, as the scatter in erosion rates is low for k_{sn} values $<$~200 m$^{0.9}$ but higher for k_{sn} values $>$ ~200 m$^{0.9}$ (Figure 2). In the Himalaya, however, scatter in erosion rates is generally high, irrespective of k_{sn} values. At present, we are unable to explain these differences.

6.2. Role of Climate and Other Factors in Explaining Differences in Erosional Efficiency Between the Himalaya and Eastern Tibet

Our modeling results show some success in collapsing the [10]Be-derived erosion rates from the Himalaya and Eastern Tibet onto one trend when accounting for spatial variations in discharge mean and variability and channel widths with the stochastic-threshold SPM. Compared to the simple SPM, even when accounting for spatial variations in mean annual runoff, the stochastic-threshold SPM produces better fits to the data (Table 5). The sensitivity tests have shown, however, that regional differences in discharge variability have almost no effect, whereas most changes in erosional efficiency arise from regional differences in channel widths and mean discharge during the high-flow season, rendering threshold effects relatively unimportant. In addition, there exist residual, possibly systematic deviations between [10]Be-derived and modeled rates at the higher end of erosion rates in the Himalaya (modeled rates lower), and the scatter of the data around the 1:1 line is substantial. In the following, we will discuss some possible factors that may explain these shortcomings (Table 6).

6.2.1. Precipitation

It is possible that our way of accounting for spatial gradients in precipitation and thus discharge could be inappropriate if the present-day precipitation rates that we used in our modeling were not representative for the timescales relevant for ^{10}Be-derived erosion rates or channel steepness. It is well known that the early Holocene has been a wetter period throughout monsoonal Asia [e.g., *Wang et al.*, 2008; *Herzschuh*, 2006], which implies that samples from slowly eroding areas ($<$0.1 mm yr^{-1}) integrate erosion rates over time periods that were on average wetter than samples from more rapidly eroding areas. The historical gauging data and modern satellite observations that we use instead integrate over much shorter time periods that may additionally be affected by ongoing climate change. Because the stochastic-threshold SPM is very sensitive to changes in Q_h^* and f (Figure 15), these different integration time periods could be important. While this could potentially be an important issue in some areas, we do not think that it helps to explain the remaining scatter between ^{10}Be-derived and modeled erosion rates nor the deviations at high erosion rates, which typically integrate over time periods that do not extend into the early Holocene. Although little is known about past changes in the variability of precipitation and thus discharge (k_l and k_h), our sensitivity analysis has shown that such changes would not affect erosion rates by much (see Figure 15 and section 5.6).

6.2.2. Vegetation Cover

Another indirect aspect of climate that imparts on discharge magnitudes and variability are soils and vegetation [e.g., *Langbein and Schumm*, 1958; *Istanbulluoglu and Bras*, 2005]. Where soils and vegetation are present, evapotranspiration is higher, and the amount of runoff for a given precipitation event is lower [e.g., *Rossi et al.*, 2015]. Furthermore, interception by plants and infiltration into soils with subsequent subsurface runoff will act to retard the flow of water from hillslopes to rivers and consequently reduce peak discharge magnitudes. While such effects are likely to be important when comparing catchments from arid and humid environments [e.g., *Acosta et al.*, 2015], or from slowly and rapidly eroding areas that may have contrasting soil cover [e.g., *DiBiase et al.*, 2012], we do not think they are particularly relevant in our study area where we compare catchments from rather humid and rapidly eroding areas. Furthermore, while soils and vegetation influence the transformation of precipitation to discharge, this should not affect our results as we calibrated the precipitation data sets we used to available discharge records. Recently, it has been hypothesized that both scatter and nonlinearity in k_{sn}-E relationships, which are based on ^{10}Be-data from the Himalaya, are related to differences in vegetation cover, with less rainfall and vegetation resulting in more erosional variability and a more nonlinear k_{sn}-E relationship [*Olen et al.*, 2016]. However, our modeling results show that even large changes in discharge variability have almost no influence on the k_{sn}-erosion rate relationship in the Himalaya (Figure 15d).

6.2.3. Rock Strength

One of our starting observations was that the variability in lithology and rock type within the two regions is likely higher than between the regions and therefore unlikely to explain the regional differences in erosional efficiency. While this is still true, it does not mean that rock strength or erodibility have to follow the same spatial variability. Previous studies highlighted the role of joint spacing in setting rock strength and erodibility in both fluvial [*Whipple et al.*, 2000b] and glacial settings [*Dühnforth et al.*, 2010]. Similarly, in a recent study from Eastern Tibet, *Gallen et al.* [2015] analyzed coseismic landslides resulting from the Wenshuan earthquake and found that effective cohesion is more strongly influenced by proximity to the mountain front, where the climate is wetter and fault density is higher, than by rock type. If rock strength, even for similar rock types, were different within and between the two regions, this may indeed explain some or much of the scatter we observe.

To offset the deviations at higher erosion rates in the Himalaya, rocks in more rapidly eroding catchments would have to be weaker, for example due to changes in tectonic setting [*Molnar et al.*, 2007] or systematic variations in regional tectonic and topographic stresses [e.g., *St. Clair et al.*, 2015]. Differences in rock strength that are associated to fracture density are difficult to quantify with traditional methods such as a Schmidt hammer [e.g., *Allen et al.*, 2013], and we are not aware of any study that quantified fracture densities in the Himalaya or Eastern Tibet. Although *Gallen et al.* [2015] proposed that rocks at the range front of Eastern Tibet are weaker, in part due to higher density of active faults, we do not think such an explanation holds for the deviation at high erosion rates in the Himalaya. Tectonically induced fractures are probably a more important factor for enhancing the erodibility of massive rocks, like granites, compared to layered metasedimentary rocks, which typically contain already abundant discontinuities in the form of bedding planes. In

both regions, however, massive crystalline rocks are more abundant in the rapidly eroding catchments, whereas more slowly eroding catchments often expose layered metasedimentary rocks (Figure 2).

If, on the other hand, geomorphic fracturing by thermal, chemical, and biotic processes is more important in setting rock strength [e.g., *Clarke and Burbank*, 2010], then rocks from more slowly eroding catchments might be expected to have higher fracture densities and be weaker. Frost-related fracturing of bedrock could also contribute to higher fracture densities at certain elevations [e.g., *Hales and Roering*, 2009]. Cooler temperatures during the last glacial period would have caused this zone to lie lower compared to today. For example, Quaternary frost cracking intensities in the Nepalese Khumbu Himalaya were estimated to be highest at elevations between 4 and 6 km [*Scherler*, 2014], thereby affecting many of the sample catchments. The impact of frost cracking in Eastern Tibet would probably be different, as catchments at such elevations are among the most slowly eroding catchments that presumably expose ample soil cover beneath which frost cracking processes are subdued [*Andersen et al.*, 2015].

6.2.4. Landslides

It is well known that bedrock landslides add additional uncertainty to ^{10}Be-derived erosion rates due to the stochastic input of low-concentration material [*Niemi et al.*, 2005; *Yanites et al.*, 2009; *West et al.*, 2014], and many data sets from rapidly eroding landscapes contain suspicious data "outliers" that authors typically suspect to be due to recent landsliding [e.g., *Ouimet et al.*, 2009; *Scherler et al.*, 2014a]. Landslides may thus potentially contribute to the remaining scatter in the data set analyzed in this study. Could there also be fundamental issues with the role of landsliding at high erosion rates? The recent Wenshuan earthquake has triggered >50,000 landslides, which are thought to at least balance the volume of rock uplift by the earthquake [*Li et al.*, 2014]. The recurrence interval for earthquakes of this magnitude is estimated to be on the order of several thousand years [e.g., *Shen et al.*, 2009; *Zhang et al.*, 2010], which can be longer than the integration timescale of ^{10}Be-derived erosion rates from the Longmen Shan. An intriguing possibility is that erosion rates in more rapidly eroding parts of Eastern Tibet are therefore systematically underestimated by ^{10}Be, due to infrequent but important large earthquakes, as suggested from comparison with million-year exhumation rates inferred from thermochronology [*Ouimet*, 2010]. The same could be true for ^{10}Be-derived erosion rates from the Himalaya, which typically integrate over even shorter timescales, due to the higher erosion rates, although the recurrence intervals of large earthquakes are also thought to be shorter [*Stevens and Avouac*, 2016]. At present, it is not entirely clear that landslide erosion from infrequent large earthquakes would dominate the long-term record, and it is difficult to evaluate the relative importance of this mechanism in each region. Although ^{10}Be-derived erosion rates and long-term exhumation rates from thermochronology appear to show some mismatches also in the Himalaya [cf., *Lupker et al.*, 2012; *Thiede and Ehlers*, 2013; *Scherler et al.*, 2014a; *Godard et al.*, 2014], direct comparison is hampered due to bias of ^{10}Be-derived erosion rates toward the ice-free and more slowly eroding Lesser Himalaya, whereas low-temperature thermochronology data are typically biased toward the more rapidly eroding High Himalaya, as the Lesser Himalayan rocks rarely yield suitable apatite grains [e.g., *Thiede and Ehlers*, 2013].

6.2.5. River Sediment

Another known control on bedrock river incision is the tools and cover role of bed load sediment [*Sklar and Dietrich*, 1998]: while rivers that lack sediment may have no tools to incise into bedrock, excessive sediment supply may cover the bed and inhibit incision. The threshold term in the stream power model used in this study accounts for the cover effect only in a very simplistic way and does not consider its dependency on hillslope sediment supply and bed load grain size distributions. Some models of bedrock river incision have been developed that include these effects [e.g., *Sklar and Dietrich*, 2004; *Lamb et al.*, 2008; *Lague*, 2010], but their implementation is difficult as they depend on parameters that cannot be estimated easily. It is well known that the grain size distribution of the sediment supplied by hillslopes to rivers depends on lithology, fracture density, and likely also the climate-influenced rate of weathering [*Sklar and Dietrich*, 2006; *Sklar et al.*, 2006; Sklar *et al.*, 2016]. Some of the aforementioned influences of climate, vegetation, lithology, and landslides are therefore likely linked to grain size effects in complex ways.

Our efforts to include spatially variable thresholds into the stochastic-threshold SPM have yielded better model fits to the data at the lower end of erosion rates, mostly in Eastern Tibet, but yielded worse fits at high erosion rates in the Himalaya (Figure 13). One explanation may be that we parameterized D_{50} using k_{sn} as the independent variable, whereas the degree of weathering and rock disintegration may be more related to hillslope residence times and thus erosion rates, which follow different trends with k_{sn}, depending on other

variables such as discharge. Therefore, a more mechanistic formulation taking into account how grain sizes may depend on weathering processes [*Riebe et al.*, 2015; *Attal et al.*, 2015; *Sklar et al.*, 2016] would be preferable and should be a target of future efforts. Because of the above mentioned multiple controls on river sediment size, it is certainly possible that some of the scatter in our results is due to spatially variable river sediment and threshold effects. In addition to spatial variations in grain size delivery to channel networks, changes in dominant incision process (e.g., abrasion, plucking, and debris flows) may influence the sensitivity to threshold effects and the scaling between incision rate and channel steepness in general [*Whipple et al.*, 2013]. River sediment size is also likely to influence the flow resistance coefficient k_t that has the capability to greatly affect erosional efficiency (Figure 15f), but which at present is unconstrained. Larger grain sizes likely result in greater bed roughness and thus higher flow resistance [*Ferguson*, 2007], which increases shear stress and erosional efficiency. Provided that faster erosion results in larger grain sizes [*Riebe et al.*, 2015; *Attal et al.*, 2015; *Sklar et al.*, 2016], this effect could explain the systematic deviation at higher erosion rates.

6.2.6. Channel Width

Our and previous measurements of channel width from different rivers in the Himalaya and Eastern Tibet [e.g., *Finnegan et al.*, 2005; *Craddock et al.*, 2007; *Kirby and Ouimet*, 2011; *Fisher et al.*, 2013; *Whipple et al.*, 2013] have shown that these tend to be quite variable and to follow different power law scaling, often with a lot of scatter. Our sensitivity analysis has shown that changes in k_{wn} can have a large impact on erosional efficiency and accounting for such variability could improve model predictions. Most of the catchments we used in our study are small enough so that spatial variations in climate or rock uplift are probably minor, and hence, variations in channel width ought to be either due to differences in rock erodibility, or due to transients in the channel geometry. Therefore, we think that some of the scatter we observe is probably related to such small-scale effects. However, it is difficult to account for them in the catchment-integrated approach we have chosen. Because of the variability in channel widths for individual rivers, it is also difficult to evaluate whether there exist any systematic variations in the channel width-discharge scaling relationship (equation (6)) as a function of incision rate [e.g., *Yanites et al.*, 2010; *Lague*, 2014], for example, due to a transition in the dominant incision processes.

6.2.7. Glaciation

Although subglacial sediments may bias cosmogenic nuclide-derived erosion rates at high elevations, it is unlikely that there is a systematic bias at high erosion rates in the Himalaya (section 5.5.1). However, even if a catchment is ice-free at present, past glaciations might still have an impact on how and where the catchment erodes today [e.g., *Norton et al.*, 2010]. After ice retreat, formerly glaciated catchments often have unstable, oversteepened rock slopes [e.g., *Ballantyne*, 2002] that tend to fail and transiently elevate erosion rates, even long after deglaciation [e.g., *Church and Ryder*, 1972; *Church and Slaymaker*, 1989; *Moon et al.*, 2011]. On the other hand, glaciers typically carve out gentle-sloping and sometimes overdeepened valleys [e.g., *Brocklehurst and Whipple*, 2002; *Scherler et al.*, 2014b], which provide accommodation space that may buffer the sediment flux from higher parts in the catchment. In this case, the sampled stream sediments could be biased toward source areas at lower elevations where production rates are lower than the catchment average, and the calculated erosion rates would thus be too high. For comparison, at 29°N, 95°E, surface production rates at 4 km elevation are >3 times those at 2 km elevation [http://hess.ess.washington.edu/math/al_be_v22/al_be_multiple_v22.php; *Balco et al.*, 2008]. Therefore, former glaciation may indeed result in ^{10}Be-derived erosion rates being either truly or artificially higher compared to long-term erosion rates.

Whereas residuals between modeled and ^{10}Be-derived erosion rates show no altitudinal dependence in Eastern Tibet, the largest residuals in the Himalaya are found in catchments at high elevations (Figure 16a), suggestive of former glacial sculpting. We note, however, that although absolute residuals are much larger at high elevations, relative residuals are substantial also at lower elevations (Figure 16b). Comparison of each catchment's concavity index, θ, with its mean elevation shows a negative trend with elevation: while catchments below 2000 m often have concavity indices equal or greater than our reference value of 0.45, catchments at higher mean elevations often have indices that are below this value (Figure 16c). It is remarkable that a similar trend with elevation appears to prevail in both regions; but as most catchments from Eastern Tibet are located at high elevations, they have on average lower concavity indices (Table S2). These lower concavity indices could reflect the effect of glacial sculpting, which lowers channel slopes in high parts of a catchment. In Eastern Tibet, they may also reflect a recent increase of incision rate [*Harkins et al.*, 2007], which steepens channel slopes in lower parts of a catchment, but this explanation does not systematically
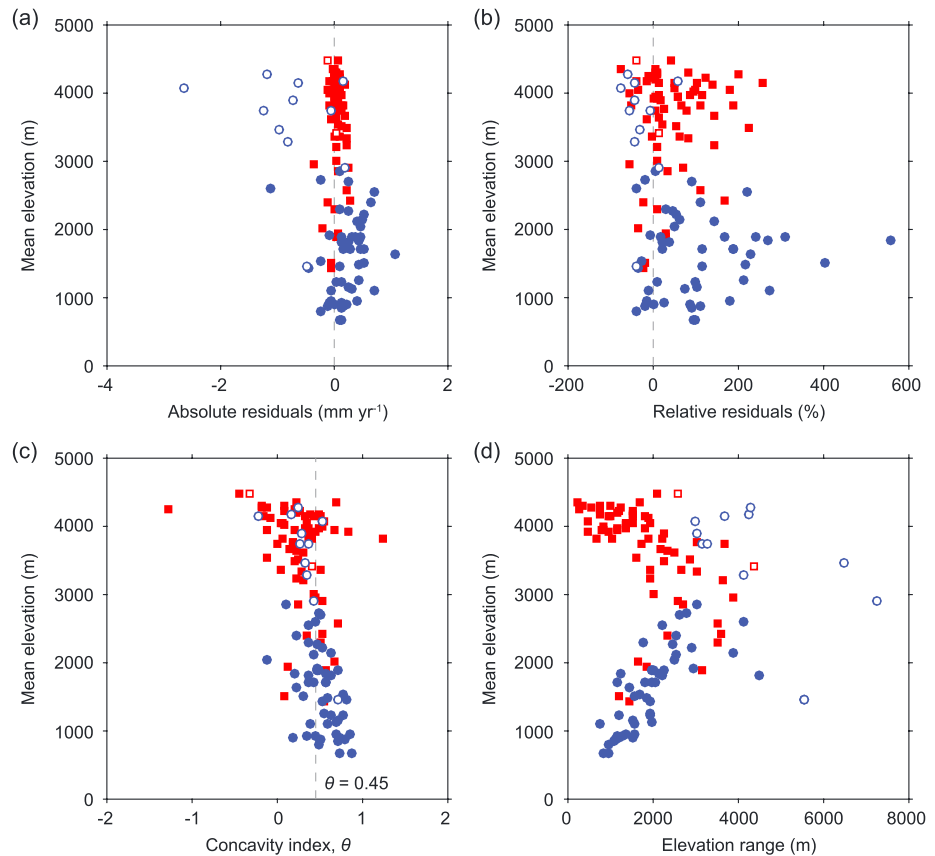
Figure 16. Comparison of catchment mean elevation with (a) absolute residuals, (b) relative residuals, (c) the concavity index, and (d) catchment elevation range. The red squares and blue circles indicate catchments from Eastern Tibet and the Himalaya, respectively. The hollow symbols indicate catchments with present-day ice cover ($0 <$ ice cover $< 20\%$). Model results are based on the TRMM-calibrated stochastic-threshold SPM with variable τ_c^* and variable D_{50} (see Figure 13f).

hold in the Himalaya. In any case, lower concavity values in the context of the stream power model suggest nonuniform erosion rates. Catchments at high mean elevation in Eastern Tibet do not show equally large residuals, because they occupy limited elevation ranges (Figure 16d), which efficiently buffer any production rate effects. In addition, they are less steep and erode much slower, which results in small absolute residuals. We therefore suggest that the lower concavity indices at higher mean elevations in the Himalaya are due to glacial sculpting, which could systematically bias [10]Be-derived erosion rate estimates due to catchment mean production rates that are assumed too high. However, limiting the entire data set to a narrow range of concavity values (e.g., 0.3–0.6) does not change the results significantly, as the residuals are uncorrelated with the concavity values (Figure 17).

6.2.8. Summary

Our choice of modeling framework was guided by the expected dominance of spatial variations in climate and how they would express themselves in river discharge and its variability. However, the above discussion has shown that there are many additional controls on bedrock river incision that are not well captured in the stochastic-threshold SPM that we used in this study. Specifically, the influence of rock strength and river sediment may be equally important as discharge magnitude and variability, and deserves to be better studied and quantified. While rock strength can be expected to be less variable through time, river sediment and erosion thresholds, if based on bed load grain sizes, can also be studied from terrace deposits. Furthermore, the processes acting at the higher end of channel steepness indices/erosion rates need to be better understood to assess where deviations between data and modeling results are due to data issues or incomplete erosion laws. For example, controls other than discharge on channel width [e.g., *Finnegan et al.*, 2007; *Yanites et al.*, 2010; *Lague*, 2014], and changes in erosion processes, are not captured by the stream power model. In addition, by comparing model results with [10]Be-derived erosion rates, it is also necessary to consider methodological assumptions and how these may be
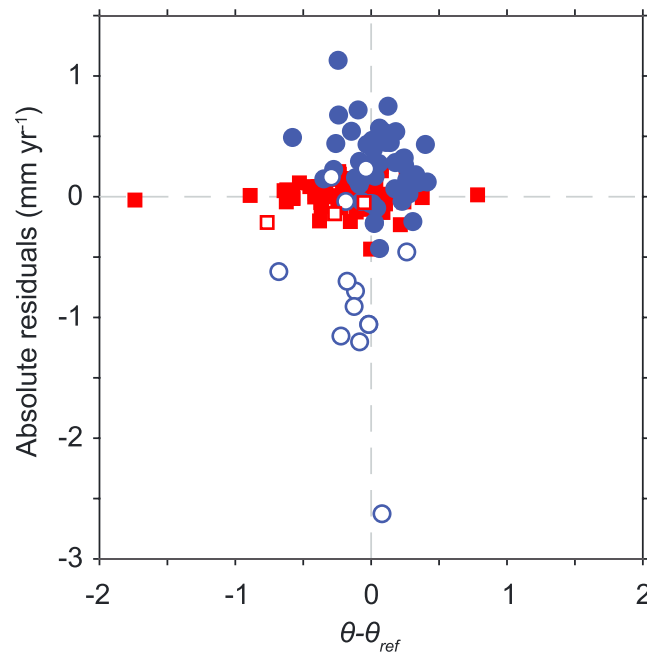
Figure 17. Absolute residuals between ^{10}Be-derived and modeled erosion rates versus difference between the measured concavity index, θ, and the reference concavity index, $\theta_{ref} = 0.45$. Model results are based on the TRMM-calibrated stochastic-threshold SPM with variable τ_c^* and variable D_{50} (see Figure 13f). The red squares and blue circles indicate catchments from Eastern Tibet and the Himalaya, respectively. The empty symbols indicate catchments with present-day ice cover ($0 < $ ice cover $< 20\%$).

violated in places where landslides and previous glaciation are important. Finally, although comparison of erosion rate estimates integrating over timescales that are long enough to capture erosional variability [e.g., *Ganti et al.*, 2016] with model results obtained from present-day climatic boundary conditions remains ambiguous, records of paleoclimate help us in evaluating potential biases.

6.3. Modeling Monsoonal Discharge Variability

Our analysis of daily discharge records from monsoonal Asia yielded a distinct pattern of discharge variability, which is typically expressed by a bimodal frequency distribution that corresponds to two discharge regimes (Figure 4). These two modes are temporally confined to the wet summer and dry winter seasons in the Himalaya (Figure 3a), but the pattern is more complicated farther to the east (Figures 3b–3d). In the Himalaya, low discharge variability within each regime (Figure 18) can be related to the different sources contributing to discharge during the monsoon seasons. During the winter monsoon season precipitation events are rare and stream discharge is mostly due to the release of groundwater [*Andermann et al.*, 2012] and snowmelt [*Wulf et al.,* 2015], i.e., processes with dampened variability compared to rainfall events. During the summer monsoon season precipitation occurs very regularly, often daily. Depending on the elevation range of the catchment, snow- and ice-melt can be substantial [*Immerzeel et al.*, 2010; *Bookhagen and Burbank*, 2010; *Wulf et al.*, 2015] and many rivers are constantly at high stage (Figure 3). Short-term variations in daily rainfall amounts have only a small impact on hydrographs, because of the delayed response due to subsurface flow and variable flow-path lengths.

Our modeling of the two discharge regimes using a weighted sum of two different inverse gamma distributions picks up well the variability associated to each regime. It should be noted, however, that for variability values of $k > 2$, the inverse gamma distribution has a light tail of high discharge events and is not substantially different from other parametric models that have light tails, such as an exponential distribution [*Lague*, 2014]. Nevertheless, by adding two different distributions, potential changes in each of these different modes or the partitioning between them can be treated in a straightforward manner. In our study, two distinct discharge regimes appear sufficient to fit the observational data, but we anticipate that there may exist regions in which more than two regimes prevail. The formulation shown in equation (14) can be easily expanded to account for additional regimes. However, it is clear that the smaller the contribution of any particular discharge regime to the total distribution, the longer the observational record needs to be for reliably picking it up with an unconstrained data fit.

Recently, *Rossi et al.* [2015] argued that the high discharge tail of discharge distributions in the United States and Puerto Rico is better captured with a stretched exponential distribution than with a power law, as previously used by *Molnar et al.* [2006]. In other regions, an inverse gamma distribution (Taiwan [*Lague et al.*, 2005]) or, as in our study, the weighted sum of two inverse gamma distributions, provide excellent fits to the observations. The choice of the parametric model of discharge distribution when used in conjunction
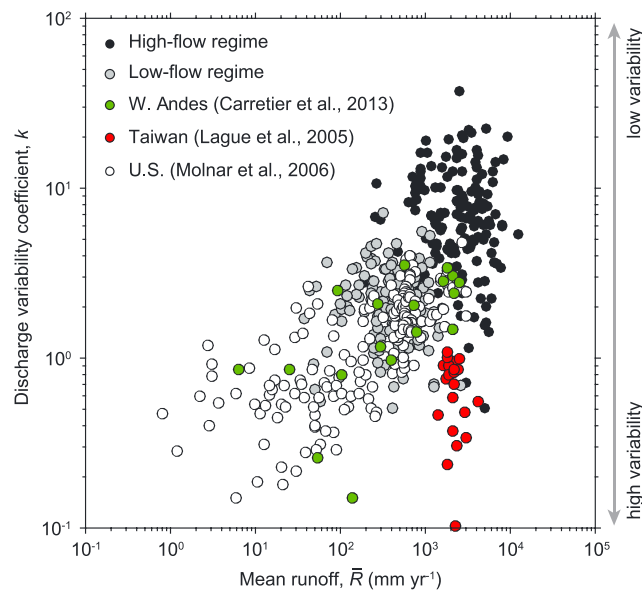
Figure 18. Discharge variability and mean annual runoff. Mean runoff in the high- and low-flow regimes has been scaled to a full year using the annual fraction, f and $(1-f)$, of each regime, respectively.

with a stochastic-threshold river incision model influences how long-term erosional efficiency varies as a function of channel steepness [*DiBiase and Whipple*, 2011]. However, the range of studies that examined discharge records from different regions [e.g., *Lague et al.*, 2005; *Molnar et al.*, 2006; *DiBiase and Whipple*, 2011; *Carretier et al.*, 2013; *Rossi et al.*, 2015; this study] has shown that there may not exist a single model suitable to capture all possible discharge distributions [*Lague*, 2014]. The bimodal distribution of daily discharges observed in Monsoonal Asia (e.g., Figure 4) is not well captured with any single distribution function and requires a weighted sum of two distribution functions (e.g., exponential, power law, inverse gamma, and stretched exponential). Our ability to accurately capture the very rare and high discharge events is probably less a question of the actual distribution used and more related to the amount of observational data available to constrain the model.

From an analysis of 440 stream gauge records from the United States, *Molnar et al.* [2006] concluded that discharge variability tends to decrease (higher k) as mean annual runoff increases (Figure 18). A similar pattern is observed for Chilean gauging records from the Western Andes of South America [*Carretier et al.*, 2013], although data from Taiwan, where both mean runoff and discharge variability are very high, contradict this trend, likely due to the impact of typhoons [*Lague et al.*, 2005]. When comparing the discharge variability from our study area with previous data (Figure 18), we find that our new observations, distinguished by season, broadly agree with the trend previously observed by *Molnar et al.* [2006]. Discharge variability of the low-flow regime clusters around k-values of 1–3 at mean annual runoffs between ~300 and 1000 mm yr^{-1} (scaled to the full year). These values are similar to those observed in the United States (Figure 18). Discharge variability of the high-flow regime covers scaled mean annual runoffs between ~1000 and 10,000 mm yr^{-1} and k-values that are between ~2 and 20, i.e., extremely low variability. It should also be stressed that discharge variability is likely higher in more arid parts of the Himalaya and Tibet, where we have no discharge data for and where infrequent excursions of north-penetrating monsoon moisture can result in highly erosive events [*Hobley et al.*, 2012].

6.4. Implications for Assessing the Geomorphic Impact of Climate Change

Assuming that spatial variations of erosion partly reflect a climatic control similar to how climate has impacted temporal variations of erosion, our stochastic-threshold model can be used to assess the impact of changes in precipitation and discharge on erosion. Our sensitivity analysis suggests that only changes in the duration and intensity of the summer monsoon can induce significant changes in bedrock river incision and, by extension, also sediment transport. Previous studies have argued that variations in monsoon strength have indeed had a pronounced impact on the spatial and temporal distribution of erosion in the Himalaya [e.g., *Goodbred and Kuehl*, 2000; *Galy and France-Lanord*, 2001; *Bookhagen et al.*, 2005; *Clift et al.*, 2008a, 2008b]. From marine and terrestrial records it is well known that the Asian monsoon intensity has strongly varied along with orbital-driven changes in solar insolation [e.g., *Clemens et al.*, 1991; *Wang et al.*, 2008]. Such intensity variations are associated with both changes in the amount of precipitation and changes in the extent of the monsoon realm. The most recent phase of an intensified monsoon was the early- to mid-Holocene [e.g., Gasse et al., 1991; *Herzschuh*, 2006]. During this period, it is thought that heavier precipitation, and thus discharge, resulted in more erosion in the Himalaya [*Clift et al.*, 2008b], which is also indicated by a

temporal clustering of large landslide events [*Bookhagen et al.*, 2005; *Dortch et al.*, 2009], and elevated sediment flux toward the Ganges-Brahmaputra River delta [*Goodbred and Kuehl*, 2000].

It is therefore interesting to investigate how monsoon strength affects erosion rates according to our model. Unfortunately, quantitative estimates of precipitation changes on orbital timescales are rare and largely based on climate model results. For example, *Li et al.* [2016] employed an atmospheric general circulation model to study climatic conditions over the Tibetan Plateau and bordering mountain ranges during the mid-Holocene (6 ka B.P.) and the Last Glacial Maximum (LGM; 21 ka B.P.). Their model results indicate that mid-Holocene precipitation was higher in the central Himalaya by up to 400–600 mm yr^{-1} compared to pre-industrial times, similar to the results by *Dallmeyer et al.* [2013]. This represents an increase of approximately 10–20%, depending on locality. According to our stochastic-threshold SPM that we calibrated to the Himalayan data, such an increase would translate to Q_h^* values of 3.1–3.4, which result in 35–80% higher river incision rates. In contrast, during the LGM, modeled summer monsoon precipitation was found to be lower by 600–1200 mm yr^{-1}, compared to preindustrial times, which results in Q_h^* values of 2.0–2.4 and thus a 60 to 70% reduction of river incision rates. This calculation assumes that the impact of topographic changes on hydrology can be neglected. It should further be noted that the calculation applies to rates of bedrock river incision and does not take into account transient changes in the amount of sediment supply from hillslopes. Paleo-erosion rates that were obtained with ^{10}Be from terrace deposits in the Yamuna catchment, Garhwal Himalaya, for example, indicate that hillslope erosion rates were in fact higher by a factor of 2–4 during a period of river aggradation in the Late Pleistocene, when bedrock incision was shut off [*Scherler et al.*, 2015].

6.5. Implications for Landscape Evolution

An important implication from the stochastic-threshold incision model is that the return time of the most effective floods [*Wolman and Miller*, 1960] varies considerably depending on the discharge sensitivity of the incision model (γ in equation (9)) and the discharge variability parameter, k [*Lague et al.*, 2005]. For the case of the Himalaya, we have shown that the return time of the most effective flood is a strong function of channel steepness (Figure 11). While in gentle-sloping streams ($k_{sn} \sim 50$ m$^{0.9}$) the return time is close to 2 years, as proposed by *Wolman and Miller* [1960], in very steep streams ($k_{sn} \sim 400$ m$^{0.9}$) it can be as short as several days during both the high-flow regime during summer and the low-regime during winter. This short recurrence interval is due to two factors: first, in very steep channels the erosion threshold is small compared to typical bed shear stresses such that thresholds are almost unimportant [*DiBiase and Whipple*, 2011]. Second, the low discharge variability leads to a thin tail in the discharge distribution and although progressively larger floods are more erosive individually, they are so infrequent that the cumulative incision is less (Figure 12). What follows is that in some landscapes, like the Himalaya, where discharge variability is small, accounting for discharge variability [*Lague et al.*, 2005] is more important in gentle-sloping channels than in steep channels.

However, our assessment of the impact of incision thresholds and discharge variability hinges on the size of the threshold, which is not well defined. The notion that D_{50} or D_{84} is the controlling grain size for incipient motion of bed load has to our knowledge not been extended to very steep and rapidly eroding landscapes, in which several meter-sized boulders are frequently mantling river beds. Furthermore, because such material is more likely to be found in massive crystalline rocks, compared to thin-bedded sedimentary rocks, for example, there may be links to lithology and rock strength that go beyond the erodibility constant, k_e. In addition, while a threshold based on bed load sediment is meaningful, there may be other thresholds involved with plucking, for example. We see good reason that erosion thresholds vary with channel steepness or erosion rate, but quantifying such a relationship has only just begun [e.g., *Attal et al.*, 2015; *Sklar et al.*, 2016] and will be important for formulating more mechanistic rules for the threshold term. Further work is thus needed to quantify the dynamic range of channel geometry, flow resistance, and threshold magnitudes in natural channels.

7. Conclusions

We have shown that a stochastic-threshold stream power model is able to relate the first-order differences in erosional efficiency we observe between the Himalaya and Eastern Tibet to regional differences in discharge and channel widths. Although discharge variability during either the wet or dry monsoon

season is low and not particularly different between the two regions, large differences in mean discharge between the seasons allow for erosion thresholds to play a role. However, in our analysis incision thresholds are important only in low-relief (and thus low erosion rate) landscapes. By including spatially variable thresholds that depend on channel steepness, systematic mismatches between modeled and [10]Be-derived catchment average erosion rates at low channel steepness indices are reduced. In contrast, the mismatch persists for channels with high steepness indices. In steep channels, incision thresholds are easily exceeded by large boundary shear stresses, yet modeled erosion rates tend to be lower than those derived from [10]Be data. Potential reasons for this bias include infrequent large landslide events, unaccounted for differences in channel widths and rock strength, tools and cover effects of river sediment and complex dependencies of grain sizes on substrate and hillslope processes, and limited drainage connectivity due to past glaciations. At present, it is difficult to confidently say whether modeled erosion rates at high channel steepness values are truly too low, or whether [10]Be-derived erosion rates are actually too high; although there is some indication of [10]Be-derived erosion rates being too high due to effects of past glaciations. Our analysis of daily discharge records from a large number of gauging stations in monsoonal Asia yielded a robust parameterization of monsoonal discharge variability, which, in conjunction with the stochastic-threshold stream power model calibrated to the Himalaya suggests that temporal changes in discharge variability are unlikely to affect erosion rates much, whereas the seasonal duration and the total amount of summer monsoon discharge have the greatest effect on erosion rates. It should be noted, however, that poorly constrained parameters, such as the flow resistance coefficient, or unaccounted for variability in channel widths or rock strength, can have a similarly large impact on modeled erosion rates.

Our synthesis highlights the challenges in modeling erosion rates at regional scales with significant variations of climate, lithology and tectonics. Accounting for differences in precipitation and discharge using the stochastic-threshold approach is effective to first order and is probably the best possible approach based on current knowledge and widely available data. The next step is to better account for temporal changes in precipitation, i.e., moving beyond the historical discharge record, which requires quantitative estimates from both archives and models. Further progress also appears to require a more sophisticated account of the spatiotemporal variations of rock strength and sediment grain-size effects important for quantifying erosion thresholds and erodibility. Finally, our discussion has shown that there exist many methodological issues that complicate comparison of [10]Be-derived erosion rates with model results, specifically at high erosion rates. However, due to the limited opportunities of obtaining alternative indicators of landscape-scale erosion rates, and provided the growing number of erosion rates from cosmogenic nuclides, there is utility and promise in extracting further details about the linkages between threshold effects, climate variability, and river incision from such data sets. Although our modeling approach has limitations, it provides a tool to assess the impact of climate change on erosion of tectonically active mountain ranges.

References

Abrahami, R., P. van der Beek, P. Huyghe, E. Hardwick, and J. Carcaillet (2016), Decoupling of long-term exhumation and short-term erosion rates in the Sikkim Himalaya, *Earth Planet. Sci. Lett.*, *433*, 76–88, doi: 10.1016/j.epsl.2015.10.039.

Acosta, V.T., T. F. Schildgen, B. A. Clarke, D. Scherler, B. Bookhagen, H. Wittmann, F. von Blanckenburg, and M. R. Strecker (2015), The effect of vegetation cover on millennial-scale landscape denudation rates, *Lithosphere*, *7*, 408–420, doi:10.1130/L402.1.

Adams, B. A., K. X. Whipple, K. V. Hodges, and A. M. Heimsath (2016), In situ development of high-elevation, low-relief landscapes via duplex deformation in the eastern Himalayan hinterland, Bhutan, *J. Geophys. Res. Earth Surf.*, *121*, 294–319, doi:10.1002/2015JF003508.

Allen, G. H., J. B. Barnes, T. M. Pavelsky, and E. Kirby (2013), Lithologic and tectonic controls on bedrock channel form at the northwest Himalayan front, *J. Geophys. Res. Earth Surf.*, *118*, 1806–1825, doi:10.1002/jgrf.20113.

Andermann C., L. Longuervergne, S. Bonnet, A. Crave, P. Davy, and R. Gloaguen (2012), Impact of transient groundwater storage on the discharge of Himalayan rivers, *Nat. Geosci.*, *5*, 127–132, doi:10.1038/ngeo1356.

Ansberque, C., V. Godard, O. Bellier, J. De Sigoyer, J. Liu-Zeng, X. Xu, Z. Ren, Y. Li, and A. S. T. E. R. Team (2015), Denudation pattern across the Longriba fault system and implications for the geomorphological evolution of the eastern Tibetan margin, *Geomorphology*, *246*, 542–557, doi:10.1016/j.geomorph.2015.07.017.

Andersen, J. L., D. L. Egholm, M. F. Knudsen, J. D. Jansen, S. B. Nielsen (2015), The periglacial engine of mountain erosion—Part 1: Rates of frost cracking and frost creep, *Earth Surf. Dyn.*, *3*, 447–462, doi:10.5194/esurf-3-447-2015.

Attal, M., and L. Lavé (2006), Changes of bedload characteristics along the Marsyandi River (central Nepal): Implications for understanding hillslope sediment supply, sediment load evolution along fluvial networks, and denudation in active orogenic belts, in *Tectonics, Climate, and Landscape Evolution*, edited by S. D. Willett et al., *Geol. Soc. Am. Spec. Pap.*, *398*, 143–171, doi: 10.1130/2006.2398(09).

Attal, M., P. A. Cowie, A. C. Whittaker, D. E. J. Hobley, G. E. Tucker, and G. P. Roberts (2011), Testing fluvial erosion models using the transient response of bedrock rivers to tectonic forcing in the Apennines, Italy, *J. Geophys. Res.*, *116*, F02005, doi:10.1029/2010JF001875.

Attal, M., S. M. Mudd, M. D. Hurst, B. Weinman, K. Yoo, and M. Naylor (2015),Impact of change in erosion rate and landscape steepness on hillslope and fluvial sediments grain size in the Feather River basin (Sierra Nevada, California), *Earth Surf. Dyn.*, 3, 201–222, doi:10.5194/esurf-3-201-2015.

Avouac, J.-P. (2003), Mountain building, erosion, and the seismic cycle in the Nepal Himalaya, *Adv. Geophys.*, 46, 1–80, doi:10.1016/S0065-2687(03)46001-9.

Bagnold, R. A. (1977), Bed load transport by natural rivers, *Water Resour. Res.*, 13, 303–312, doi:10.1029/WR013i002p00303.

Balco, G., J. Stone, N. Lifton, and T. Dunai (2008), A complete and easily accessible means of calculating surface exposure ages or erosion rates from ^{10}Be and ^{26}Al measurements, *Quat. Geochronol.*, 3, 174–195, doi:10.1016/j.quageo.2007.12.001.

Ballantyne, C. K. (2002), Paraglacial geomorphology, *Quat. Sci. Rev.*, 21, 1935–2017.

Bookhagen, B., and D. W. Burbank (2006), Topography, relief, and TRMM-derived rainfall variations along the Himalaya, *Geophys. Res. Lett.*, 33, L08405, doi:10.1029/2006GL026037.

Bookhagen, B., and D. W. Burbank (2010), Toward a complete Himalayan hydrologic budget: Spatiotemporal distribution of snowmelt and rainfall and their impact on river discharge, *J. Geophys. Res.*, 115, F03019, doi:10.1029/2009JF001426.

Bookhagen, B., R. C. Thiede, and M. R. Strecker (2005), Late Quaternary intensified monsoon phases control landscape evolution in the northwest Himalaya, *Geology*, 33(2), 149–152, doi:10.1130/G20982.1.

Brocklehurst, S. H., and K. X. Whipple (2002), Glacial erosion and relief production in the Eastern Sierra Nevada, California, *Geomorphology*, 42, 1–24.

Buffington, J. M., and D. R. Montgomery (1997), A systematic analysis of eight decades of incipient motion studies, with special reference to gravel-bedded rivers, *Water Resour. Res.*, 33(8), 1993–2029.

Burbank, D.W., J. Leland, E. Fielding, R. S. Anderson, N. Brozovic, M. R. Reid, and C. Duncan (1996), Bedrock incision, rock uplift and threshold hillslopes in the northwestern Himalayas, *Nature*, 379, 505–510.

Burchfiel, B. C., Z. Chen, Y. Liu, and L. H. Royden (1995), Tectonics of the Longmen Shan and adjacent regoins, central China, *Int. Geol. Rev.*, 37, 661–735.

Carretier, S., V. Regard, R. Vassallo, G. Aguilar, J. Martinod, R. Riquelme, E. Pepin, R. Charrier, G. Hérail, M. Farías, J-L Guyot, G. Vargas and C. Lagane (2013), Slope and climate variability control of erosion in the Andes of central Chile, *Geology*, 41(2), 195–198, doi: 10.1130/G33735.1.

Church, M., and J. M. Ryder (1972), Paraglacial sedimentation: A consideration of fluvial processes conditioned by glaciation, *Geol. Soc. Am. Bull.*, 83, 3059–3072.

Church, M., and O. Slaymaker (1989), Disequilibrium of Holocene sediment yield in glaciated British Columbia, *Nature*, 337, 452–454.

Clarke, B. A., and D. W. Burbank (2010), Bedrock fracturing, threshold hillslopes, and limits to the magnitude of bedrock landslides, *Earth Planet. Sci. Lett.*, 297, 577–586, doi:10.1016/j.epsl.2010.07.011.

Clemens, S., W. Prell, D. Murray, G. Shimmield, and G. Weedon (1991), Forcing mechanisms of the Indian Ocean monsoon, *Nature*, 353, 720–725.

Clift, P. D., K. V. Hodges, D. Heslop, R. Hannigan, H. V. Long, and G. Calves (2008a), Correlation of Himalayan exhumation rates and Asian monsoon intensity, *Nat. Geosci.*, 1, 875–880, doi:10.1038/ngeo351.

Clift, P. D., L. Giosan, J. Blusztajn, I. H. Campbell, C. Allen, M. Pringle, A. R. Tabrez, M. Danish, M. M. Rabbani, A. Alizai, A. Carter, and A. Lückge (2008b), Holocene erosion of the Lesser Himalaya triggered by intensified summer monsoon, *Geology*, 36(1), 79–82, doi:10.1130/G24315A.1.

Craddock, W. H., D. W. Burbank, B. Bookhagen, and E. J. Gabet (2007), Bedrock channel geometry along an orographic rainfall gradient in the upper Marsyandi River valley in central Nepal, *J. Geophys. Res.*, 112, F03007, doi: 10.1029/2006JF000589.

Crave, A., and P. Davy (2001), A stochastic "precipiton" model for simulating erosion/sedimentation dynamics, *Comput. Geosci.*, 27, 815–827.

Cyr, A. J., D. E. Granger, V. Olivetti, and P. Molin (2010), Quantifying rock uplift rates using channel steepness and cosmogenic nuclide–determined erosion rates: Examples from northern and southern Italy, *Lithosphere*, 2(3), 188–198, doi:10.1130/L96.1.

D'Arcy, M., and A. C. Whittaker (2014), Geomorphic constraints on landscape sensitivity to climate in tectonically active areas, *Geomorphology*, 204, 366–381.

Dallmeyer, A., M. Claussen, Y. Wang, and U. Herzschuh (2013), Spatial variability of Holocene changes in the annual precipitation pattern: A model-data synthesis for the Asian monsoon region, *Clim. Dyn.*, 40, 2919–2936, doi:10.1007/s00382-012-1550-6.

de Ferranti, J. (2014), Digital elevation data. [Available at http://viewfinderpanoramas.org/dem3.html, accessed November 2012.]

DiBiase, R. A., and K. X. Whipple (2011), The influence of erosion thresholds and runoff variability on the relationships among topography, climate, and erosion rate, *J. Geophys. Res.*, 116, F04036, doi:10.1029/2011JF002095.

DiBiase, R. A., K. X. Whipple, A. M. Heimsath, and W. B. Ouimet (2010), Landscape form and millennial erosion rates in the san Gabriel Mountains, CA, *Earth Planet. Sci. Lett.*, 289(1–2), 134–144, doi:10.1016/j.epsl.2009.10.036.

DiBiase, R. A., A. M. Heimsath, and K. X. Whipple (2012), Hillslope response to tectonic forcing in threshold landscapes, *Earth Surf. Process. Landf.*, 37(8), 855–865, doi:10.1002/esp.3205.

Dietsch, C., J. M. Dortch, S. A. Reynhout, L. A. Owen, and M. W. Caffee (2015), Very slow erosion rates and landscape preservation across the southwestern slope of the Ladakh Range, India, *Earth Surf. Process. Landf.*, 40, 389–402, doi:10.1002/esp.3640.

Dortch, J. M., L. A. Owen, W. C. Haneberg, M. W. Caffee, C. Dietsch, and U. Kamp (2009), Nature and timing of large landslides in the Himalaya and Transhimalaya of northern India, *Quat. Sci. Rev.*, 28, 1037–1054, doi:10.1016/j.quascirev.2008.05.002.

Dühnforth, M., R. S. Anderson, D. Ward and G. M. Stock (2010), Bedrock fracture control of glacial erosion processes and rates, *Geology*, 38, 423–426, doi:10.1130/G30576.1.

Duvall, A., E. Kirby, and D. Burbank (2004), Tectonic and lithologic controls on bedrock channel profiles and processes in coastal California, *J. Geophys. Res.*, 109, F03002, doi:10.1029/2003JF000086.

Farr, T. G., P. A. Rosen, E. Caro, R. Crippen, R. Duren, S. Hensley, M. Kobrick, M. Paller, E. Rodriguez, L. Roth, D. Seal, S. Shaffer, J. Shimada, J. Umland, M. Werner, M. Oskin, D. Burbank, and D. Alsdorf (2007), The Shuttle Radar Topography Mission, *Rev. Geophys.*, 45, RG2004, doi:10.1029/2005RG000183.

Ferrier, K. L., K. L. Huppert, and J. T. Perron (2013), Climatic control of bedrock river incision, *Nature*, 496, 206–211, doi:10.1038/nature11982.

Ferguson, R. (2007), Flow resistance equations for gravel- and boulder-bed streams, *Water Resour. Res.*, 43, W05427, doi:10.1029/2006WR005422.

Finnegan, N. J., G. Roe, D. R. Montgomery, and B. Hallet (2005), Controls on the channel width of rivers: Implications for modeling fluvial incision of bedrock, *Geology*, 33(3), 229–232, doi:10.1130/G21171.1.

Finnegan, N. J., L. S. Sklar, and T. K. Fuller (2007), Interplay of sediment supply, river incision, and channel morphology revealed by the transient evolution of an experimental bedrock channel, *J. Geophys. Res.*, 112, F03S11, doi:10.1029/2006JF000569.

Finnegan, N. J., B. Hallet, D. R. Montgomery, P. K. Zeitler, J. O. Stone, A. M. Anders, and L. Yuping (2008), Coupling of rock uplift and river incision in the Namche Barwa-Gyala Peri massif, Tibet, *Geol. Soc. Am. Bull.*, *120*, 142–155.

Fisher, G. B., B. Bookhagen, and C. B. Amos (2013), Channel planform geometry and slopes from freely available high-spatial resolution imagery and DEM fusion: Implications for channel width scalings, erosion proxies, and fluvial signatures in tectonically active landscapes, *Geomorphology*, doi:10.1016/j.geomorph.2013.04.011.

Fisher, G. B., C. B. Amos, B. Bookhagen, D. W. Burbank, and V. Godard (2012), Channel widths, landslides, faults, and beyond: The new world order of high-spatial resolution Google Earth imagery in the study of Earth surface processes, in *Google Earth and Virtual Visualizations in Geoscience Education and Research*, edited by S. J. Whitmeyer et al., *Geol. Soc. Am. Spec. Pap., 492*, 1–22, doi:10.1130/2012.2492(01).

Flint, J. J. (1974), Stream gradient as a function of order, magnitude, and discharge, *Water Resour. Res.*, *10*, 969–973.

Gallen, S.F., M.K. Clark, and J.W. Godt (2015), Coseismic landslides reveal near-surface rock strength in a high-relief, tectonically active setting, *Geology*, *43*(1), 11–14, doi:10.1130/G36080.

Galy, A., and C. France-Lanord (2001), Higher erosion rates in the Himalaya: Geochemical constraints on riverine fluxes, *Geology*, *29*, 23–26.

Gansser, A. (1964), *Geology of the Himalayas*, 289 pp., Interscience, London.

Ganti, V., C. von Hagke, D. Scherler, M. P. Lamb, W. W. Fischer, J.-P. Avouac (2016), Time scale bias in erosion rates of glaciated landscapes, *Sci. Adv.*, *2*(10), e1600204, doi:10.1126/sciadv.1600204.

Gasse, F., M. Arnold, J. C. Fontes, M. Fort, E. Gibert, A. Huc, L. Bingyan, L. Yuanfang, L. Qing, F. Mélières, E. Van Campo, W. Fubao, and Z. Qingsong (1991), A 13,000-year climate record from western Tibet, *Nature*, *353*, 742–745.

Godard, V., D. L. Bourlès, F. Spinabella, D. W. Burbank, B. Bookhagen, G. B. Fisher, A. Moulin, and L. Léanni (2014), Dominance of tectonics over climate in Himalayan denudation, *Geology*, *42*(3), 243–246, doi: 10.1130/G35342.1.

Godard, V., D. W. Burbank, D. L. Bourlès, B. Bookhagen, R. Braucher, and G. B Fisher (2012), Impact of glacial erosion on [10]Be concentrations in fluvial sediments of the Marsyandi catchment, central Nepal, *J. Geophys. Res.*, *117*, F03013, doi:10.1029/2011JF002230.

Godard, V., J. Lavé, J. Carcaillet, R. Cattin, D. Bourlès, and J. Zhu (2010), Spatial distribution of denudation in Eastern Tibet and regressive erosion of plateau margins, *Tectonophysics*, *491*, 253–274.

Goodbred, S. L., Jr., and S. A. Kuehl (2000), Enormous Ganges-Brahmaputra sediment discharge during strengthened early Holocene monsoon, *Geology*, *28*(12), 1083–1086.

Hales, T. C., and J. J. Roering (2009), A frost "buzzsaw" mechanism for erosion of the eastern Southern Alps, New Zealand, *Geomorphology*, *107*, 241–253, doi:10.1016/j.geomorph.2008.12.012.

Harkins, N., E. Kirby, A. Heimsath, R. Robinson, and U. Reiser (2007), Transient fluvial incision in the headwaters of the Yellow River, northeastern Tibet, China, *J. Geophys. Res.*, *112*, F03S04, doi:10.1029/2006JF000570.

Henck, A. C., D. R. Montgomery, K. W. Huntington, and C. Liang (2010), Monsoon control of effective discharge, Yunnan and Tibet, *Geology*, *38*(11), 975–978, doi: 10.1130/G31444.1.

Herzschuh, U. (2006), Palaeo-moisture evolution in monsoonal Central Asia during the last 50,000 years, *Quat. Sci. Rev.*, *25*, 163–178, doi:10.1016/j.quascirev.2005.02.006.

Heyman, J. (2014), Paleoglaciation of the Tibetan Plateau and surrounding mountains based on exposure ages and ELA depression estimates, *Quat. Sci. Rev.*, *91*, 30–41, doi:10.1016/j.quascirev.2014.03.018.

Hobley, D. E. J., H. D. Sinclair, and S. M. Mudd (2012), Reconstruction of a major storm event from its geomorphic signature: The Ladakh floods, 6 August 2010, *Geology*, *40*, 483–486, doi: 10.1130/G32935.1.

Hodges, K. V. (2000), Tectonics of the Himalaya and southern Tibet from two perspectives, *Geol. Soc. Am. Bull.*, *112*(3), 324–350.

Howard, A. D. (1994), A detachment-limited model of drainage basin evolution, *Water Res. Research*, *30*(7), 2261–2285.

Howard, A. D., and G. Kerby (1983), Channel changes in badlands, *Geol. Soc. Am. Bull.*, *94*(6), 739–752, doi:10.1130/0016-7606(1983)94<739:CCIB>2.0.CO;2.

Howard, A. D., W. E. Dietrich, and M. A. Seidl (1994), Modeling fluvial erosion on regional to continental scales, *J. Geophys. Res.*, *99*(B7), 13,971–13,986.

Hurtrez, J.-E., F. Lucazeau, J. Lave, and J.-P. Avouac (1999), Investigation of the relationships between basin morphology, tectonic uplift, and denudation from the study of an active fold belt in the Siwalik Hills, central Nepal, *J. Geophys. Res.*, *104*, 12779–12796.

Immerzeel, W. W., L. P. H. van Beek, and M. F. P. Bierkens (2010), Climate change will affect the Asian water towers, *Science*, *328*, 1382–1385, doi: 10.1126/science.1183188.

Istanbulluoglu, E., and R. L. Bras (2005), Vegetation-modulated landscape evolution: Effects of vegetation on landscape processes, drainage density, and topography, *J. Geophys. Res.*, *110*, F02012, doi:10.1029/2004JF000249.

Kirby, E. and W. Ouimet (2011), Tectonic geomorphology along the eastern margin of Tibet: Insights into the pattern and processes of active deformation adjacent to the Sichuan Basin, in *Growth and Collapse of the Tibetan Plateau*, edited by R. Gloaguen and L. Ratschbacher, *Geol. Soc. London, Spec. Publ., 353*, 165–188.

Kirby, E., and K. Whipple (2001), Quantifying differential rock-uplift rates via stream profile analysis, *Geology*, *29*(5), 415–418.

Kirby, E., and K. X. Whipple (2012), Expression of active tectonics in erosional landscapes, *J. Struct. Geol.*, *44*, 54–75.

Kirby, E., K. X. Whipple, W. Tang, and Z. Chen (2003), Distribution of active rock uplift along the eastern margin of the Tibetan Plateau: Inferences from bedrock channel longitudinal profiles, *J. Geophys. Res.*, *108*(B4), 2217, doi: 10.1029/2001JB000861.

Kirby, E., P. W. Reiners, M. A. Krol, K. X. Whipple, K. V. Hodges, K. A. Farley, W. Tang, and Z. Chen (2002), Late Cenozoic evolution of the eastern margin of the Tibetan Plateau: Inferences from [40]Ar/[39]Ar and (U-Th)/he thermochronology, *Tectonics*, *21*(1), doi:10.1029/2000TC001246.

Kirchner, J. W., R. C. Finkel, C. S. Riebe, D. E. Granger, J. L. Clayton, J. G. King, and W. F. Megahan (2001), Mountain erosion over 10 yr, 10 k.y., and 10 m.y. Time scales, *Geology*, *29*(7), 591–594.

Korup, O. (2006), Rock-slope failure and the river long profile, *Geology*, *34*, 45–48, doi: 10.1130/G21959.1.

Kummerow, C., W. Barnes, T. Kozu, J. Shiue, and J. Simpson (1998), The Tropical Rainfall Measuring Mission (TRMM) sensor package, *J. Atmos. Ocean. Technol.*, *15*, 809–817.

Lague, D. (2010), Reduction of long-term bedrock incision efficiency by short-term alluvial cover intermittency, *J. Geophys. Res.*, *115*, F02011, doi:10.1029/2008JF001210.

Lague, D. (2014), The stream power river incision model: Evidence, theory and beyond, *Earth Surf. Process. Landf.*, *39*, 38–61, doi:10.1002/esp.3462.

Lague, D., and P. Davy (2003), Constraints on the long-term colluvial erosion law by analyzing slope-area relationships at various tectonic uplift rates in the Siwaliks Hills (Nepal), *J. Geophys. Res.*, *108*, 2129, doi:10.1029/2002JB001893.

Lague, D., N. Hovius, and P. Davy (2005), Discharge, discharge variability, and the bedrock channel profile, *J. Geophys. Res.*, *110*, F04006, doi:10.1029/2004JF000259.

Lamb, M., W. E. Dietrich, and J. G. Venditti (2008), Is the critical Shields stress for incipient motion dependent on channel-bed slope?, *J. Geophys. Res.*, *113*, F02008, doi:10.1029/2007JF000831.

Langbein, W. B. and S. A. Schumm (1958), Yield of sediment in relation to mean annual precipitation, *Eos Trans. AGU*, *39*, 1–9.

Lavé, J., and J.-P. Avouac (2001), Fluvial incision and tectonic uplift across the Himalayas of central Nepal, *J. Geophys. Res.*, *106*, 26561–26591.

Le Roux-Mallouf, R., V. Godard, R. Cattin, M. Ferry, J. Gyeltshen, J.-F. Ritz, D. Drupka, V. Guillou, M. Arnold, G. Aumaître, D. L. Bourlès, and K. Keddadouche (2015), Evidence for a wide and gently dipping main Himalayan thrust in western Bhutan, *Geophys. Res. Lett.*, *42*, 3257–3265, doi:10.1002/2015GL063767.

Li, G., A. J. West, A. L. Densmore, Z. Jin, R. N. Parker and R. G. Hilton (2014), Seismic mountain building: Landslides associated with the 2008 Wenchuan earthquake in the context of a generalized model for earthquake volume balance, *Geochem. Geophys. Geosyst.*, *15*, 833–844, doi:10.1002/2013GC005067.

Li, J., T. A. Ehlers, M. Werner, S. G. Mutz, C. Steger, and H. Paeth (2016), Late quaternary climate, precipitation δ^{18}O, and Indian monsoon variations over the Tibetan Plateau, *Earth Planet. Sci. Lett.*, doi:10.1016/j.epsl.2016.09.031

Lupker, M., P.-H. Blard, J. Lavé, C. France-Lanord, L. Leanni, N. Puchol, J. Charreau, and D. Bourlès (2012), ^{10}Be-derived Himalayan denudation rates and sediment budgets in the Ganga basin, *Earth Planet. Sci. Lett.*, *333-334*, 146–156, doi:10.1016/j.epsl.2012.04.020.

Mandal, S. K., M. Lupker, J.-P. Burg, P. G. Valla, N. Haghipour and M. Christl (2015), Spatial variability of ^{10}Be-derived erosion rates across the southern Peninsular Indian escarpment: A key to landscape evolution across passive margins, *Earth Planet. Sci. Lett.*, *425*, 154–167, doi:10.1016/j.epsl.2015.05.050.

Meyer-Christoffer, A., A. Becker, P. Finger, B. Rudolf, U. Schneider, and M. Ziese (2011), GPCC climatology version 2011 at 0.25: Monthly land-surface precipitation climatology for every month and the total year from rain-gauges built on GTS-based and historic data, doi:10.5676/DWD_GPCC/CLIM_M_V2011_025.

Mezaki, S., and M. Yabiku (1984), Channel morphology of the Kali Gandaki and the Narayani rivers in central Nepal, *J. Nepal Geol. Soc.*, *4*, 161–176.

Miehe, G., M. Winiger, J. Böhner, and Z. Yili (2001), The climatic diagram map of High Asia, *Erdkunde*, *55*, 94–97.

Miller, M. C., I. N. McCave, and P. D. Komar (1977), Threshold of sediment motion under unindirectional currents, *Sedimentology*, *24*, 507–527.

Morrell, K. D., M. Sandiford, C. P. Rajendran, K. Rajendran, A. Alimanovic, D. Fink, and J. Sanwal (2015), Geomorphology reveals active décollement geometry in the central Himalayan seismic gap, *Lithosphere*, *7*(3), 247–256.

Molnar, P., and P. Tapponnier (1975), Cenozoic tectonics of Asia: Effects of a continental collision, *Science*, *189*, 419–426.

Molnar, P., R. S. Anderson, G. Kier, and J. Rose (2006), Relationships among probability distributions of stream discharges in floods, climate, bed load transport, and river incision, *J. Geophys. Res.*, *111*, F02001, doi:10.1029/2005JF000310.

Molnar, P., R. S. Anderson, and S. P. Anderson (2007), Tectonics, fracturing of rock, and erosion, *J. Geophys. Res.*, *112*, F03014, doi:10.1029/2005JF000433.

Montgomery, D. R., and K. B. Gran (2001), Downstream variations in the width of bedrock channels, *Water Resour. Res.*, *37*(6), 1841–1846, doi:10.1029/2000WR900393.

Montgomery, D. R., B. Hallet, L. Yuping, N. Finnegan, A. Anders, A. Gillespie, and H. M. Greenberg (2004), Evidence for Holocene megafloods down the Tsangpo River gorge, southeastern Tibet, *Quat. Res.*, *62*, 201–207.

Moon, S., C. P. Chamberlain, K. Blisniuk, N. Levine, D. H. Rood, and G. E. Hilley (2011), Climatic control of denudation in the deglaciated landscape of the Washington cascades, *Nat. Geosci.*, *4*, 469–473, doi:10.1038/NGEO1159.

Munack, H., O. Korup, A. Resentini, M. Limonta, E. Garzanti, J. H. Blöthe, D. Scherler, H. Wittmann, and P. W. Kubik (2014), Postglacial denudation of western Tibetan Plateau margin outpaced by long-term exhumation, *Geol. Soc. Am. Bull.*, *126*(11/12), 1580–1594, doi:10.1130/B30979.

Niemi, N., M. Oskin, D. Burbank, A. Heimsath, and E. Gabet (2005), Effects of bedrock landslides on cosmogenically determined erosion rates, *Earth Planet. Sci. Lett.*, *237*, 480–498, doi:10.1016/j.epsl.2005.07.009.

Norton, K. P., L. M. Abbühl, and F. Schlunegger (2010), Glacial conditioning as an erosional driving force in the central Alps, *Geology*, *38*, 655–658, doi:10.1130/G31102.1.

Olen, S. M., B. Bookhagen, B. Hoffmann, D. Sachse, D. P. Adhikari, and M. R. Strecker (2015), Understanding erosion rates in the Himalayan orogen: A case study from the Arun Valley, *J. Geophys. Res. Earth Surf.*, *120*, 2080–2102, doi:10.1002/2014JF003410.

Olen, S., B. Bookhagen, and M. R. Strecker (2016), Role of climate and vegetation density in modulating denudation rates in the Himalaya, *Earth Planet. Sci. Lett.*, *445*, 57–67, doi:10.1016/j.epsl.2016.03.047.

Orem, C. A., and J. D. Pelletier (2016), The predominance of post-wildfire erosion in the long-term denudation of the Valles caldera, New Mexico, *J. Geophys. Res. Earth Surf.*, *121*, 843–864, doi:10.1002/2015JF003663.

Ouimet, W. B. (2010), Landslides associated with the May 12, 2008 Wenchuan earthquake: Implications for the erosion and tectonic evolution of the Longmen Shan, *Tectonophysics*, *491*, 244–252, doi:10.1016/j.tecto.2009.09.012.

Ouimet, W. B., K. X. Whipple, and D. E. Granger (2009), Beyond threshold hillslopes: Channel adjustment to base-level fall in tectonically active mountain ranges, *Geology*, *37*(7), 579–582, doi:10.1130/G30013A.1.

Ouimet, W. B., K. X. Whipple, B. T. Crosby, J. P. Johnson, and T. F. Schildgen (2008), Epigenetic gorges in fluvial landscapes, *Earth Surf. Process. Landf.*, *33*, 1993–2009, doi:10.1002/esp.1650.

Pan, G., J. Ding, D. Yao, and L. Wang (2004), *Geological Map of Qinghai-Xizang (Tibet) Plateau and Adjacent Areas (1:1,500,000), Chengdu Institute of Geology and Mineral Resources, China Geological Survey*, Chengdu Cartographic House, Chengdu.

Pitlick, J. (1994), Relation between peak flows, precipitation, and physiography for five mountainous regions in the western USA, *J. Hydrol.*, *158*, 219–240.

Portenga, E. W., P. R. Bierman, C. Duncan, L. B. Corbett, N. M. Kehrwald, and D. H. Rood (2015), Erosion rates of the Bhutanese Himalaya determined using *in situ*-produced ^{10}Be, *Geomorphology*, *233*, 112–126, doi: 10.1016/j.geomorph.2014.09.027.

Prancevic, J. P., and M. P. Lamb (2015), Unraveling bed slope from relative roughness in initial sediment motion, *J. Geophys. Res. Earth Surf.*, *120*, doi:10.1002/2014JF003323.

Rice, S. P., M. T. Greenwood, and C. B. Joyce (2001), Tributaries, sediment sources and the organization of macroinvertebrate fauna in river systems, *Can. J. Fish. Aquat. Sci.*, *58*, 824–840.

Riebe, C. S., L. S. Sklar, C. E. Lukens, and D. L. Shuster (2015), Climate and topography control the size and flux of sediment produced on steep mountain slopes, *Proc. Natl. Acad. Sci. U.S.A*, *112*(51), 15,574–15,579, doi:10.1073/pnas.1503567112.

Rossi, M., K. X. Whipple, and E. R. Vivoni (2015), Precipitation and evapotranspiration controls on daily runoff variability in the contiguous United States and Puerto Rico, *J. Geophys. Res. Earth Surf.*, *121*, 128–145, doi:10.1002/2015JF003446.

Royden, L. H., B. C. Burchfiel, R. W. King, Z. Chen, F. Shen and Y. Liu (1997), Surface deformation and lower crustal flow in Eastern Tibet, *Science*, *276*, 788–790.

Safran, E. B., P. R. Bierman, R. Aalto, T. Dunne, K. X. Whipple, and M. Caffe (2005), Erosion rates driven by channel network incision in the Bolivian Andes, *Earth Surf. Process. Landf.*, *30*, 1007–1024, doi: 10.1002/esp.1259.

Schaller, M., and T. Ehlers (2006), Limits to quantifying climate driven changes in denudation rates with cosmogenic nuclides, *Earth Planet. Sci. Lett.*, *248*, 153–167.

Scherler, D. (2014), Climatic limits to headwall retreat in the Khumbu Himalaya, eastern Nepal, *Geology*, *42*(11), 1019–1022, doi:10.1130/G35975.1.

Scherler, D., B. Bookhagen, M. R. Strecker, F. von Blanckenburg, and D. Rood (2010), Timing and extent of late Quaternary glaciation in the western Himalaya constrained by ^{10}Be moraine dating in Garhwal, India, *Quat. Sci. Rev.*, *29*, 815–831.

Scherler, D., B. Bookhagen, and M. R. Strecker (2014a), Tectonic control on 10Be-derived erosion rates in the Garhwal Himalaya, India, *J. Geophys. Res. Earth Surf.*, *118*, 1–24, doi:10.1002/2013JF002955.

Scherler, D., B. Bookhagen, H. Wulf, F. Preusser, and M. R. Strecker (2015), Increased late Pleistocene erosion rates during fluvial aggradation in the Garhwal Himalaya, northern India, *Earth Planet. Sci. Lett.*, *428*, 255–266, doi: 10.1016/j.epsl.2015.06.034.

Scherler, D., H. Munack, J. Mey, P. Eugster, H. Wittmann, A. T. Codilean, P. Kubik, and M. R. Strecker (2014b), Ice dams, outburst floods, and glacial incision at the western margin of the Tibetan Plateau: A >100 k.y. chronology from the Shyok Valley, Karakoram, *Geol. Soc. Am. Bull.*, *126*, 738–758, doi:10.1130/B30942.1.

Schildgen, T. F., D. Cosentino, B. Bookhagen, S. Niedermann, C. Yildirim, H. P. Echtler, H. Wittmann, and M. R. Strecker (2012), Multi-phased uplift of the southern margin of the Central Anatolian plateau, Turkey: A record of tectonic and upper mantle processes, *Earth Planet. Sci. Lett.*, *317-318*, 85–95, doi:10.1016/j.epsl.2011.12.003.

Schwanghart, W., and D. Scherler (2014), Short communication: TopoToolbox 2 – MATLAB-based software for topographic analysis and modeling in Earth surface sciences. *Earth Surf. Dyn.*, *2*, 1–7, doi:10.5194/esurf-2-1-2014.

Shen, Z.-K., J. Sun, P. Zhang, Y. Wan, M. Wang, R. Bürgmann, Y. Zeng, W. Gan, H. Liao, and Q. Wang (2009), Slip maxima at fault junctions and rupturing of barriers during the 2008 Wenchuan earthquake, *Nat. Geosci.*, *2*, 718–724, doi:10.1038/ngeo636.

Shields, A. (1936), Awendung der Ähnlichkeitsmechanik und der Turbulenzforschung auf die Geschiebebewegung, *Mitt. Preuss. Versuchsanst. Wasserbau Schiffbau*, *26*, 26.

Sklar, L., and W. E. Dietrich (1998), River longitudinal profiles and bedrock incision models: Stream power and the influence of sediment supply, in *Rivers Over Rock: Fluvial Processes in Bedrock Channels*, edited by K. J. Tinkler and E. E. Wohl, pp. 237–260, AGU, Washington, D. C., doi:10.1029/GM107p0237.

Sklar, L., and W. E. Dietrich (2001), Sediment and rock strength controls on river incision into bedrock, *Geology*, *29*(12), 1087–1090, doi:10.1130/0091-7613(2001)029<1087:SARSCO>2.0.CO;2.

Sklar, L. S., and W. E. Dietrich (2004), A mechanistic model for river incision into bedrock by saltating bed load, *Water Resour. Res.*, *40*, W06301, doi:10.1029/2003WR002496.

Sklar, L. S., and W. E. Dietrich (2006), The role of sediment in controlling steady-state bedrock channel slope: Implications of the saltation–abrasion incision model, *Geomorphology*, *82*, 58–83.

Sklar, L. S., C. S. Riebe, J. A. Marshall, J. Genetti, S. Leclere, C. L. Lukens, and V. Merces (2016), The problem of predicting the size distribution of sediment supplied by hillslopes to rivers, *Geomorphology*, *277*, 31–49, doi: 10.1016/j.geomorph.2016.05.005.

Snyder, N. P., K. X. Whipple, G. E. Tucker, and D. J. Merritts (2003), Importance of a stochastic distribution of floods and erosion thresholds in the bedrock river incision problem, *J. Geophys. Res.*, *108*(B2), 2117, doi:10.1029/2001JB001655.

St. Clair, J., S. Moon, W. S. Holbrook, J. T. Perron, C. S. Riebe, S. J. Martel, B. Carr, C. Harman, K. Singha, and D. deB. Richter (2015), Geophysical imaging reveals topographic stress control of bedrock weathering, *Science*, *350*, 534–538, doi:10.1126/science.aab2210.

Stevens, V. L., and J.-P. Avouac (2016), Millenary M_w > 9.0 earthquakes required by geodetic strain in the Himalaya, *Geophys. Res. Lett.*, *43*, 1118–1123, doi:10.1002/2015GL067336.

Thiede, R., and T. A. Ehlers (2013), Large spatial and temporal variations in Himalayan denudation, *Earth Planet. Sci. Lett.*, *371-372*, 278–293.

Tinkler, K. J., and E. E. Wohl (1998), A primer on bedrock channels, in *Rivers Over Rock: Fluvial Processes in Bedrock Channels*, *Geophys. Monogr. Ser.*, vol. 107, edited by K. J. Tinkler and E. E. Wohl, pp. 1–18, AGU, Washington, D. C.

Tucker, G. E. (2004), Drainage basin sensitivity to tectonic and climatic forcing: Implications of a stochastic model for the role of entrainment and erosion thresholds, *Earth Surf. Process. Landf.*, *29*, 185–205, doi:10.1002/esp.1020.

Tucker, G. E., and R. L. Bras (2000), A stochastic approach to modeling the role of rainfall variability in drainage basin evolution, *Water Resour. Res.*, *36*(7), 1953–1964, doi:10.1029/2000WR900065.

Turcotte, D. L., and L. Greene (1993), A scale-invariant approach to flood-frequency analysis, *Stoch. Hydrol. Hydraul.*, *7*, 33–40.

Turowski, J. M., N. Hovius, A. Wilson, and M.-J. Hong (2008), Hydraulic geometry, river sediment and the definition of bedrock channels, *Geomorphology*, *99*, 26–38.

von Blanckenburg, F. (2005), The control mechanisms of erosion and weathering at basin scale from cosmogenic nuclides in river sediment, *Earth Planet. Sci. Lett.*, *237*, 462–479.

Wang, Y., H. Cheng, R. L. Edwards, X. Kong, X. Shao, S. Chen, J. Wu, X. Jiang, X. Wang, and Z. An (2008), Millennial- or orbital-scale changes in the East Asian monsoon over the past 224,000 years, *Nature*, *451*, 1090–1093, doi:10.1038/nature06692.

West, A. J., R. Hetzel, G. Li, Z. Jin, F. Zhang, R. G. Hilton, and A. L. Densmore (2014), Dilution of ^{10}Be in detrital quartz by earthquake-induced landslides: Implications for determining denudation rates and potential to provide insights into landslide sediment dynamics, *Earth Planet. Sci. Lett.*, *396*, 143–153, doi:10.1016/j.epsl.2014.03.058.

Whipple, K. X., R. A. DiBiase, and B. T. Crosby (2013), Bedrock rivers, in *Treatise on Geomorphology*, vol. 9, edited by J. Shroder (Editor in Chief) and E. Wohl (Ed.), pp. 550–573, Academic Press, San Diego, Calif.

Whipple, K. X. (2004), Bedrock rivers and the geomorphology of active orogens, *Annu. Rev. Earth Planet. Sci.*, *32*, 151–85, doi: 10.1146/annurev.earth.32.101802.120356.

Whipple, K. X., and G. E. Tucker (1999), Dynamics of the stream-power river incision model: Implications for height limits of mountain ranges, landscape response timescales, and research needs, *J. Geophys. Res.*, *104*(B8), 17,661–17,674, doi:10.1029/1999JB900120.

Whipple, K. X., G. S. Hancock, and R. S. Anderson (2000a), River incision into bedrock: Mechanics and relative efficacy of plucking, abrasion, and cavitation, *Geol. Soc. Am. Bull.*, *112*(3), 490–503, doi:10.1130/0016-7606(2000)112<490:RIIBMA>2.0.CO;2.

Whipple, K. X., N. P. Snyder, and K. Dollenmayer (2000b), Rates and processes of bedrock incision by the Upper Ukak River since the 1912 Novarupta ash flow in the valley of Ten Thousand Smokes, Alaska, *Geology*, *28*(9), 835–838.

Whipple, K. X., and G. E. Tucker (2002), Implications of sediment-flux dependent river incision models for landscape evolution, *J. Geophys. Res.*, *107*(B2), 2093, doi:10.1029/2000JB000044.

Winiger, M., M. Gumpert, H. Yamout (2005), Karakorum–Hindukush–western Himalaya: Assessing high-altitude water resources, *Hydrol. Process.*, *19*, 2329–2338.

Wobus, C., A. M. Heimsath, K. X. Whipple, and K. V. Hodges (2005), Active out-of-sequence thrust faulting in the central Nepalese Himalaya, *Nature*, *434*, 1008–1011, doi:10.1038/nature03499.

Wobus, C., K. X. Whipple, E. Kirby, N. Snyder, J. Johnson, K. Spyropolou, B. Crosby, and D. Sheehan (2006), Tectonics from topography: Procedures, promise, and pitfalls, *Geol. Soc. Am. Spec. Pap.*, *398*, 55–74, doi:10.1130/2006.2398(04).

Wohl, E., and G. C. L. David (2008), Consistency of scaling relations among bedrock and alluvial channels, *J. Geophys. Res.*, *113*, F04013, doi:10.1029/2008JF000989.

Wolman, M. G., and J. P. Miller (1960), Magnitude and frequency of forces in geomorphic processes, *J. Geol.*, *68*(1), 54–74.

Wulf, H., B. Bookhagen, and D. Scherler (2010), Seasonal precipitation gradients and their impact on fluvial sediment flux in the northwest Himalaya, *Geomorphology*, *118*(1–2), 13–21, doi:10.1016/j.geomorph.2009.12.003.

Wulf, H., B. Bookhagen, and D. Scherler (2012), Climatic and geologic controls on suspended sediment flux in the Sutlej River Valley, western Himalaya, *Hydrol. Earth Syst. Sci.*, *16*, 2193–2217, doi:10.5194/hess-16-2193-2012.

Wulf, H., B. Bookhagen, and D. Scherler (2015), Differentiating between rain, snow, and glacier contributions to river discharge in the western Himalaya using remote-sensing data and distributed hydrological modelling, *Adv. Water Resour.*, doi:10.1016/j.advwatres.2015.12.004.

Yalin, M. S., and E. Karahan (1979), Inception of sediment transport, *J. Hydraul. Div. ASCE*, *105*(11), 1433–1443.

Yanites, B. J., G. E. Tucker, K. J. Mueller, Y.-G. Chen, T. Wilcox, S.-Y. Huang, and K.-W. Shi (2010), Incision and channel morphology across active structures along the Peikang River, central Taiwan: Implications for the importance of channel width, *Geol. Soc. Am. Bull.*, *122*(7/8), 1192–1208, doi: 10.1130/B30035.1.

Yanites, B. J., G. E. Tucker, and R. S. Anderson (2009), Numerical and analytical models of cosmogenic radionuclide dynamics in landslide-dominated drainage basins, *J. Geophys. Res.*, *114*, F01007, doi:10.1029/2008JF001088.

Yin, A. (2006), Cenozoic tectonic evolution of the Himalayan orogen as constrained by along-strike variation of structural geometry, exhumation history, and foreland sedimentation, *Earth Sci. Rev.*, *76*, 1–131.

Zhang, P.-Z., X.-Z. Wen, Z.-K. Shen, and J.-H. Chen (2010), Oblique, high-angle, listric-reverse faulting and associated development of strain: The Wenshuan earthquake of May 12, 2008, Sichuan, China, *Annu. Rev. Earth Planet. Sci.*, *38*, 353–382, doi: 10.1146/annurev-earth-040809-152602.